REPORT DOCUMENTATION PAGE

Form Approved
OMB No. 0704-0188

Public reporting burden for this collection of information is astimated to average 1 hour per responsa, including tha tima for reviewing instructions, searching existing data sources, gathering and maintaining the data needed, and complating and reviewing this collection of information. Send comments regarding this burden estimete or eny other espect of this collection of information, including suggestions for reducing this burden to Department of Defanse, Washington Headquarters Sarvices, Directorete for Informetion Operations and Raports (0704-0188), 1215 Jefferson Davis Highwey, Suita 1204, Arlington, VA 22202-4302. Raspondents should be aware that notwithstanding any other provision of law, no person shall be subject to any penalty for failing to comply with a collection of information if it does not displey e currently valid OMB control number. **PLEASE DO NOT RETURN YOUR FORM TO THE ABOVE ADDRESS.**

1. REPORT DATE *(DD-MM-YYYY)*	2. REPORT TYPE	3. DATES COVERED *(From - To)*
05-13-2011	Final	30 Mar 07 - 30 Apr 11

4. TITLE AND SUBTITLE

An Experimental Investigation of the Acoustic and Fluid Dynamic Characteristics of a Circulation-Controlled Airfoil

5a. CONTRACT NUMBER
N00014-07-1-0824 & N00014-10-1-0679

5b. GRANT NUMBER

5c. PROGRAM ELEMENT NUMBER

6. AUTHOR(S)
L Cattafesta, D Wetzel

5d. PROJECT NUMBER

5e. TASK NUMBER

5f. WORK UNIT NUMBER

7. PERFORMING ORGANIZATION NAME(S) AND ADDRESS(ES)

University of Florida
Mechanical and Aerospace
Engineering
231 Aerospace Building
Gainesville FL 32611-6250

8. PERFORMING ORGANIZATION REPORT NUMBER

9. SPONSORING / MONITORING AGENCY NAME(S) AND ADDRESS(ES)
ONR
875 N Randolph St
Arlington VA 22203-1995

10. SPONSOR/MONITOR'S ACRONYM(S)

11. SPONSOR/MONITOR'S REPORT NUMBER(S)

12. DISTRIBUTION / AVAILABILITY STATEMENT

Approved for Public Release; distribution is unlimited

13. SUPPLEMENTARY NOTES
This contract was awarded under N00014-07-1-0824 and continued under N00014-10-1-0679.

14. ABSTRACT

The purpose of this investigation is to experimentally identify and characterize the flow field and corresponding noise sources of a circulation control airfoil. Flow and acoustic data are obtained for a dual-slotted, elliptic circulation control airfoil in an anechoic wind tunnel. The effect of single-slot blowing on the aerodynamic characteristics of the airfoil and the flow field is evaluated. Noise sources are identified for a variety of test conditions, and the acoustic data are compared with an existing analytical model of circulation control acoustics. An accurate acoustic model combined with specific information about each noise source mechanism will provide future researchers with the tools necessary to intuitively design and test quiet circulation control appendages for use on underwater vehicles.

15. SUBJECT TERMS
Circulation Control

16. SECURITY CLASSIFICATION OF:			17. LIMITATION OF ABSTRACT	18. NUMBER OF PAGES	19a. NAME OF RESPONSIBLE PERSON
a. REPORT	**b. ABSTRACT**	**c. THIS PAGE**			L Cattafesta
Unclassified	Unclassified	Unclassified	UL	96	**19b. TELEPHONE NUMBER** *(include area code)* (352) 846-3017

Standard Form 298 (Rev. 8-98)
Prescribed by ANSI Std. Z39.18

An Experimental Investigation of the Acoustic and Fluid Dynamic Characteristics of a Circulation-Controlled Airfoil

Drew Wetzel[+], and Louis Cattafesta[*]

University of Florida

[+] *Graduate Research Assistant, Mechanical and Aerospace Engineering Department*
[*] *Professor, Mechanical and Aerospace Engineering Department*

1   Technical Objectives

Coanda-effect circulation control (CC) has shown tremendous promise for high-lift control surfaces in underwater naval vehicles (Rogers & Donnelly 2004). CC increases lift generation at low mean flow speeds without deploying mechanical devices. However, additional self-noise is produced over and above trailing edge noise. Unfortunately, our understanding of CC acoustics is limited. Salikuddin *et al.* (1987) and, more recently, Munro *et al.* (2001) have experimentally studied the noise due to conventional upper surface blowing on an airfoil with a mechanical flap appendage, which is most suitable for aircraft configurations. On the other hand, Howe (2002) has analyzed sound production from a hydrofoil and identified three mechanisms: (1) low frequency curvature noise associated with interaction of a turbulent boundary layer with the rounded trailing edge, (2) high frequency jet-slot noise, and (3) passive slot noise caused by diffraction of nearfield pressure fluctuations in the turbulent boundary layer by the slot lip. This theory has not been experimentally confirmed. To complicate matters further, recent work by Rogers & Donnelly (2004) has demonstrated the potential of dual-slotted (i.e., upper and lower surface) blowing configurations. The noise associated with this configuration has not yet been systematically studied.

The objectives of this study are to experimentally characterize the acoustics and fluid dynamics of an elliptic circulation control airfoil. Particle image velocimetry measurements provide insight into the flow physics related to the noise generation mechanisms. A variety of acoustic measurement techniques are compared to determine what methods may be suitable for measuring circulation control noise. Noise sources are identified, and their far-field acoustic levels are compared to determine the primary sources over different frequency ranges. Finally, Howe's theoretical model of circulation control noise is evaluated and compared with measurements (Howe 2002).

2   Technical Approach

A two-dimensional, dual-slotted, elliptic circulation control airfoil based on the hydrofoil studied by Rogers & Donnelly (2004) is designed and fabricated. Tests are conducted in the University of Florida Aeroacoustic Flow Facility (UFAFF) at low and moderate chord Reynolds numbers ($Re_c = 6.5 \times 10^5$ to 1.3×10^6) and zero angle of attack. Focus is placed on low blowing, moderate lift performance typical of an underwater vehicle control surface. Higher lift cases appropriate for application to STOL aircraft are also studied. Steady surface pressure measurements are used to characterize the freestream flow and determine lift as a function of momentum coefficient. The freestream and curved wall jet flows are measured and analyzed using PIV. Multiple far-field

microphones and a nested phased microphone array are used for determining source levels and identifying noise sources. Using data from the PIV study, Howe's model of circulation control acoustics is evaluated and compared with measurements (Howe 2002).

3 Experimental Setup

For a complete description of the experimental setup, please refer to Wetzel (2011). For convenience, a brief summary of the experimental setup is included in this report.

3.1 Circulation Control Airfoil

A dual-slotted, two-dimensional circulation control airfoil, shown in Figure 1A, is designed based on the geometry of the hydrofoil previously studied by Rogers & Donnelly (2004). The airfoil's profile is a 20% thickness-to-chord ratio ellipse with a cylindrical trailing edge and no camber. Details regarding the trailing edge geometry are provided in Figure 1B. The airfoil has a 0.5207 m chord and 1.12 m span. Although the frontal area ratio between the model and tunnel inlet cross-sections is somewhat high (14%), the large airfoil size is chosen for a number of reasons, including: to suit anticipated full-scale application chord Reynolds numbers and momentum coefficients, for improved spatial resolution in measurements, for reduced compressibility effects in the slot jet, and for lower acoustic frequencies. The height of each blowing slot is adjustable using eight sets of push-pull screws equally spaced across the span. Each blowing slot is supplied pressurized air from two constant area air feeds, one on each side of each plenum. The model is primarily machined from cast aluminum tool plate.

During the investigation, only a single blowing slot is used at any given time. The other, unused blowing slot is set to the nominal slot height of 1.0 mm and sealed with tape. Spanwise strips of 12 mm wide, 0.4 mm thick, Glasfaser Flugzeug-Service zig-zag turbulator tape are placed on the airfoil at 18% chord to trip the upper and lower surface boundary layers. ghboring labs for model leak tests and slot flow uniformity studies between tunnel entries.

3.2 University of Florida Aeroacoustic Flow Facility

The UFAFF is an open-return wind tunnel with an open-jet test section installed in an ISO 3745-certified 100 Hz anechoic chamber, which is used to simulate a free field, or reflection-free acoustic environment. The test section measures 0.74 m tall by 1.12 m wide and extends 1.83 m in the flow direction. Test section speeds between 18 and 75 m/s can be reached with turbulent intensity levels below 0.1% at frequencies above 10 Hz (Mathew *et al.* 2005). In 2010, a flow silencer was added upstream of the inlet, and over one meter of the diffuser was removed. Figure 2 provides schematics of the circulation control airfoil installed in the pre- and post-modification tunnel configurations. For illustration purposes, some ceiling wedges are removed in the renderings to reveal the chamber interior and test section. The airfoil is installed 13 cm downstream of the inlet exit plane at zero degrees geometric angle of attack. The model is always bounded by sidewalls for two dimensional flow. For more information regarding the UFAFF, please refer to Mathew *et al.* (2005).

3.3 Flow Measurements

3.3.1 Steady Pressure and Lift

Steady surface pressure, p_s, is measured using 47 0.711 mm inner diameter midspan static pressure ports, including nine located on the midspan trailing edge instrument ring. The taps are symmetrically distributed on the upper and lower surfaces of the airfoil. Two taps placed at the leading edge of the airfoil are slightly offset from midspan due to installation constraints. Three 16-channel Esterline Pressure Systems (PSI) pressure scanners (ranges 5 psi, 1 psi, and 10 inH$_2$O) measure 39 static surface pressures, four Venturi meter pressures, and the blowing slot plenum pressure. Data are acquired at two samples per second for 30 seconds. The pressure scanners' reference pressure ports are connected to the tunnel pitot-static pressure port. The pitot-static and pitot-dynamic pressures are measured using Mensor 6115 digital pressure transducers with ranges of 16 psia and 0.58 psig, respectively. Surface pressure coefficients are computed by dividing the pressure scanner output, $p_s - p_\infty$, by the pitot-dynamic pressure, q_∞.

$$C_p = \frac{p_s - p_\infty}{q_\infty} \tag{1}$$

Because of the coarse resolution of pressure taps, the C_p data, plotted versus normalized chordwise position, are fit with a cubic spline curve that is integrated to determine the lift coefficient per unit span.

$$c_l = \int_0^1 \Delta C_p \, d(x/c) = \int_0^1 \left(C_{p,lower} - C_{p,upper} \right) d(x/c) \tag{2}$$

3.3.2 Slot Jet Velocity and Momentum Coefficient

The mean slot jet velocity is computed assuming an isentropic expansion from the plenum to the freestream,

$$U_{jet} = \sqrt{2RT_0 \left(\frac{\gamma}{\gamma - 1} \right) \left[1 - \left(\frac{p_\infty}{p_0} \right)^{(\gamma-1)/\gamma} \right]}, \tag{3}$$

where γ is the ratio of specific heats, and R is the ideal gas constant. The measured freestream pitot-static pressure, p_∞, is added to the measured relative plenum pressure to determine the absolute plenum pressure, p_0. The air line stagnation temperature, T_0, is recorded using a resistance temperature detector (RTD). For the complete derivation of Equation 3 and the influence of a nonzero plenum velocity on the jet velocity estimate, see Wetzel (2011).

The momentum coefficient is calculated using the combined mass flow rates of the two Venturi meters, the jet velocity computed from Equation 3, the measured freestream dynamic pressure, and the circulation control model planform area, S,

$$C_\mu = \frac{\dot{m} U_{jet}}{q_\infty S}. \tag{4}$$

3.3.3 Particle Image Velocimetry

Particle image velocimetry provides a non-intrusive means of measuring the velocity and related properties of a flow field (Raffel *et al.* 2007). The local displacement of tiny particles seeded

within a flow are detected by imaging two snapshots of the flow illuminated by a "instantaneous" light source. The light source, which is a laser beam that passes through a series of lenses to form a thin laser sheet, illuminates a planar region of interest in the flow field. The two spatially coincident lasers are pulsed at a known rate but separated by a specified amount of time, typically on the order of microseconds. For two-dimensional PIV, a camera positioned outside the flow field and aligned normal to the laser sheet captures a pair of images for each pair of laser pulses. The image pair is discretized into smaller regions called interrogation windows, where each interrogation window is designed to contain several common illuminated particles for each frame of the image pair. The spatial cross-correlation of each corresponding pair of windows is then computed using Fast Fourier Transforms (FFTs). The average x- and y-displacements of the group of particles within each window pair are determined from the location of the highest correlation peak. The in-plane velocity components are calculated from these displacements and the known time between laser pulses. Altogether, the discretized velocity measurements obtained from an image pair provide a snapshot of the velocity flow field. With a large enough set of measured vector fields such that statistical convergence is achieved, turbulent flow quantities can also be estimated.

Five different PIV experiments are performed to capture different flow phenomenon. The flow is measured in regions around the leading edge, behind the trailing edge, above the slot lip, and along the curved trailing edge in the chordwise plane, as shown in Figure 3. The trailing edge flow is also measured once in the spanwise plane. For more information on the PIV experimental setup, please see Wetzel (2011).

3.4 Acoustic Measurements

Acoustic measurement techniques utilized in this study include free-standing microphones and array-based methods. Both are discussed in this section.

3.4.1 Free-Standing Microphones

Two different sets of free-standing microphone data are acquired. The first is measured prior to the shortening of the UFAFF diffuser and the addition of an inlet silencer but is included in this analysis because multiple slot heights are tested. For that experiment, four G.R.A.S. Sound and Vibration (G.R.A.S.) 6.35 mm 40BE free-field microphones are placed outside the wind tunnel open jet shear layers. The microphones are oriented in pairs, two above and two below the airfoil, as shown in Figure 4. The G.R.A.S. microphones are calibrated using a Brüel & Kjær (B&K) 4231 Sound Calibrator at a frequency of 1 kHz. G.R.A.S. 40BE microphones are designed for a flat frequency response for $0°$ incidence with the protection grid installed. The frequency responses of all G.R.A.S. microphones used deviate by less than 1 dB (ref. 20μPa), so no corrections are applied to the measured spectra.

The second set of data are recorded simultaneously with the phased array, which is described in Section 3.4.2. Three microphones are placed above the trailing edge, as illustrated in Figure 5. The center microphone, labeled "M2" in Figure 5, is a G.R.A.S. 40BE, while the upstream ("M1") and downstream ("M3") microphones displaced 10.2 cm from the center microphone are B&K 4939 6.35 mm free-field microphones. All three microphones are approximately 1.12

m from the trailing edge. The microphones are calibrated using a B&K 4228 Pistonphone at a frequency of 250 Hz. The B&K microphones are designed for a flat frequency response for $0°$ incidence with the protection grid removed. Since the microphone grids remain installed, the frequency response of each B&K microphone is used to adjust the measured spectrum accordingly.

Various processing techniques are applied to the microphone data, including single microphone autospectra, coherent output power, and the three-microphone method (Brooks & Hodgson 1981; Hutcheson & Brooks 2002; Bahr *et al.* 2008; Bendat & Piersol 2000). These techniques are described in detail by Wetzel (2011).

3.4.2 Phased Array

Phased microphone arrays are used extensively for noise source assessment in aeroacoustic applications. A phased microphone array consists of a significant number of microphones strategically located in a frame or flush-mounted in a flat plate. The array is "focused" to a point of interest by appropriately weighting and delaying the microphones' signals in a process known as beamforming.

Beamforming The simplest and most straightforward beamformer is the delay-and-sum beamformer. Consider the illustration in Figure 6 of an array comprised of $m = 1, ..., M$ microphones and a scanning region of $l = 1, ..., L$ points located at $\vec{x}_l$, each assumed to be an incoherent and statistically independent monopole source. The estimated acoustic power at each location is given by the following equation 5 (Dougherty 2002; Yardibi *et al.* 2010a).

$$P_l = \frac{1}{M^2} \tilde{\mathbf{a}}_l^H \mathbf{G} \tilde{\mathbf{a}}_l \tag{5}$$

The weight, or steering, vector $\tilde{\mathbf{a}}_l$ compensates for the different propagation distances traveled by the sound wave from the scanning point $\vec{x}_l$ to the different microphones and is defined by Equation 6. The superscript ^{H} in Equation 5 corresponds to the Hermitian, or complex-conjugate transpose of this matrix.

$$\tilde{\mathbf{a}}_l = \frac{1}{r_{l,0}} \begin{bmatrix} r_{l,1} e^{-jkr_{l,1}} \\ r_{l,2} e^{-jkr_{l,2}} \\ \vdots \\ r_{l,M} e^{-jkr_{l,M}} \end{bmatrix} \tag{6}$$

In Equation 6, the distance from each scanning point l to each microphone m is designated $r_{l,m}$, and the distance from the array center to the lth scanning point is denoted $r_{l,0}$. Note that the $1/r_{l,0}$ factor is used to scale the power measured by each microphone to match the power that would be measured at the array center. Finally, $\mathbf{G}$ represents the estimated cross-spectral matrix (CSM) of the measured microphone signals.

Integrated spectra can be obtained by summing the powers of each scanning point and normalizing by the point-spread-function (PSF) of the array (Oelermans *et al.* 2007; Yardibi

et al. 2010*b*).

$$P_L = \frac{\sum_{l \in L} P_l}{\sum_{l \in L} PSF(l)} \qquad (7)$$

The PSF is the theoretical array response to a monopole placed above the center of the array at the same height as the scanning plane. In computing the power via Equation 7, only selected scanning points in a particular region of interest need to be evaluated, providing a means to "remove" noise sources other than the source(s) of interest.

Compared to the previously described methods, phased array measurements are much more expensive from cost, time, and computational standpoints. In addition, while relative sound levels from array integration can typically be trusted, absolute levels may be erroneously low due to coherence loss between microphones in the array, particularly at higher frequencies (Oelermans *et al.* 2007). However, unlike the conventional microphone techniques discussed earlier, phased arrays are extremely useful in identifying noise sources in a complex acoustic field.

Array setup A 60-element free-field nested microphone array is designed and built for the circulation control experiments. The inner, 7.62 cm aperture, 25-element array is designed for frequencies between 10 kHz and 80 kHz and is comprised of 10 B&K 4954B and 15 G.R.A.S. 40BE high-frequency microphones. The outer, 73.7 cm aperture, 40-element array is designed for frequencies below 10 kHz and is comprised of 35 B&K 4958 "array" microphones in addition to five shared G.R.A.S. 40BE microphones also part of the inner array.

The microphones are installed on a stereolithography frame with built-in microphone holders. The frame is wrapped in Nomex and foam to mitigate reflections caused by the frame and its mount. The array is installed in the anechoic wind tunnel 1.12 m below the airfoil's trailing edge and centered at midspan, as shown in Figure 5. A picture of the test setup along with pictures of the array are provided in Figure 7. Design microphone coordinates and the serial numbers of all microphones used are listed in Wetzel (2011).

Calibration The goal of array calibration is to characterize the magnitude and phase response of each microphone relative to the array center, or reference, microphone. The frequency response between each sensor and the reference is different due to the individual microphone responses and scattering from neighboring microphones and the sensor's own protective grid. The calibration procedure used in this investigation is described by Wetzel (2011).

3.4.3 Data Acquisition

All acoustic data are acquired at 204,800 Hz for 30 seconds. During processing, the data from each channel are separated into 480 blocks of 12,800 samples each, resulting in a 16 Hz bin width. The data are then processed using a Hanning window and 75% overlap, producing 996 effective averages and a normalized autospectral random uncertainty of 3.2%.

6

4 Fluid Dynamics

Even though the primary motivation for this research is acoustics, the fluid dynamics of the problem are equally important. Knowledge of the flow behavior is crucial to understanding the nature of the flow and theoretical noise sources, like those outlined by Howe (2002). Surface pressure measurements are used to provide insight into the flow around the airfoil. PIV is used to measure details of the flow field, including leading edge stagnation point movement and streamline curvature, the influence of the blowing slot on the trailing edge wake, characteristics of the turbulent boundary layer passing over the slot lip, and curved wall jet development and separation. Before the flow field is studied extensively, the circulation control airfoil is characterized.

4.1 Freestream Flow Characterization

The freestream flow field is characterized using a combination of static surface pressure and PIV measurements. The results from these tests are presented in this section.

4.1.1 Surface Pressure Measurements

Static surface pressure distributions are plotted in Figure 8 for three different momentum coefficients, $C_\mu = 0$, 0.015, and 0.057 at $Re_c = 6.5 \times 10^5$ and $h/c = 0.0019$. For clarity, uncertainty bounds are not included, as they are typically smaller than the datum point size. The effect of blowing on the C_p distribution is apparent by the large trailing edge suction peak whose magnitude increases substantially with larger values of C_μ. A leading edge suction peak typically observed in circulation control airfoil experiments, including those of Abramson (1975), is absent. Furthermore, the lift produced by the airfoil is substantially lower than the lift produced by Abramson's similar elliptic circulation control airfoil. Lift coefficients for a variety of momentum coefficients are compared in Figure 9. It is likely that the absence of the leading edge suction peak is the source of the lift deficiency observed in Figure 9.

4.1.2 Test Section Influence

To determine if the airfoil location in the test section is responsible for the missing leading edge suction peak, the airfoil position is varied by 13 cm vertically ($0.25c$) and 38 cm ($0.73c$) in the streamwise direction. However, the C_p distributions remain unchanged. Since the tests performed by Abramson (1975) took place in a closed wind tunnel, the absence of the leading edge suction peak could be due to the UFAFF open jet test section. To investigate this phenomenon further, the wind tunnel test section is enclosed with foam walls, as shown in Figure 10.

C_p data measured in the closed configuration are corrected to account for solid blockage

(Pope & Rae 1984). Specifically, C_p, C_μ, and Re_c are corrected using

$$C_{p,c} = \frac{C_p}{(1 + 2\epsilon_t)} \tag{8}$$

$$C_{\mu,c} = \frac{C_\mu}{(1 + 2\epsilon_t)} \tag{9}$$

$$Re_{c,c} = Re_c(1 + \epsilon_t) \tag{10}$$

where $\epsilon_t = 0.0357$ is one-quarter of the ratio between the model frontal area and test section cross-sectional area. Once again, for clarity, uncertainty bounds are not included, as they are typically smaller than the datum point size. Figure 11 compares midspan C_p distributions measured in both open and closed test sections for $C_\mu = 0$. Both C_p distributions have a similar shape, but the closed test section C_p distribution is noticeably offset from its open test section counterpart. Notably, the closed test section C_p data are more negative, indicative of the increased flow speed caused by the addition of a floor and ceiling and their containment of the tunnel jet.

Figure 12 compares open and closed test section C_p distributions for $C_\mu = 0.057$. Both C_p distributions have similar prominent trailing edge suction peaks associated with the trailing edge jet. However, at the leading edge, the C_p distributions are drastically different. The leading edge suction peak absent in the open test section configuration appears when the test section is fully enclosed. Lift coefficients for the closed test section and open test section cases are compared with data from Abramson (1975) in Figure 13. The closed test section lift curve is in close agreement with Abramson's lift values (Abramson applied the same blockage corrections used in the present analysis). Therefore, the wind tunnel open jet test section is responsible for the disappearance of the leading edge suction peak.

Since the primary motivation for this investigation is acoustics, it is concerning that the C_p distributions measured with an open and closed test section differ significantly. The mid-frequency circulation control noise source theorized by Howe (2002), passive-slot noise, is produced by freestream boundary layer turbulence scattering off the slot lip. If the characteristics of the turbulent boundary layer near the slot are highly-dependent on the flow upstream of the slot, then so too is the sound produced. PIV is used to further investigate the influence of the test section on the flow field, including the freestream boundary layer passing over the lip.

4.1.3 Closed Test Section Behavior

The leading edge flow field and the boundary layer flow passing over the slot lip are measured using PIV. Please refer to Wetzel (2011) for information regarding the experimental setup. In order to image the flow field, one foam sidewall is replaced with a clear polycarbonate panel. The PIV cameras are mounted behind this panel outside the flow. When the test section is fully enclosed, the foam ceiling is also replaced with a clear polycarbonate panel to permit the laser sheet to pass through and illuminate the flow. However, the tunnel floor remains foam. A picture of the test section enclosed for PIV measurements is provided in Figure 14.

Because the laser sheet can only illuminate the flow above the leading edge (a shadow region is created below the leading edge), the trailing edge jet is emitted from the lower blowing slot

so that any stagnation point movement occurs on the upper surface of the leading edge. The flow passing over the slot lip is of interest as well, so tests are repeated with upper slot blowing, since the light sheet also illuminates the flow above the upper surface lip. Thus, since the PIV experiments utilize both upper and lower slot blowing, it is important to compare C_p distributions for both.

Figure 15 compares C_p distributions for upper and lower slot blowing in the closed test section configurations. Surprisingly, there are substantial differences in the C_p distributions for upper and lower slot blowing when the test section is enclosed for PIV testing. With upper slot blowing (blowing on the same side as the polycarbonate ceiling), the C_p values are more negative. Figure 15 also reveals that the C_p data for lower slot blowing in the PIV test configuration (blowing on the same side as the foam floor) agree with the upper slot blowing C_p data obtained when the test section is fully enclosed with foam. Lower slot blowing experiments are not performed with the all-foam closed test section.

To rule out the blowing slots as the cause for these differences, C_p distributions for upper and lower slot blowing in the open test section are compared in Figure 16 for similar test conditions. The slight differences between the two distributions are minor, and it can be concluded that the variation in the C_p distributions in Figure 15 is not the result of dissimilar blowing between the upper and lower slots. Instead, it appears that the boundary conditions imposed by the tunnel surface on the same side as the blowing slot have a considerable influence on the flow field. A potential flow analysis is performed to provide insight into this observed flow behavior.

4.1.4   Potential Flow Analysis

A full description of the potential flow analysis, including MATLAB codes, is provided in Wetzel (2011). The approach is outlined in this section. Potential lifting flow over a cylinder in a freestream can be transformed to flow over an ellipse via conformal mapping (Panton 2005; Katz & Plotkin 2001). Consider the $z = x + iy$ plane whose origin is located at the center of a cylinder of radius R. The η plane, whose origin is located at the center of the ellipse, is defined by

$$\eta = z + \frac{a^2}{z},\tag{11}$$

where a is the transformation constant written in terms of the the cylinder radius R, the ellipse semi-major axis A, and the ellipse semi-minor axis B.

$$R = \frac{1}{2}(A + B)\tag{12}$$

$$a = \sqrt{\frac{1}{2}R(A - B)}\tag{13}$$

The complex potential for lifting flow around a cylinder of radius R is the summation of the potentials for a uniform freestream, a doublet, and a vortex.

$$F(z) = U_\infty\left(z + \frac{R^2}{z}\right) + \frac{i\Gamma \ln z}{2\pi}\tag{14}$$

9

Taking the derivative of Equation 14 yields the complex velocity.

$$W(z) = \frac{dF}{dz} = U_\infty \left(1 - \frac{R^2}{z^2}\right) + \frac{i\Gamma}{2\pi z} \tag{15}$$

To determine the surface pressure on an ellipse with circulation in a freestream, the complex velocity $W(z)$ must be transformed to $W(\eta)$ using the conformal mapping function given by Equation 11. Thus, it follows that,

$$W(\eta) = \frac{dF}{d\eta} = \frac{dF}{dz}\frac{dz}{d\eta} = \frac{dF}{dz}\frac{1}{\frac{d\eta}{dz}}, \tag{16}$$

and the complex velocity on the ellipse surface, where $z = Re^{i\theta}$, is given by

$$W(\eta) = \frac{U_\infty \left(e^{i2\theta} - 1\right) + \frac{i\Gamma}{2\pi R}e^{i\theta}}{e^{i2\theta} - \frac{a^2}{R^2}}. \tag{17}$$

Since $W(\eta) = u - iv$, the magnitude of the velocity on the surface and hence the C_p distribution along the surface of the ellipse can be computed.

$$C_p = 1 - \left(\frac{|\boldsymbol{V_s}|}{U_\infty}\right)^2 = 1 - \frac{u^2 + v^2}{U_\infty^2} \tag{18}$$

The aforementioned analysis can be extended to include rigid boundaries, like ground and ceiling planes, using the method of images (Katz & Plotkin 2001). Consider potential lifting flow around a circular cylinder placed a distance h_c from a ceiling plane. An "image" cylinder with circulation of opposite-sense from the real cylinder is "placed" a distance h_c from the opposite side of the plane. The origin of the real cylinder coincides with the origin of the $z_1 = x_1 + iy_1$ plane, and the origin of the image cylinder coincides with the origin of the $z_2 = x_2 + iy_2$ plane, which is offset from the z_1 plane such that $z_2 = z_1 - i2h_c$. The mapping transformation for the real cylinder is $\eta_1 = z_1 + a^2/z_1$, and the mapping transformation for the image cylinder is $\eta_2 = z_2 + a^2/z_2$. The complex potentials for the real and imaginary cylinders are given by the following equations.

$$F_1(z_1) = U_\infty \left(z_1 + \frac{R^2}{z_1}\right) + \frac{i\Gamma}{2\pi}\ln z_1 \tag{19}$$

$$F_2(z_2) = \frac{U_\infty R^2}{z_2} - \frac{i\Gamma}{2\pi}\ln z_2 \tag{20}$$

An expression is desired for the complex velocity of the flow around both ellipses as a function of η_1. For the real ellipse, this is straightforward and follows the steps outlined in the freestream flow analysis.

$$W_1(\eta_1) = \frac{dF_1}{dz_1}\frac{dz_1}{d\eta_1} = \left[U_\infty\left(1 - \frac{R^2}{z_1^2}\right) + \frac{i\Gamma}{2\pi z_1}\right]\frac{1}{1 - \frac{a^2}{z_1^2}} \tag{21}$$

The complex velocity for the image ellipse is

$$W_2(\eta_1) = \frac{dF_2}{dz_2}\frac{dz_2}{d\eta_2}\frac{d\eta_2}{d\eta_1}. \tag{22}$$

10

The distance between the cylinders and the distance between the ellipses are not the same, since

$$h_e = h_c + \frac{a^2}{h_c}. \tag{23}$$

Therefore, $\eta_2 = \eta_1 - 2ih_e$, $d\eta_2/d\eta_1 = 1$, and the complex velocity for the image ellipse is given by

$$W_2(\eta_1) = -\left(\frac{U_\infty R^2}{z_2^2} + \frac{i\Gamma}{2\pi z_2}\right)\frac{1}{1 - \frac{a^2}{z_2^2}}. \tag{24}$$

Substituting $z_2 = z_1 - 2ih_c$ and then writing both complex velocities in terms of $z_1 = Re^{i\theta}$ yields the following complex velocities.

$$W_1(\eta_1) = \frac{U_\infty\left(e^{i2\theta} - 1\right) + \frac{i\Gamma}{2\pi R}e^{i\theta}}{e^{i2\theta} - \frac{a^2}{R^2}} \tag{25}$$

$$W_2(\eta_1) = -\frac{1}{1 - \frac{a^2}{(Re^{i\theta} - 2ih_c)^2}}\left[\frac{U_\infty R^2}{(Re^{i\theta} - 2ih_c)^2} + \frac{i\Gamma}{2\pi(Re^{i\theta} - 2ih_c)}\right] \tag{26}$$

Finally, the complex velocity on the surface of the real ellipse is just the superposition of the image and real ellipse complex velocities,

$$W(\eta_1) = W_1(\eta_1) + W_2(\eta_1). \tag{27}$$

C_p is again computed using equation 18.

If a ground plane is present instead of a ceiling plane, then the only change to the previous analysis is that $z_2 = z_1 + 2ih_c$ and $\eta_2 = \eta_1 + 2ih_e$. The presence of both ground and ceiling planes is accounted for by an infinite number of image ellipses, since each image itself is reflected by the additional plane (Katz & Plotkin 2001). Thus, the complex velocity on the surface of the real ellipse between two planes is given by the following summation.

$$W(\eta_1) = \frac{U_\infty\left(e^{i2\theta} - 1\right) + \frac{i\Gamma}{2\pi R}e^{i\theta}}{e^{i2\theta} - \frac{a^2}{R^2}}$$
$$- \sum_{n=1}^{\infty}\frac{1}{1 - \frac{a^2}{(Re^{i\theta} - 2nih_c)^2}}\left[\frac{U_\infty R^2}{(Re^{i\theta} - 2nih_c)^2} + \frac{(-1)^{n+1}i\Gamma}{2\pi(Re^{i\theta} - 2nih_c)}\right]$$
$$- \sum_{n=1}^{\infty}\frac{1}{1 - \frac{a^2}{(Re^{i\theta} + 2nih_c)^2}}\left[\frac{U_\infty R^2}{(Re^{i\theta} + 2nih_c)^2} + \frac{(-1)^{n+1}i\Gamma}{2\pi(Re^{i\theta} + 2nih_c)}\right] \tag{28}$$

For moderate circulation, the lift coefficient computed from the results of Equation 28 converges to within three significant digits with well under 500 image ellipses considered. However, this result is largely dependent on the specified circulation, as convergence is established with as few as 20 images for certain lift values.

C_p distributions for potential lifting flow around a 20% ellipse in a variety of flow configurations are compared in Figure 17 for a freestream $c_l = 1.90$. Specifically, the impact of a ground plane, ceiling plane, and both ground and ceiling planes is assessed. The ground and ceiling planes are placed at the same distance from the ellipse, whose chord is identical to the airfoil

11

used in experiments, as the floor and ceiling installed in the UFAFF. Figure 17 reveals a few interesting details. First, the addition of a ceiling plane drastically augments the lift, whether or not a ground plane is present. Furthermore, the addition of a ground plane alone actually reduces the lift compared to the freestream case.

The potential flow analysis only assumes impermeable, rigid boundaries, whereas in actual testing, a combination of impermeable (polycarbonate) and porous (foam) boundaries are used. For this reason, while the potential flow results cannot be expected to match experiments exactly, the trends revealed by Figure 17 can still be applied to the measured observations. For example, Figure 17 indicates that the presence of an impermeable ceiling plane produces the greatest suction-side and lowest pressure-side C_p magnitudes, regardless of whether a ground plane is present, absent, or, hence, impermeable or porous. This agrees with the measured data presented in Figure 15, where the greatest suction-side and lowest pressure-side C_p magnitudes are observed when blowing is utilized on the same side as the polycarbonate tunnel ceiling. Additionally, Figure 15 shows little variation in the measured C_p distributions when blowing is utilized on the same side as the porous foam ceiling and the pressure-side boundary is either polycarbonate or foam. This agrees with the theory in Figure 17, which indicates that the presence of a ground plane has a minimal influence on the C_p distribution.

To further illustrate these trends, the potential flow solutions for the ellipse near a ground plane and ceiling plane alone are compared with measurements. Since the potential flow solutions do not account for the presence of the trailing edge jet and its contribution to the trailing edge suction peak, measured and computed C_p distributions cannot be compared using equivalent lift coefficients. Instead, the theoretical and measured distributions are matched at the leading edge stagnation points. The measured closed test section C_p distributions for blowing on the same side as and opposite side from the polycarbonate tunnel ceiling are compared to theory for flow with a ceiling plane and ground plane, respectively, in Figure 18. The measured leading edge stagnation points are found to match with theory for both data sets when the freestream lift coefficient is 1.90. At the leading edge, the theory agrees well with the measurements, and the trends revealed by Figure 17 are clearly followed by the measured data.

Further potential flow analysis indicates the differences between the computed closed test section and freestream surface pressure distributions are insignificant when the tunnel blockage ratio, computed from the ratio of the airfoil thickness to tunnel height, is less than 6%. By comparison, the tunnel blockage ratio for the present investigation is 14%, and the blockage ratios for studies by Abramson (1975) and Novak & Cornelius (1986) were 8% and 7%, respectively.

4.1.5 PIV Results

Although theory and measurements agree that there are large overall differences in the C_p distributions depending on the suction-side boundary condition, in general, enclosing the test section clearly produces the leading edge suction peak absent in the open test section measurements. The influence of enclosing the test section on the leading edge flow is captured by PIV. Mean flow streamlines for both open and closed test section configurations at a variety of lower blowing slot momentum coefficients are shown in Figure 19. In the open test section configuration, leading edge stagnation point movement and streamline curvature are minimal

as C_μ increases. Conversely, when the test section is enclosed, the leading edge stagnation point moves considerably with increasing C_μ, and streamline curvature is greatly enhanced.

The primary motivation for this research investigation is acoustics. It has been revealed that, upstream of the slot, the C_p distributions measured with the test section opened and closed differ significantly. Passive-slot noise is theorized by Howe (2002) to be produced by turbulence in the freestream boundary layer scattering off the slot lip. If the characteristics of the turbulent boundary layer near the slot vary with test section configuration, then so too does the sound produced. The turbulent boundary layer passing over the slot lip is measured using PIV in both open and closed tunnel configurations for a variety of upper slot blowing momentum coefficients. The results are presented in Figures 20, 21, and 22. Profiles of mean tangential and normal velocities, turbulence intensities, and Reynolds stress are plotted. For clarity, only every fourth datum point is displayed, and uncertainty bounds are represented by solid lines. Without blowing (Figure 20), the profiles are normalized using the local freestream velocity and the boundary layer thickness. With blowing (Figures 21 and 22), the mean tangential velocity profiles appear more like wall jet profiles, and the local maximum velocity and the boundary layer thickness based on where the velocity is $0.99U_{max}$ are used to normalize the data. For all cases, there are minor differences between the profiles, and these deviations are typically within the measurement uncertainty. From an acoustics perspective, the differences between the profiles should be negligible, and the sound produced by the interaction of the turbulent boundary flow with the slot lip should be the same whether or not the test section is opened or closed.

4.2   Curved Wall Jet Flow

The primary mechanism exploited by circulation control is the curved wall jet, which is expected to play an important role in the production of circulation control noise. Curvature noise is theorized by Howe (2002) to be produced by the interaction of boundary layer turbulence with the rounded trailing edge, and the scales required to assess Howe's model of this noise - the displacement thickness, mean velocity, and friction velocity - are clearly going to be dictated by the interaction of the curved wall jet with the freestream. Thus, there is a need for high-resolution flow measurements of the curved wall jet to determine these scales. Of greater importance and interest, however, is the potential for flow similarity. If the circulation control wall jet exhibits similarity, then it may be possible to predict the evolution of the flow and its various length and velocity scales. Such a finding would have direct application to Howe's model and also the design of circulation control airfoils for a variety of applications.

Unfortunately, the literature provides evidence that full flow similarity may only be possible for very specific geometries. Guitton & Newman (1977) presented a similarity solution for a curved wall jet in the absence of a freestream and concluded that full flow similarity is only possible if the surface is defined by a logarithmic spiral, e.g. $r \propto e^{R\theta/x}$ where R is the local radius of curvature, and x is the arc length from the origin. A logarithmic spiral is illustrated in Figure 23. Their analysis is extended in the next section for the curved wall jet with an external freestream.

4.2.1 General Similarity Solution

Using the turbulent forms of the governing equations in polar coordinates, Guitton & Newman (1977) developed a similarity solution for a curved wall jet in the absence of a freestream, assuming the following forms of the similarity functions f, g, and g_{12}.

$$u = U_{max} f'(\eta) \tag{29}$$

$$-\overline{u'v'} = U_{max}^2 g_{12}(\eta) \tag{30}$$

$$\overline{u'^2} - \overline{v'^2} = U_{max}^2 g(\eta) \tag{31}$$

$$\eta = \frac{y}{y_{1/2m}} \tag{32}$$

U_{max} is the local maximum velocity, and $y_{1/2m}$ is the local normal distance from the surface where the velocity is $\frac{1}{2}U_{max}$. Guitton and Newman showed that the wall jet flow can only be self-similar provided the surface is defined by a logarithmic spiral, $r \propto e^{R\theta/x}$. The ratio x/R dictates the rate at which the local radius of curvature, R, grows. The larger the value of x/R, the larger the local radius of curvature at some arc length x. Table 7 lists the relevant length and velocity scales and how each scales with arc length x.

With an external freestream, the velocity may never decay to $\frac{1}{2}U_{max}$. For such conditions, Launder & Rodi (1983) suggested the use of a defect velocity, defined as $U_{max} - U_e$, where U_e is the velocity where the Reynolds stress decays to a negligible value, and the length $y_{e,1/2}$, defined as the normal distance from the surface where the velocity is $\frac{1}{2}(U_{max} + U_e)$. These scales are illustrated in Figure 24. The analysis of Guitton & Newman (1977) is extended for a curved wall jet in the presence of a freestream by assuming the following arbitrary forms of the similarity functions.

$$u = U_1 f'(\eta) + U_2 \tag{33}$$

$$-\overline{u'v'} = U_1^2 g_{12}(\eta) \tag{34}$$

$$\overline{u'^2} - \overline{v'^2} = U_1^2 g(\eta) \tag{35}$$

$$\eta = \frac{y - y_2}{y_1} \tag{36}$$

If the scales suggested by Launder & Rodi (1983) are applied to similarity functions listed in Equations 33 to 36, then $U_1 = U_{max} - U_e$, $U_2 = U_e$, $y_1 = y_{e,1/2} - y_{max}$, and $y_2 = y_{max}$.

The remainder of the similarity analysis follows the same steps outlined by Guitton & Newman (1977) and is included in detail in Wetzel (2011). The similarity equation is

$$\begin{aligned}
&\frac{y_1}{U_1}\frac{dU_1}{dx}(f'^2 - f''f + 2g) - \frac{dy_1}{dx}(f''f + \eta g') - g_{12}' \\
&- \frac{y_1}{R}\left\{\frac{y_1}{U_1}\frac{dU_1}{dx}[A] + \frac{dy_1}{dx}[B] + (\eta g_{12}' + 2g_{12}) + \frac{y_1}{U_1}\frac{dU_2}{dx}[C] + \frac{dy_2}{dx}[D]\right\} \\
&+ \frac{y_1}{U_1}\frac{dU_2}{dx}(f' - \eta f'') - \frac{dy_1}{dx}\frac{U_2}{U_1}(\eta f'') + \frac{dy_2}{dx}\left[\frac{U_2}{U_1}(f'') - (g')\right] \\
&+ \frac{y_1}{U_1}\frac{U_2}{U_1}\left[\frac{dU_1}{dx}(f') + \frac{dU_2}{dx}\right] - \frac{y_2}{R}(g_{12}') = 0
\end{aligned} \tag{37}$$

14

where

$$A = \left(f'f + 2 \int_\eta^\infty f'^2 d\eta \right) + \frac{U_2}{U_1} \left(f + 4 \int_\eta^\infty f' d\eta \right) + 2 \int_\eta^\infty \left(\frac{U_2}{U_1} \right)^2 d\eta \tag{38}$$

$$B = \left(f'f + \int_\eta^\infty f'^2 d\eta \right) + \frac{U_2}{U_1} \left(f + \eta f' + 2 \int_\eta^\infty f' d\eta \right) - \left(\eta \left(\frac{U_2}{U_1} \right)^2 \right) + \int_\eta^\infty \left(\frac{U_2}{U_1} \right)^2 d\eta \tag{39}$$

$$C = (\eta f') + \frac{U_2}{U_1} \eta \tag{40}$$

$$D = \frac{U_2}{U_1} (f') - \frac{U_2^2}{U_1^2}. \tag{41}$$

When $U_2 = y_2 = 0$, Equation 37 reduces to the form of the similarity solution provided by Guitton & Newman (1977). In the general case, all terms outside the parentheses in Equation 37 must be constant. Consider the term,

$$\frac{dy_1}{dx} (f''f' + \eta g'). \tag{42}$$

Since dy_1/dx must be constant, it follows that $y_1 \propto x$. Similarly, note the term,

$$\frac{y_1}{R} (\eta g'_{12} + 2g_{12}). \tag{43}$$

Since y_1/R must be constant, then $R \propto y_1 \propto x$. Therefore, in order for true similarity to be achieved, the surface must be a logarithmic spiral, i.e. $r \propto e^{R\theta/x}$ where R is the local radius of curvature labeled in Figure 23. Table 7 lists the length and velocity scales from this analysis and how each scales with arc length x.

Since the trailing edge of the circulation control airfoil has a constant radius, complete self-similarity of the flow cannot be achieved in the present investigation. A log-spiral trailing edge is not practical for underwater vehicle applications where control surface symmetry is desired. In addition, a log-spiral design would likely interfere with the secondary blowing slot used to control excessive jet attachment at extremely high primary blowing slot momentum coefficients.

Although full flow similarity is not possible in the present investigation, even partial flow similarity could still prove useful. For instance, similarity of the mean tangential velocity alone would potentially provide a means of estimating the displacement thickness, mean velocity, and perhaps friction velocity required for Howe's model. Before the curved wall jet flow is examined for similarity, dimensional analysis is used to identify the dependent parameters in this investigation.

4.2.2 Dimensional Analysis

A dimensional analysis is performed to determine the important dimensionless parameters associated with the trailing edge flow field. As an example, the location of maximum velocity y_{max} is used as the relevant dependent length scale. Any other dependent length or velocity scale could be used in its place.

First, all significant parameters in the problem are identified. Note that the flow is assumed to be incompressible since $M_{jet} < 0.3$ for all cases considered. The geometric properties include

the chord c, slot height h, trailing edge radius r, and lip thickness l. Of these, the chord, trailing edge radius, and lip thickness are fixed in the current experimental investigation. Flow properties include density ρ, viscosity μ, freestream velocity U_∞, jet velocity U_{jet}, and y_{max}.

If c, U_∞, and ρ are chosen as the repeating parameters, the Π groups assembled are: $\Pi_1 = h/c$, $\Pi_2 = r/c$, $\Pi_3 = l/c$, $\Pi_4 = \rho U_\infty c/\mu = Re_c$, $\Pi_5 = U_{jet}/U_\infty$, and $\Pi_6 = y_{max}/c$. Π_5 can be recast into the momentum coefficient,

$$\Pi_5' = 2\Pi_1(\Pi_5)^2 = 2\left(\frac{h}{c}\right)\left(\frac{U_{jet}}{U_\infty}\right)^2 = C_\mu. \tag{44}$$

Note that the jet Reynolds number, defined as

$$Re_{jet} = \frac{\rho U_{jet} h}{\mu}, \tag{45}$$

is related to the chord Reynolds number, momentum coefficient, and slot height-to-chord ratio.

$$C_\mu = 2\left(\frac{c}{h}\right)\left(\frac{Re_{jet}}{Re_c}\right)^2 = 2\left(\frac{h}{c}\right)\left(\frac{U_{jet}}{U_\infty}\right)^2 \tag{46}$$

Hence, of C_μ, Re_{jet}, Re_c, and h/c, only three are independent. Therefore, the dimensionless length scales, such as y_{max}/c and velocity scales, like U_{max}/U_∞, are dependent on the following parameters.

$$\frac{y_{max}}{c} = f\left(\frac{h}{c}, \frac{r}{c}, \frac{l}{c}, C_\mu, Re_c\right) \tag{47}$$

As noted earlier, r/c and l/c are constant in the present investigation. However, h/c, C_μ, and Re_c are variable. Thus, two of these three parameters can be kept constant, and the effect of varying the third parameter on y_{max} and other length and velocity scales can be studied.

Table 3 summarizes the six different cases that are included in this study of the curved wall jet. Cases one through three represent tests where Re_c and h/c are fixed, but C_μ changes. In cases four and five, C_μ and h/c are fixed, but Re_c varies. Finally, in cases four and six, C_μ and Re_c are fixed, but h/c differs. In the following sections, results from these six cases are presented and discussed.

4.2.3 Flow Characteristics

Before studying the PIV measurements of the curved wall jet, the surface pressure along the Coanda surface is examined. Trailing edge C_p data for the cases listed in Table 3 are plotted in Figure 25. Initially, a favorable pressure gradient accelerates the flow for all cases except $C_\mu = 0.0039$, where $U_{jet} \approx U_\infty$. Shortly thereafter, near $r\theta/c = 0.02$, a strong adverse pressure gradient develops. The trends displayed in Figure 25 follow similar findings reported by Novak *et al.* (1987). Trailing edge C_p provides insight into the expected similarity, or lack thereof, of the curved wall jet flow. In their study of a curved wall jet in the absence of a freestream, Neuendorf & Wygnanski (1999) observed full similarity of $\bar{U}$ (inner and outer regions) in the constant pressure region but only outer region similarity of $\bar{U}$ in the adverse pressure gradient region.

16

Profiles of mean velocity ($\bar{U}$ and $\bar{V}$), turbulence intensity ($(\overline{u'^2})^{1/2}$ and $(\overline{v'^2})^{1/2}$), and Reynolds stress ($\overline{u'v'}$) from PIV measurements along the rounded trailing edge are plotted in Figure 26 at a variety of downstream distances from the slot for $Re_c = 6.5 \times 10^5$, $h/c = 0.0019$, and $C_\mu = 0.0039$, 0.015, and 0.057. Profiles are not included for $C_\mu = 0.0039$ after $r\theta/c = 0.040$ because separation occurs upstream of that position. The distance from the surface is normalized using the slot height h, and the flow quantities are normalized using the jet velocity U_{jet}. Uncertainty bounds are removed from the plots for clarity. The mean tangential velocity profiles reveal how the jet decays and spreads as it travels away from the slot. As $\bar{U}$ decays, the mean normal velocity $\bar{V}$ increases and separation is approached. The turbulence intensities and Reynolds stress are significant in the immediate vicinity of the blunt slot lip and the high-shear region that exists there. As the jet spreads and entrains fluid from the freestream, Reynolds stress becomes non-negligible over a growing region of the trailing edge. The similarity of the measured curved wall jet flow is assessed in the following section.

4.2.4 Flow Similarity

Novak & Cornelius (1986) and Novak *et al.* (1987) showed that the outer region of $\bar{U}$ along the trailing edge of their circulation control airfoil exhibited similarity when normalized using the scales suggested by Launder & Rodi (1983) (refer to Figure 24). These same scales are applied to the current data set in order to determine if similarity is achieved. In addition, the data is normalized using the scales found by Zhou & Wygnanski (1993) to collapse the outer region of $\bar{U}$ for a plane wall jet in an external freestream. Those scales include local U_{max}, U_∞, y_{max}, and $y_{m/2}$, which is the normal distance where $\bar{U} = \frac{1}{2}U_{max}$. In the current set of experiments, U_∞ is replaced with U_{min}, the velocity where the outer region mean shear approaches zero, and $y_{m/2}$ is replaced with $y_{m,1/2}$, the normal distance where $\bar{U} = \frac{1}{2}(U_{max} + U_{min})$, since the velocity does not always decay to values of $\frac{1}{2}U_{max}$. These scales are illustrated in Figure 27.

To normalize the flow profiles, the various length and velocity scales described must first be determined. U_{max} is found by detecting the point of maximum velocity in each profile, fitting a Gaussian curve to this point and its adjacent four neighbors, and then finding the maximum of the Gaussian curve. With U_{max} known, y_{max} is determined. To find y_{min}, the mean shear ($d\bar{U}/dy$) is computed starting at y_{max} and moving outwards from the surface until the sign of the shear flips, and then a third-order polynomial is fit to the two points on either side of the zero-crossing, and the exact zero-crossing is determined and set as y_{min}. For a few profiles, the shear never changes sign in the outer region. In those situations, y_{min} is specified as the first instance where $(h/U_{jet})(d\bar{U}/dy) < 4 \times 10^{-6}$ (or $\bar{U}/U_{jet}$ changes by less than 6×10^{-4}). This particular shear threshold is determined by inspection of the data. With y_{min} specified, U_{min} is found by evaluating a third-order polynomial fit of the velocity data at y_{min}. $U_{m,1/2}$ is computed once U_{max} and U_{min} are known, and then $y_{m,1/2}$ is determined by a piecewise cubic interpolation along all the points between y_{max} and y_{min}. To determine y_c, first, $\overline{u'v'}_{max}$ is determined in similar fashion to U_{max} using a Gaussian curve fit. Then the first instance where $\overline{u'v'}/(\overline{u'v'})_{max} < 0.05$ (this value is also chosen by inspection; slightly higher thresholds do not significantly affect the results) above the position of maximum Reynolds stress is deemed the negligible Reynolds stress location. A third-order polynomial fit of the velocity data is then

evaluated at this location to determine U_e. $U_{e,1/2}$ follows the same approach used to find $U_{m,1/2}$.

The length scales y_{max}, y_{min}, y_e, $y_{m,1/2}$, and $y_{e,1/2}$ are plotted with the mean tangential velocity and Reynolds stress profiles for $C_\mu = 0.015$ in Figure 28. Profiles are provided from $r\theta/c = 0.0027$ until just past separation at $r\theta/c = 0.047$. As Figure 28 attests, there is little difference between y_{min} and y_e and $y_{m,1/2}$ and $y_{e,1/2}$.

The scales are used to normalize the outer region of the mean tangential velocity profiles in Figure 29, where it is seen that, using either the scaling suggested by Launder & Rodi (1983) or the modification to the approach by Zhou & Wygnanski (1993), the outer streamwise profiles exhibit similarity. Note that the velocity data at $r\theta/c = 0.0027$ are not included, as they do not collapse with the other profiles. In fact, only profiles in the constant pressure or adverse pressure gradient region along the trailing edge exhibit similarity, agreeing with the observations of Neuendorf & Wygnanski (1999), Novak & Cornelius (1986), and Novak *et al.* (1987). The solid line in Figure 29 represents a hyperbolic tangent of the form

$$U = 0.5 \left[1 - 1.315 \tanh(y^- 1) \right],\tag{48}$$

where U and y are the normalized velocity and distance from the surface, respectively.

Now that the outer region of $\bar{U}$ has been found to exhibit similarity, the inner region of $\bar{U}$ is studied. It is difficult to measure extremely close to the surface with PIV (recall, the slot height is typically 1 mm), so inner region data are limited compared to the outer region of the flow. Nevertheless, there are sufficient data to determine whether or not similarity is achieved. Inner region $\bar{U}$ data are normalized using y_{max} and U_{max} and plotted in Figure 30. Unlike the outer region, the inner region does not exhibit similarity. These results agree with Neuendorf & Wygnanski (1999), who found that the inner region of $\bar{U}$ for a curved wall jet in quiescent surroundings does not exhibit similarity in the adverse pressure gradient region.

The remaining flow profiles, $\bar{V}$, $(\overline{u'^2})^{1/2}$, $(\overline{v'^2})^{1/2}$, and $\overline{u'v'}$, also do not exhibit similarity using any combination of mean velocity and length scales. However, the similarity of $\bar{U}$ in the outer region alone may permit the prediction of that portion of the flow and subsequently the mean tangential velocity scales, which are required to assess Howe's model (Howe 2002). In addition, knowledge of y_{max} may be useful in providing at least a rudimentary prediction of the local displacement thickness. In the following section, the length and velocity scales found to collapse the outer region of $\bar{U}$ are analyzed for the six cases listed in Table 3.

4.2.5 Length and Velocity Scales

The set of length and velocity scales based on the mean shear found to sufficiently collapse the outer streamwise profiles do not require knowledge of the flow turbulence and are thus more practical in application. As such, they are the focus of the remainder of the analysis. The length and velocity scales associated with this approach, y_{max}, $y_{m,1/2}$, U_{max}, and U_{min}, are plotted in increments of $r\theta/c = 0.002$ for $C_\mu = 0.015$ in Figure 31. The data are plotted from just downstream of the slot exit to separation, detected by the first sign of flow reversal. Figure 31 further illustrates the development and spread of the jet. The velocity scales initially increase, reach a maximum value near $r\theta/c = 0.015$, then decay at similar rates. The length scales y_{max}

18

and $y_{m,1/2}$ are nearly constant initially, then increase gradually, and finally grow sharply as separation is approached. On the other hand, y_{min} increases immediately and then follows a parabolic form, similar to the other length scales.

For all test cases listed in Table 3, the trends of y_{max}, $y_{m,1/2}$, U_{max}, and U_{min} are analyzed in an attempt to collapse each set of curves. Only data where the outer region exhibits similarity is included. Neuendorf & Wygnanski (1999) found that, for a curved wall jet in the absence of a freestream, the decay of U_{max} and the rate of spread of the jet described by the location where $U = \frac{1}{2}U_{max}$ could be scaled using the local kinematic jet momentum,

$$ J = U_{max}^2 \, y_{m/2} \int_{y/y_{m/2}=0}^{\infty} \left(\frac{\bar{U}}{U_{max}} \right)^2 d \left(\frac{y}{y_{m/2}} \right) = 0.78 U_{max}^2 \, y_{m/2}. \tag{49} $$

and the wall radius in the constant pressure region. However, unlike the curved wall jet of Neuendorf and Wygnanski, the entire velocity profile of the circulation control curved wall jet does not exhibit similarity. Hence, the local kinematic jet momentum cannot be expected to collapse the scales. Likewise, Neuendorf and Wygnanski observed that the rate of spread could be expressed solely as a function of the wall radius and downstream angular position from the slot. This is clearly not observed for the circulation control airfoil, as shown in Figures 32 and 33. For a planar wall jet in an external freestream, Zhou & Wygnanski (1993) found that the length and velocity scales describing the planar wall jet's spread and decay could be expressed as a function of a normalized downstream distance from the slot defined by XJ/ν^2, where X is the dimensional distance from the slot, ν is the kinematic viscosity, and $J = h(U_{jet} - U_\infty)U_{jet}$ is the excess of kinematic momentum flux near the nozzle. A dimensionless velocity ratio $(U_{jet} - U_\infty)/(U_{jet} + U_\infty)$ was also used. These parameters do not collapse the current data set either. Instead, the data are best fit using Re_c, C_μ, and h/c, as shown in Figures 32 through 35. A power law curve is fit to each data set by minimizing the square of the error. The scales, as a function of $r\theta/c$, are found to collapse with the product of Re_c and C_μ, referred to as the Reynolds corrected momentum coefficient, which has recently been found to scale lift increments for active control of airfoil flow separation (Stalnov & Seifert 2010). This scaling parameter takes into consideration the freestream boundary layer and its development as a function of Re_c. Recall Figures 21 and 22, where at higher values of C_μ, the mean tangential velocity profile of this upstream "boundary layer" does not actually resemble a conventional boundary layer. The Reynolds corrected momentum coefficient provides some basis to account for this effect. Best-fit equations for the length and velocity scales are provided in Equations 50 to 53.

$$\frac{y_{max}}{h} = \frac{1}{(C_\mu Re_c)^{0.60}} \left[9.0 \times 10^{10} \left(\frac{r\theta}{c} \right)^{6.1} + 110 \right] \tag{50}$$

$$\frac{y_{m,1/2}}{h} = 2.6 \times 10^{10} \left[\frac{1}{(C_\mu Re_c)^{0.11}} \frac{r\theta}{c} \right]^{5.7} + 1.0 \tag{51}$$

$$\left(\frac{U_{jet}}{U_{max}} \right)^2 = \left(\frac{h}{c} \right)^{-0.80} \left\{ 7.0 \times 10^6 \left[\frac{1}{(C_\mu Re_c)^{0.10}} \frac{r\theta}{c} \right]^{4.9} + 0.005 \right\} \tag{52}$$

$$\left(\frac{U_{jet}}{U_{min}} \right)^2 = \left(\frac{h}{c} \right)^{-0.65} \left\{ 3.0 \times 10^{11} \left[\frac{1}{(C_\mu Re_c)^{0.18}} \frac{r\theta}{c} \right]^{5.9} + 0.04 \right\} \tag{53}$$

Equations 50 and 51 reveal approximately a 6th power dependence on the arc length $r\theta/c$. Contrast that to the results of the general similarity solution, which indicates that, for the self-similar flow over a log spiral surface, these scales should have a linear relationship with the arc length.

The product of the chord Reynolds number and momentum coefficient can also be rearranged as the product of the jet Reynolds number and jet-to-freestream velocity ratio.

$$Re_c C_\mu = \left(\frac{U_\infty c}{\nu} \right) \left[2 \left(\frac{h}{c} \right) \left(\frac{U_{jet}}{U_\infty} \right)^2 \right] = 2 \frac{U_{jet} h}{\nu} \frac{U_{jet}}{U_\infty} = 2 Re_{jet} \frac{U_{jet}}{U_\infty} \tag{54}$$

Thus, in the case of the circulation control airfoil, it appears that the rate of decay and spread of the jet are dependent on the jet Reynolds number. This is in stark contrast to the findings of Zhou & Wygnanski (1993), who determined that, as long as $U_{max}/U_\infty > 2$, the length and velocity scales describing the planar wall jet in an external freestream are independent of the jet Reynolds number. Note that $U_{max}/U_\infty > 2$ for some profiles in cases 2 through 5 listed in Table 3.

Equations 50 to 53 provide a predictive capability for the length and velocity scales of the mean outer region flow. Predicted and measured scales are compared in the next section.

4.2.6 Flow Prediction

A comparison of the predicted and measured length and velocity scales is presented in Figure 36 for $Re_c = 6.5 \times 10^5$, $C_\mu = 0.015$, and $h/c = 0.0019$. Overall, the agreement between the measured and predicted scales is good. U_{min} is initially over-predicted in the favorable pressure gradient region, but recall, only data in the adverse pressure gradient region, where the outer region of $\bar{U}$ is similar, is used to determine Equations 50 to 53. Despite that fact, the other scales are predicted reasonably well in the favorable pressure gradient region.

While the agreement between the predicted and measured flow fields in Figure 36 is promising, it is a rather expected result since, after all, the data for those test conditions are used in determining the prediction equations. To truly test the prediction's capabilities, it should be compared to measurements for a case not included in the prior analysis. Thus, the predicted and measured scales are compared in Figure 37 for $Re_c = 1.3 \times 10^6$, $C_\mu = 0.014$, and $h/c = 0.0029$. Although there are larger differences between the predicted and measured scales in comparison

20

with Figure 36, the overall agreement is fair.

To this point, the curved wall jet flow has only been considered prior to separation. In the next section, flow separation is discussed.

4.2.7 Separation and Stability

It is well known that the circulation control curved wall jet is responsible for entraining freestream fluid, delaying separation and increasing circulation. The cause of separation is perhaps less clear, and could be the result of a severe adverse pressure gradient (see Figure 25), meandering streamwise vortices, observed in curved wall jets absent of a freestream by Likhachev *et al.* (2001), Neuendorf *et al.* (2004), and Han *et al.* (2006), or a combination of influences.

Separation is first studied in the present investigation by using PIV to measure the trailing edge flow field and part of the wake region. Mean speed contours and mean velocity vectors are presented for $C_\mu = 0$, 0.014, and 0.057 in Figure 38. When $C_\mu = 0$, a large wake is formed aft of the trailing edge, and the freestream flow appears symmetric about the chordline. With blowing, the flow along the upper surface of the airfoil remains attached and separates much farther downstream, as shown in Figure 38B. The vectors reveal the extent of flow turning due to entrainment from the jet. As C_μ further increases to 0.057 in Figure 38C, the freestream is deflected even more, and the separation point is shifted farther away from the blowing slot.

Figure 38 only provides a qualitative description of flow separation. For a more quantitative analysis, the curved wall jet PIV data are used to estimate the separation location by detecting the onset of flow reversal near the surface. Data along the trailing edge surface are analyzed in increments of 0.13 mm, which corresponds to the vector resolution of the data set. Also, since it is not possible to resolve the flow field very near the surface with PIV, the separation locations presented can only be regarded as estimates, and the true separation location likely occurs just upstream of the estimated location. The separation locations are plotted as a function of $C_\mu Re_c$ in Figure 39, which indicates that the separation location moves farther downstream from the slot as the product of the chord Reynolds number and momentum coefficient increases. In particular, as $C_\mu Re_c$ initially increases, the separation distance increases at a high rate, but at larger values of $C_\mu Re_c$, a significant increase in the product of the two parameters yields only a small delay in separation. A curve, whose equation is given by Equation 55, is fit to this data so the separation distance can be estimated for a given Reynolds corrected momentum coefficient. Equation 55 accurately predicts the separation locations for both cases considered in Section 4.2.6 with an error of less than 2% .

$$\frac{r\theta_{sep}}{c} = 0.0085 \left(C_\mu Re_c\right)^{0.184} \tag{55}$$

It should be noted that Equation 55 appears to be only applicable to the airfoil geometry of the present investigation. Attempts to predict the separation locations reported by Novak & Cornelius (1986) and Novak *et al.* (1987) result in errors of just under 50% (or $\theta = 65°$). However, the trailing edge geometry of the circulation control airfoil studied by Novak and his colleagues is significantly different from the trailing edge of the circulation control airfoil in the present investigation. Furthermore, Equation 55 is only accurate for $Re_c > 0$. With no

freestream, the curved wall jet flow separates well downstream of the blowing slot.

The mechanism causing separation has garnered much attention over the last decade. Recent work by Likhachev et $al.$ (2001), Neuendorf et $al.$ (2004), and Han et $al.$ (2006) has revealed that meandering streamwise vortices are likely the culprits of curved wall jet flow separation. Floryan (1986) determined the inviscid stability criterion for boundary layer and wall jet flows over convex surfaces, given by

$$\frac{d\bar{U}^2}{dy} > 0. \tag{56}$$

Since the wall jet profile is non-monotonic, whether or not a freestream is present, it automatically violates the inviscid stability criterion. In particular, $d\bar{U}^2/dy < 0$ in the outer region of the profile where the velocity decays. Therefore, the outer region of the wall jet flow over a convex surface is potentially unstable and susceptible to the formation of "Görtler vortices" (Floryan 1986; Saric 1994). Floryan also performed a viscous stability analysis and provided a neutral stability curve for the Görtler number, which he found to be a function of the maximum velocity, boundary layer thickness, kinematic viscosity, and curved wall radius.

$$G = \frac{U_{max}\delta}{\nu} \left(\frac{\delta}{r}\right)^{1/2} \tag{57}$$

Floryan (1986) defined the boundary layer thickness by

$$\delta = \left(\frac{\nu r \theta}{U_{max}}\right)^{1/2}. \tag{58}$$

The Görtler number is evaluated as a function of downstream distance from the slot for $Re_c = 6.5 \times 10^5$, $C_\mu = 0.015$, and $h/c = 0.0019$. The results are plotted against the neutral stability curve computed by Floryan in Figure 40 and indicate that beyond $r\theta/c = 0.0047$, the flow is unstable to disturbances of critical wavelengths indicated by the region of the figure labeled "unstable," where $\alpha = 2\pi\delta/\lambda$ is a dimensionless wavenumber and λ is the disturbance wavelength. For reference, the Görtler number at the separation location is also included. These "Görtler" vortices are expected to be centered about the outer region of the velocity profile, or along $y_{m,1/2}$ (Floryan 1986).

Crossflow PIV is used to detect the presence of streamwise vortices by illuminating a crossflow plane normal to the trailing edge surface 13 mm downstream from the blowing slot, or $r\theta/c$ = 0.025. Initially, measurements are attempted at the same test conditions used to evaluate the Görtler number in Figure 40. However, to boost the jet seed density and image quality, the chord Reynolds number is reduced to $Re_c = 5.6 \times 10^5$ while maintaining $C_\mu = 0.014$ and h/c = 0.0019. The drop in Reynolds number reduces the mass flow rate required to maintain the desired C_μ and hence increases the seed density, but since the momentum coefficient remains constant, the same jet-to-freestream velocity ratio is maintained ($U_{jet}/U_\infty = 2$). Counter-rotating pairs of vortices, much like those described by Neuendorf et $al.$ (2004), are readily visible in the acquired image pairs and typically located between one-half and one-and-a-half slot heights from the surface. An instantaneous snapshot of the spanwise vorticity computed from an image pair is presented in Figure 41 and shows multiple regions of positive and negative

vorticity, often located in pairs. A smaller region of the flow is extracted in Figure 42, where a counter-rotating pair of vortices is clearly present. The axes of the vortices are located between $0.9 < y/h < 1.3$, which, based on the results of the curved wall jet analysis for the same C_μ and $Re_c = 6.5 \times 10^5$, likely place the vortices in the outer region of the streamwise flow field.

Neuendorf *et al.* (2004) and Han *et al.* (2006) hypothesize that these vortices lead to separation by "lifting" the flow off the surface. Consider the counter-rotating pair of vortices in Figure 42. Since these vortices are located in the outer region of $\bar{U}$, they "pull" lower-momentum fluid from the freestream towards the surface and "push" the higher-momentum fluid located near y_{max} away from the surface. In contrast, vortex generators are commonly placed in boundary layer flows to produce streamwise vorticity that "pulls" the higher-momentum freestream fluid towards the surface and "pushes" the lower-momentum near-boundary fluid away, delaying separation. The streamwise vortices produced in the outer region of the curved wall jet do just the opposite and actually have implications to possible noise-abating treatments. Recall Slomski (2009) numerically evaluated the effect of serrating the slot lip to reduce lip tones by breaking up the coherent spanwise vortices shed from the lip. It is possible that the saw-tooth serration pattern could introduce these vortices upstream from where they naturally occur, causing the flow to separate earlier. Since the computational domain evaluated by Slomski did not include the separation region, the influence of the serrations on flow separation could not be definitively assessed.

4.3   Summary

Fluid dynamic measurements reveal a great extent about both the freestream and circulation control curved wall jet flows. C_p measurements of the circulation control airfoil in the open jet test section of the UFAFF lack a leading edge suction peak typically observed in closed test section measurements. Enclosing the test section causes the leading edge peak to emerge but does not change the freestream boundary layer flow passing over the slot lip. The influence of different wall boundary conditions on the C_p distribution is also examined using data and potential flow theory. The curved wall jet flow is measured using PIV and found to exhibit similarity in the outer region of $\bar{U}$ only. However, this alone permits the development of equations to predict the length and velocity scales required for similarity as a function of Re_c, C_μ, and h/c. Finally, flow separation is found to be dependent on the product $C_\mu Re_c$, and streamwise vortices theorized to promote separation are observed in crossflow PIV measurements.

The fluid dynamic measurements also provide insight with regards to acoustics. Since the turbulent boundary layer passing over the slot lip is independent of the test section configuration, the sound produced by the interaction of the flow with the airfoil trailing edge should be independent of the test section configuration as well. The similarity of the curved wall jet flow makes prediction of some of the scales required for Howe's model possible, particularly in the assessment of curvature noise (Howe 2002). Finally, serrating the slot lip for noise reduction may cause earlier flow separation by instigating the production of streamwise vortices in the outer region of the flow.

5 Acoustics

The focus of this section is findings from acoustics measurements. First, the presence and scaling of tones is discussed. Then, results from phased array measurements are presented in order to identify the primary noise sources under different test conditions. Different measurement and processing techniques are used to estimate the broadband noise spectrum. Finally, Howe's model of circulation control acoustics is compared with a measurement (Howe 2002).

5.1 Tones

Acoustic tones are undesirable for underwater vehicle applications and a potential hurdle for the application of circulation control to underwater vehicles. The presence of tones is evaluated using microphone "M1" from the test setup illustrated in Figure 4. Figure 43 includes spectra for a variety of momentum coefficients at $Re_c = 6.5 \times 10^5$ and $h/c = 0.0019$. The spectra reveal both low and high frequency tones under certain conditions. These tones are evaluated further in the following sections.

5.1.1 Low Frequency Tones

Spectra from all test cases where a low frequency tone is measured are plotted together in Figure 44. The tests included cover variations in C_μ, Re_c, and h/c. The frequency axis is normalized using the Strouhal number,

$$St = \frac{2y_{TE}}{U_\infty}, \tag{59}$$

which has a nominal value of 0.21 for vortex shedding from a blunt edge. The length scale y_{TE} = 4.6 cm, the thickness of the trailing edge at the slot exit plane, is used as the reference length scale. The tones plotted in Figure 44 collapse at a Strouhal number just above 0.21, indicating that these low frequency tones are produced by vortex shedding from the round airfoil trailing edge.

With sufficient blowing, these tones are not measured. Using just a single blowing slot, the tones are eliminated if $C_\mu \geq 0.002$.

5.1.2 High Frequency Tones

Previous research cited the presence of high frequency tones thought to be attributed to vortex shedding from the slot lip (Slomski 2009). Microphones placed in the UFAFF measure high frequency tones at a variety of frequencies and amplitudes. A sampling of these tones is provided in Figure 45 for $C_\mu = 0.014$ and $h/c = 0.0029$. The frequency axis is again normalized by the Strouhal number, this time defined by

$$St = \frac{fl}{U_{jet}}, \tag{60}$$

where l is the lip thickness. The Strouhal number of the tones are in close agreement near 0.21, and it is concluded that these tones are produced by vortex shedding from the slot lip.

These "lip" tones are only, but non necessarily, produced when both freestream and jet flows exist. However, exact conditions corresponding to the generation of lip tones could not be determined. No clear trends between the appearance or magnitude of the tones and flow parameters such as Re_c, C_μ, h/c, and Re_{jet} are found. The directionality of the tones is assessed to some extent using the microphones placed on the opposite side from the blowing slot. The levels of the tones measured by these microphones are at most only slightly above broadband noise levels, as shown in Figure 46.

With both vortex shedding tones experimentally verified, focus shifts towards broadband noise and noise source identification.

5.2   Assessment of Noise Sources

As discussed in Section 3.4, a single microphone is unable to discern between multiple acoustic sources. Furthermore, pairs or triads of microphones are unable to distinguish between multiple correlated noise sources. Phased acoustic arrays are, on the other hand, distinctly useful for identifying noise sources. Results from phased array measurements of the circulation control airfoil are presented in this section. Cases with only freestream flow, only jet flow, and both flows are examined.

5.2.1   In the Absence of a Freestream

The circulation control jet is first considered in the absence of a freestream. Recall Figure 16, which reveals that the C_p distributions for upper and lower slot blowing are nearly identical in the tunnel open test section configuration. It is reasonable to assume that, since the C_p distributions are similar, the trailing edge blowing slot flows and the sound they produce are also comparable. Thus, before beam maps are discussed, consider the spectra shown in Figure 47, presented as sound pressure level (SPL) in dB, where

$$SPL = 10 \log_{10} \left(\frac{\hat{G}_{yy}(f)\Delta f}{p_{ref}^2} \right). \tag{61}$$

Δf is the bin width of the processed spectrum. These spectra are measured by the center microphone placed above the airfoil for cases where the blowing slot on the same side as the microphone is used, and this is referred to from this point forwards as same side blowing (SSB). Furthermore, the cases presented in Figure 47 are similar to SSB cases analyzed with the phased array. Upper microphone spectra are considered in place of the spectra from the array center microphone since the array microphone suffers from significant inter-microphone scattering at higher frequencies. The vertical lines in Figure 47 signify the octave frequencies where beam maps are generated, notably 1 kHz to 64 kHz. Notice that when $Re_{jet} = 1380$, the sound generated is hardly distinguishable from the noise floor. Hot-wire data used to characterize slot flow uniformity indicate that the jet is just becoming turbulent at $Re_{jet} = hU_{jet}/\nu = 2600$. According to Howe (2002), slot-jet interaction noise is eliminated if the jet is laminar.

Beam maps, like the example displayed in Figure 48, are presented for a variety of jet Reynolds numbers in Figures 49 through 55. Each beam map includes overlays with the airfoil,

sidewalls, inlet, and diffuser, as illustrated in Figure 48. All measurements represent cases where the blowing slot on the same side of the airfoil as the array is used. The array point spread function (PSF) is also shown in each figure as reference for the array resolution. CSM diagonal removal is applied during beamforming to eliminate microphone self-noise and channel noise (Dougherty 2002). Propagation times are not corrected for shear layer refraction because of the unknown effect of the blowing jet on the tunnel shear layer (Amiet 1978). Beam maps are presented in absolute dB (ref. 20μPa) for comparison between different test conditions. The scanning plane is located along the chordline, 1.12 m above the array.

By and large, in the absence of a freestream, the trailing edge is the dominant noise source at all frequencies, provided the jet Reynolds number is sufficiently large. When $Re_{jet} = 1340$, the trailing edge noise is not uniform or no single source is apparent. However, the levels are also extremely low in comparison with the higher Re_{jet} cases, agreeing with the hot-wire data that indicates the jet is just becoming turbulent when $Re_{jet} = 2600$. When $Re_{jet} = 2680$, the trailing edge is the lone dominant source, although the sound power is not distributed uniformly along the trailing edge at frequencies of 4 kHz and 8 kHz. In addition, the levels are also extremely low above 16 kHz. When $Re_{jet} = 3980$ and higher, the trailing edge is the principal noise source, the power is generally distributed uniformly along the trailing edge, and levels increase with Re_{jet}.

Having identified the trailing edge as the primary noise source in the absence of a freestream, the array is used to identify noise sources with the addition of the tunnel freestream.

5.2.2   With a Freestream

The addition of a freestream may produce contaminating noise sources. Potentially harmful noise sources include sidewall scrubbing noise and diffuser flow impingement noise, which was severe enough in prior experiments in the UFAFF, that it motivated the removal of a meter-long section of the diffuser to further separate it from microphones and arrays (Bahr 2010). If these noise sources are present, then the array provides insight into their strengths relative to the sources of interest and the frequencies at which they may be problematic.

Following the pattern of the previous section, before beam maps are provided, consider the upper microphone spectra measured for upper slot blowing test conditions plotted in Figure 56 for a variety of momentum coefficients at $Re_c = 6.5 \times 10^5$. Like the jet-only spectra, the spectrum for $Re_{jet} = 0$ $(C_\mu = 0)$ is nearly identical to the $Re_{jet} = 1330$ $(C_\mu = 0.004)$ spectrum. When $C_\mu = 0.015$ $(Re_{jet} = 2660)$, there is some increase in SPL at frequencies below 1 kHz and above 10 kHz, but in between the difference is marginal. As C_μ increases further, the sound levels increase over all frequencies.

Beam maps are provided in Figures 57 to 63 for octaves between 1 kHz and 64 kHz. The cases again represent SSB. Diagonal removal is used, but a shear layer correction is not. The scanning region is located 1.12 m above the array, along the airfoil chordline. Array PSFs are also shown for reference with each figure.

In Figure 57 (992 Hz), it is immediately obvious that circulation control is not a significant noise source when the slot jet is not turbulent. Maps B through D indicate that noise is coming from the vicinity of the airfoil, but it is difficult to discern exactly where the noise is originating.

There is evidence of flow impingement noise on the tunnel diffuser or neighboring ceiling wedges in map D, which corresponds to $C_\mu = 0.017$. At the highest momentum coefficients tested, there is no evidence of flow impingement noise. In maps E through G, the trailing edge region is the definitive dominant noise source, although the power appears skewed to one side of the trailing edge. The power levels increase significantly with increasing C_μ beginning with $C_\mu = 0.017$.

Maps produced at 2 kHz are presented in Figure 58. In maps B through D, sidewall scrubbing noise, caused by the turbulent wall boundary layer, appears to be significant, and the levels for these maps are nearly identical, despite the fact that C_μ is increasing considerably. Flow impingement noise is also evident in maps D and E and is dominant in map D where $C_\mu = 0.017$. Beginning with map E ($C_\mu = 0.037$), the primary noise source is located in the vicinity of the trailing edge, but there are large deviations in sound power across the span of the model in maps E through G.

The beam maps at 4 kHz shown in Figure 59 have similar characteristics to the 2 kHz maps. Sidewall noise dominates in maps B through D and is also readily apparent in map E. Flow impingement noise is observed in maps D and E as well. In maps F and G, the strongest source appears along the trailing edge at 37% span, and its level increases with C_μ. Other, less dominant sources are visible at the junctions between the sidewalls and model trailing edge.

In Figure 60, which shows maps at 8 kHz, maps B through D again reveal sidewall noise, and the primary sources are located at the intersections of the sidewalls and the airfoil leading edge. This sound could be caused by horseshoe vortices formed when the tunnel wall boundary layer passes around the leading edge. Compared with the higher C_μ cases, their levels are relatively low. In maps E through G, the primary sources appear at the trailing edge-sidewall interfaces and once again along the trailing edge at 37% span.

Maps created by the inner array at 16 kHz are shown in Figure 61. Sources in maps B through D include the sidewalls, leading edge horseshoe vortices, and diffuser flow impingement. However, the levels of these sources are very low relative to the sources at momentum coefficients of $C_\mu = 0.037$ and higher. The trailing edge-sidewall interface still dominates in map E, but the sound appears to distribute more uniformly over the trailing edge as C_μ increases in maps F and G.

Beam maps for 32 kHz are presented in Figure 62. With no or minimal blowing (maps B and C), the leading edge horseshoe vortices and the boundary layer trip appear as sources, although their levels are extremely low. The dominant sources are the trailing edge-sidewall interfaces in map D through G, and the 37% span location in maps E through G.

Finally, at 64 kHz (Figure 63), maps A through D are extremely noisy, but spectra measured by the center microphone in Figure 56 indicate the levels at this frequency are at or near the noise floor. Among the sidelobes apparent in maps E through G, the dominant sources still appear to be located at the junctions of the sidewalls and the trailing edge and along the trailing edge at 37% span.

Figures 57 through 63 reveal an assortment of noise sources, most of which are undesired. It is clear that for $Rec = 6.5 \times 10^5$, contaminating noise sources dominate at all frequencies considered when $C_\mu < 0.017$. These sources include sidewall noise, flow impingement noise, and leading edge noise, possibly from horseshoe vortices. At $C_\mu = 0.037$, some of these sources

are still present with the addition of noise at the trailing edge that appears to originate at the trailing edge-sidewall junctions and at 37% span. These same trailing edge sources appear to dominate for the higher momentum coefficients considered. Near the sidewall, a few mechanisms could be generating sound. First, vortices similar to wing tip vortices have been observed in prior circulation control experiments with sidewalls, and these very vortices were the subject of a recent numerical investigation (Englar & Williams 1972; Nishino & Shariff 2010). Second, there is a discontinuity at the edge of the slot formed by the steel airfoil end plate just a few millimeters from the foam wall. This edge could radiate sound. While these are potential mechanisms for sound generated near the sidewall, the source appearing at 37% span is surprising, especially considering that, in the absence of a freestream, the source is uniformly distributed across the entire trailing edge. Perhaps the sound is only generated with a freestream because it is caused by the turbulent boundary layer passing over the model surface or lip edge. However, while there is a seam of two lip pieces near 37% span, inspection reveals no distinct discontinuity or non-uniformity compared to the other lip seams, and prior to the tunnel entry, this seam is sealed and checked for leaks.

To gather more insight regarding these trailing edge sources, beam maps from opposite side blowing measurements (OSB) are compared with SSB measurements in Figures 64 to 70 for the three highest momentum coefficients considered. The left column of beam maps (A, C, E) corresponds to SSB, and the right column of beam maps (B, D, F) corresponds to OSB. To reiterate, the array is located on the same side as the blowing slot for the SSB cases.

The same and opposite slot blowing beam maps at 992 Hz, shown in Figure 64, are nearly undistinguishable, but it is interesting that the levels are slightly higher for OSB. At 2 kHz (Figure 65), there are slight differences in the sources identified. With OSB, the array does not measure flow impingement noise when $C_\mu = 0.040$, likely because the flow impingement noise is below the array plane. At the higher momentum coefficients, the maps are fairly similar, but the levels are as much as 5 dB higher for OSB compared to SSB. At 4 kHz (Figure 66), there are substantial differences in the apparent noise sources. With OSB, the noise is much more evenly distributed than SSB, and the levels are between 3-4 dB higher for OSB. At 8 kHz (Figure 67), however, the trailing edge-sidewall interfaces begin to dominate, along with a region near 25% span. Levels are just slightly higher for the OSB cases. It is difficult to distinguish the SSB and OSB beam maps shown in Figure 68 for 16 kHz, and for all but the highest C_μ shown, the maximum levels for SSB are higher than OSB. At 32 kHz and 64 kHz, presented in Figures 69 and 70, respectively, the beam maps for OSB reveal just one source located at one of the sidewall-trailing edge junctions. The highest levels for OSB are again 3-4 dB higher than SSB for 32 kHz, but the maximum levels are higher for SSB at 64 kHz. It is interesting that sources are not observed along the trailing edge at 37% span and at the opposite sidewall for OSB.

The array measurements provide useful information about the true sound sources in this experiment. At low momentum coefficients, tunnel sidewall noise, flow impingement noise, leading edge horseshoe vortices, and sidewall-trailing edge junction noise dominate. At the highest momentum coefficients, sidewall scrubbing noise and flow impingement noise are insignificant, but the sound may largely be produced at the sidewall-trailing edge interfaces and along the trailing edge at 37% span by an unknown source. Undoubtedly, a single microphone is certainly

not measuring only two-dimensional circulation control noise sources. Furthermore, since the trailing edge alone is never the dominant source, the applicability of the coherent output power and three-microphone methods is also questionable.

5.3 Broadband Noise

The beamforming results show that multiple broadband acoustic sources exist over all frequencies regardless of the momentum coefficient tested. Since sound produced by the two-dimensional circulation control sources of interest never appears to dominate, the COP and three-microphone methods are likely not suitable for application towards this investigation. However, they will still be assessed and compared with a single microphone autospectrum.

5.3.1 Free-Standing Microphones

The different free-standing microphone processing techniques described in Section 3.4.1 are compared for $Re_c = 6.5 \times 10^5$, $h/c = 0.0019$, and $C_\mu \approx 0.10$, which represents the highest C_μ tested and, as indicated by the beam maps, yields insignificant sidewall scrubbing and flow impingement noise. Data are presented for SSB and OSB cases. The single microphone spectrum represents the autospectrum of the center G.R.A.S. microphone. The COP de-noised autospectrum estimate is computed using the center G.R.A.S. and the downstream B&K microphone, although the resultant spectrum is similar if the upstream microphone is used. Both the COP and three-microphone spectra represent estimates for the signal measured by the center G.R.A.S. microphone.

Figure 71 compares the three methods for SSB. The COP and three-microphone spectra are plotted as a filled region that includes their uncertainty bounds. The COP spectrum is lower in magnitude than the single and three-microphone spectra, particularly at higher frequencies. The COP method is known to under-predict levels if the signal-to-noise ratio of the additional microphone is not sufficiently high (Bahr *et al.* 2008). The three-microphone spectrum is in close agreement with the single microphone spectrum at higher frequencies.

Similar results are shown in Figure 72 for opposite side blowing. The COP spectrum levels are low in comparison with the other methods, and the three-microphone spectrum agrees well with the single microphone spectrum, even at higher frequencies.

The general agreement of the spectra in Figures 71 and 72 indicates that there is little uncorrelated noise in the measurements. Since beamforming results indicate the existence of multiple dominant sources, these methods are not appropriate for measuring the noise of interest produced by the circulation control trailing edge. The three-microphone and single-microphone spectra are in good agreement, suggesting that the three-microphone method provides a satisfactory representation of the overall acoustic field comprised of circulation control noise and installation effects. Using the phased array, it may be possible to extract a spectrum of this desired circulation control noise only.

5.3.2 Array

An alternative approach to the methods discussed in the previous section is to obtain a spectrum from the array via integration, as described in Section 3.4.2. This process is certainly not without its limitations, particularly at higher frequencies, since the integrated levels are highly-dependent on the accuracy of the array calibration, including the measured sensor locations, and the region of integration.

An integrated spectrum is compared to the free-standing center G.R.A.S. microphone autospectrum in Figure 73 for $Re_c = 6.5 \times 10^5$, $h/c = 0.0019$, and SSB $C_\mu \approx 0.065$. The outer array is used to compute the spectrum for frequencies below 10 kHz, while the inner array is used for frequencies 10 kHz and higher. The integration region is frequency dependent and aims to exclude noise from the sidewall-trailing edge interfaces. In particular, the integration region is defined by

$$-BW/2 \le x \le BW/2$$
$$-L/2 + BW/2 \le y \le L/2 - BW/2$$

where BW refers to the computed array 3 dB beamwidth, $L = 1.12$ m is the airfoil span, and the origin of the coordinate system is at the midspan point where $x/c = 1$. The shaded overlay in Figure 73 represents the estimated uncertainty in the spectral levels computed using 10,000 iterations of the Monte-Carlo simulation described by Yardibi *et al.* (2010*a*). Both spectra in Figure 73 are plotted using the dimensionless spectrum form suggested by Howe (2002),

$$\Phi = 10 \times \log_{10}\left(\frac{(U/a)\Phi_O(\vec{x}, \omega)}{(\rho_0 U^2)^2 (L_s a/|\vec{x}|^2) M \sin^2(\theta/2) \sin \psi}\right), \tag{62}$$

where U is the freestream velocity, Φ_O is the single-sided power-spectral density, ρ_0 is the freestream density, L_s is the source length, $|\vec{x}|$ is the distance from the trailing edge at midspan to the observer, M is the freestream mach number, θ is the angle between the chordwise direction and the observer, and ψ is the angle between the spanwise direction and the observer. For the single microphone spectrum, $L_s = L = 1.12$ m, but for the array spectrum, L_s is based on the spanwise length of the frequency-dependent integration region. As expected, the array spectrum and single microphone spectrum deviate significantly, particularly at higher frequencies where the dominant sources appear at the sidewall-trailing edge interfaces.

The integrated array spectrum is used in the following section for comparison with the acoustic model derived by Howe (2002).

5.4 Howe's Model of Circulation Control Acoustics

Howe (2002) theorized three significant broadband noise types: curvature noise, passive slot noise, and slot-jet interaction noise. Curvature noise is produced by boundary layer turbulence scattering off the rounded trailing edge. Passive slot noise is generated by freestream boundary layer turbulence scattering off the slot lip. Finally, slot-jet interaction noise is caused by the interaction of turbulence in the trailing jet with the slot lip and trailing edge surface near the slot. Howe derived mathematical models for these three noise sources that are functions of

30

local flow scales, including the displacement thickness, mean velocity, and friction velocity. In order to accurately compare Howe's model with the experimental results, these scales need to be determined. First, the primary assumptions behind Howe's model are introduced.

5.4.1 Assumptions

Howe's model follows three primary assumptions. First, the freestream Mach number, $M \ll 1$. For the cases considered, $M = 0.06$, so this assumption is satisfied. Second, the freestream Reynolds number must be large. Since $Re_c = 6.5 \times 10^5$, this assumption is also satisfied. Finally, Howe assumed compactness of the scattering edge thickness. For curvature noise, Howe considered the trailing edge radius as the length scale of interest, and hence, $R \ll \lambda$. For the circulation control airfoil of the present study, $R = \lambda$ when $f = 15$ kHz, so provided $f < 1$ kHz, the compactness assumption is met. Howe considered the lip thickness as the length scale of interest when determining compactness for passive slot noise and slot-jet interaction noise. The airfoil under investigation has a lip thickness of 0.28 mm. An acoustic wavelength of 0.28 mm corresponds to a frequency of over 1200 kHz, so this compactness assumption is also valid for the highest frequency of interest, 80 kHz.

5.4.2 Estimates of Flow Scales

Howe's model is assessed using flow measurements for $Re_c = 6.5 \times 10^5$, $C_\mu = 0.057$ ($Re_{jet} = 5000$), and $h/c = 0.0019$. This case represents the highest momentum coefficient studied with PIV. The flow scales (mean velocity, displacement thickness, and friction velocity) required to evaluate Howe's model are estimated from this data.

Curvature noise   Howe (2002) defines curvature noise as the sound produced by turbulence in the boundary layer passing over the rounded trailing edge. This is perhaps an unclear definition, since, as shown in Section 4, the flow over the rounded trailing edge is that of a wall jet and not a conventional boundary layer. In addition, exactly where to estimate the scales along the trailing edge is vague. In his analysis, Howe used the point of maximum curvature on an ellipse. Since the airfoil trailing edge under investigation has a constant radius, curvature is constant. Instead, since it is well-known that turbulent sound production increases with velocity, scales for curvature noise are evaluated at the point of maximum velocity along the trailing edge.

The mean tangential velocity profile at the position of maximum velocity, found to be $r\theta/c = 0.0129$, is plotted in Figure 74. The three scales of interest include the mean velocity outside the boundary layer, the displacement thickness, and the friction velocity. Since the flow represents a wall jet, the inner region provides the closest resemblance to a conventional boundary layer and will henceforth be used to determine these flow scales. The mean velocity outside the boundary layer is chosen to be the local maximum velocity, which is measured to be $U_o = U_{max} = 91.3$ m/s. The displacement thickness and friction velocity are much more difficult to calculate because of insufficient data near the surface. Furthermore, the maximum velocity is found to be the closest datum point to the surface. As an approximation, a one-seventh power law is

used to estimate the displacement thickness and momentum thickness (Prandtl 1961).

$$\frac{\bar{U}}{U_{max}} = \left(\frac{y}{y_{max}}\right)^{1/7} \tag{63}$$

The displacement thickness,

$$\delta_* = \int_0^{y_{max}} \left(1 - \frac{\bar{U}}{U_{max}}\right) dy, \tag{64}$$

and momentum thickness,

$$\theta = \int_0^{y_{max}} \frac{\bar{U}}{U_{max}} \left(1 - \frac{\bar{U}}{U_{max}}\right) dy, \tag{65}$$

are determined by evaluating the power law. The skin friction coefficient is then estimated using the Kármán integral relation (White 2006),

$$C_f \approx \frac{0.3e^{-1.33H}}{(\log_{10} Re_\theta)^{1.74+0.31H}}, \tag{66}$$

where $H = \delta_*/\theta$ is the shape factor, and $Re_\theta = U_{max}\theta/\nu$ is the Reynolds number based on the momentum thickness and "freestream" velocity. After the skin friction is obtained, the wall shear stress and friction velocity are estimated.

$$\tau_w = \frac{1}{2}\rho_0 U_{max}^2 C_f \tag{67}$$

$$v_* = \sqrt{\frac{\tau_w}{\rho_0}} \tag{68}$$

The displacement thickness and friction velocity are approximately 0.010 mm and 9.57 m/s, respectively.

Passive slot noise Howe (2002) considers passive slot noise to be the sound produced by turbulence in the exterior freestream boundary layer scattering off the slot lip. Like curvature noise, the assumption of a conventional boundary layer flow passing over the lip is not entirely true. Figure 22 shows that the flow passing over the lip edge takes the form of a wall jet more so than a boundary layer. Like curvature noise, the mean velocity outside the boundary layer is taken as the local maximum velocity, and the displacement thickness is computed using Equation 64.

The mean tangential velocity profile measured using PIV is shown in Figure 75. The maximum velocity is found to be $U_s = U_{max} = 41.4$ m/s. Because there is sufficient data in the profile, the displacement and momentum thicknesses are computed using the data alone. The friction velocity is estimated using the Kármán integral relation. The displacement thickness is 0.140 mm, and the friction velocity is 2.78 m/s.

Slot-jet interaction noise Slot-jet interaction noise is theorized by Howe (2002) to be generated by the interaction of turbulence in the jet with the slot lip and lower slot surface, i.e. the trailing edge in the vicinity of the slot. To estimate the flow scales for this noise source,

the mean tangential velocity profile just downstream of the slot exit plane is evaluated. The mean velocity is once again taken to be the local maximum wall jet velocity. Because the upper portion of the profile is influenced by the lip wake, the displacement and momentum thicknesses are analyzed at the lower Coanda surface using the one-seventh power law of Equation 63. The Kármán integral relation is again used to estimate the friction velocity.

The mean tangential velocity profile at the slot exit is shown in Figure 76. The maximum velocity is found to be $U_j = U_{max} = 88.8$ m/s, the displacement thickness is estimated as 0.025 mm, and the friction velocity is approximated to be 6.84 m/s.

5.4.3   Comparison with Measurement

Now that scales have been estimated from the PIV data, they will used to be compare Howe's model to a measured spectrum. For comparison purposes, first, Howe's model is assessed using the scales it estimates given just the model geometry, freestream velocity, and jet velocity. Specifically, the scales are the freestream velocity, U, the jet velocity U_{jet}, the semi-major axis of the airfoil elliptic profile, a, the trailing edge radius, r, the slot height, h, and the lip thickness, l.

$$U = 18.9 \text{ m/s}, \quad U_{jet} = 80.6 \text{ m/s}, \quad a = 0.2606 \text{ m}$$
$$r = 0.0222 \text{ m}, \quad h = 1 \times 10^{-3} \text{ m}, \quad l = 2.7 \times 10^{-4} \text{ m}$$

The spectrum produced by Howe's model for these inputs is shown in Figure 77 along with the spectrum obtained from the array measurement. The spectra are presented in the form given by Equation 62. For the present case, values for these constants are given below.

$$\rho_0 = 1.21 \text{ kg/m}^3, \quad |\vec{x}| = 1.12 \text{ m}, \quad M = U/c_0 = 0.055$$
$$\theta = \pi/2 \text{ rad}, \quad \psi = \pi/2 \text{ rad}$$

Recall, when applied to the array spectrum, L_s, the source length, is frequency-dependent and based on the array's 3 dB beamwidth. For the predicted spectrum in Figure 77, $L_s = 1.12$ m.

As evident in Figure 77, there are significant differences between the measured spectra and Howe's model. However, recall Howe's spectrum is computed using only estimates of the length and velocity scales. These scales are listed in Table 4 and compared with those determined from the PIV measurements. Not surprisingly, there are large differences between the scales, especially those for curvature noise. Recall, Howe (2002) considers curvature noise to be produced by boundary layer turbulence, whereas in the actual flow, there is a wall jet instead of a conventional boundary layer passing over the trailing edge. If the inner region of the wall jet is taken to be the boundary layer, then the mean and friction velocities will certainly be higher, and the displacement thickness will be significantly smaller.

When the scales estimated from the PIV measurements are substituted into Howe's model, the predicted spectrum is quite different, as shown in Figure 78. The differences between the measured and predicted spectra, though, are still significant. The shaded regions presented with each predicted spectrum represent uncertainty bounds, estimated using 10,000 iterations of a

Monte-Carlo simulation. The friction velocities, displacement thicknesses, mean velocities, slot height, lip thickness, and freestream velocity are all perturbed with each iteration. The perturbations to the friction velocities, displacement thicknesses, and mean velocities are themselves determined from 10,000 iterations of Monte-Carlo simulations based on the PIV measurement uncertainty. Even considering all uncertainties, the differences between the predicted and measured spectra are large. However, some useful information may still be extracted from Howe's model. According to the model, passive-slot noise is the dominant noise source for frequencies below 20 kHz, and slot-jet interaction noise is the primary source at higher frequencies.

Finally, an attempt is made to determine values for the flow scales in order for Howe's model spectrum to approach the measured array spectrum. Howe's model is fit to the measured spectrum using a least squares approach, and the flow scales that provide the best fit are determined. The results from the least squares fit are dependent on the initial guess and the bounds set for each parameter. The initial guesses for the parameters are the measured values of the scales listed in Table 4. The lower bounds for all parameters are set to 0. The upper bounds for the mean velocities are set to 100 m/s, the upper bounds for the friction velocities are set to 20 m/s, and the displacement thickness bounds for the wall jet and lip boundary layer profiles are set to 0.5 mm and 1 mm, respectively. The best fit spectrum is compared to the measured spectrum in Figure 79, where the two are shown to be in close agreement. Notice there is no contribution from slot-jet interaction noise. To reiterate, the resultant best fit parameters are dependent on the initial guesses and bounds, so this solution is provided simply for illustrative purposes. The scales determined from the best fit are listed in Table 5. There are generally large variations between the scales obtained from the PIV measurements and the scales listed in Table 5. In addition, some of the scales are unreasonable, including $v_* = 19$ m/s for the flow passing over the lip, $\delta_* = 0.5$ mm with a corresponding $v_* = 20$ m/s for the wall jet flow responsible for curvature noise, and $\delta_* = 1.0 \times 10^{-5}$ mm for the displacement thickness at the slot exit.

5.5 Summary

The sound produced by a circulation control airfoil in an open jet anechoic wind tunnel is measured and characterized using free-standing microphones and a nested phased acoustic array. Tones produced by vortex shedding from the round trailing edge and blunt slot lip are detected. Beamforming maps indicate that the trailing edge is the dominant source in the absence of a freestream, but with a freestream, there are a multitude of sources. At low momentum coefficients corresponding to laminar slot jets, contaminating noise sources, including flow impingement noise and sidewall scrubbing noise, are observed to dominate. At higher momentum coefficients, noise from the trailing edge is the primary source, but the sound power is unevenly distributed along the trailing edge. The beam maps indicate that the interfaces of the sidewalls and trailing edge are the primary sources, particularly at higher frequencies. Spectra computed using the COP and three-microphone methods are compared with single microphone autospectrum and found to be in close agreement, indicating little uncorrelated noise in the measurements. All three methods are, by their nature, unable to distinguish the two-dimensional circulation control noise generated at the trailing edge with noise produced by

the aforementioned contaminating noise sources. A spectrum is also computed using the phased array by integrating over a small, frequency-dependent region of the trailing edge to minimize the sidewall end effects. This integrated spectrum is compared with a model of circulation control acoustics presented by Howe (2002) and found to differ on average by 30 dB. Howe's model suggests that, for the test conditions considered, passive slot noise is the dominant noise source for frequencies below 20 kHz, and slot-jet interaction noise is the principal source at higher frequencies.

6 Conclusions and Future Work

6.1 Key Findings

6.1.1 Fluid Dynamics

Midspan surface pressure measurements of an elliptic circulation control airfoil in the UFAFF reveal the absence of a leading edge suction peak regularly observed in circulation control experiments and numerical studies. The lack of a leading edge suction peak contributes to a deficit in the lift produced compared with prior experiments of the same geometry in closed test section wind tunnels. The leading edge suction peak is recovered by enclosing the wind tunnel test section, and the lift deficit is eliminated. However, the surface pressure distribution is highly-dependent on the boundary conditions enforced by the suction-side tunnel boundary. Measured surface pressure distributions are compared with potential flow theory for flow around an ellipse using the conformal mapping technique. The theory provides insight into the behavior of the flow and explains the elevated suction-side and reduced pressure-side surface pressure magnitudes measured with a rigid versus porous suction-side tunnel boundary. In addition, the theory also supports the observations that the pressure-side tunnel boundary is nearly irrelevant in determining the surface pressure distribution.

PIV measurements reveal the extent to which enclosing the test section significantly modifies the leading edge flow field. In an open jet test section, leading edge stagnation point movement is minimal with increasing momentum coefficient. In a closed test section, leading edge stagnation point movement is considerably more significant as the momentum coefficient increases. Contrary to the leading edge observations, PIV measurements reveal negligible differences in the boundary layer flow passing over the slot lip when the test section is opened or closed. The scattering of turbulent pressure fluctuations in this boundary layer off the slot lip is one of the noise sources theorized by Howe (2002). Hence, this noise source mechanism should remain largely unchanged regardless of whether the test section is enclosed or not. This finding can provide direction to future researchers considering circulation control experiments in open or closed wind tunnels when acoustic measurements may be of interest.

Additional PIV measurements focus on the curved wall jet flow and its similarity. Although a similarity solution indicates that full flow similarity is only achievable if the curved surface takes the shape of a logarithmic spiral, the outer regions of the mean tangential velocity profiles do indeed exhibit similarity using scales based on the maximum velocity and the Reynolds stress or mean shear (Launder & Rodi 1983). The length and velocity scales required for similarity are

measured for a collection of test cases where the chord Reynolds number, momentum coefficient, and slot height are varied. The data for these scales is assembled and found to collapse, and the resultant best-fit equations of the scales are a function of the product of the chord Reynolds number and momentum coefficient. This so-called Reynolds corrected momentum coefficient can also be recast as a product of the jet Reynolds number and jet-to-freestream velocity ratio (see Equation 54) indicating that, unlike the case of the planar wall jet in a freestream, the length and velocity scales describing the curved wall jet flow in a freestream are dependent on the jet Reynolds number (Zhou & Wygnanski 1993). The equations for predicting these length and velocity scales, given by Equations 50 through 53, compare favorably with measurements.

Flow separation is also assessed using PIV, and, like the length and velocity scales of the flow, the separation location is a function of the Reynolds corrected momentum coefficient. An equation for predicting the separation location is provided and found to match the present measurements with excellent accuracy. However, the equation may only be valid for the airfoil geometry investigated, as using it to predict the separation location for a different geometry studied by Novak & Cornelius (1986) and Novak *et al.* (1987) leads to large errors. Regarding the separation mechanism, crossflow PIV measurements uncovered streamwise pairs of counter-rotating vortices only previously measured in a curved wall jet in the absence of a freestream (Likhachev *et al.* 2001; Neuendorf *et al.* 2004; Han *et al.* 2006). These vortices, which "pull" high-momentum fluid away from the surface, are thought to be ultimately responsible for flow separation (Neuendorf *et al.* 2004; Han *et al.* 2006). If that is the case, then these vortices may preclude the use of serrated lip treatments to reduce lip vortex shedding tones, since the serrations may stimulate and advance the earlier development of these vortices in the flow.

6.1.2 Acoustics

Acoustic measurements reveal the presence of low and high frequency tones associated with vortex shedding from the round trailing edge and blunt slot lip, respectively. The low frequency tone can be eliminated with single slot blowing provided the momentum coefficient is at least 0.002. The emergence and behavior of the high frequency tones is somewhat sporadic, as no clear trends based on flow parameters like the chord Reynolds number, momentum coefficient, jet Reynolds number, and slot height-to-chord ratio are found. However, the lip tones are only, but not necessarily, produced when both the chord and jet Reynolds numbers are nonzero. Also, the tones are hardly discernible from the broadband noise when measured on the opposite side from the blowing slot, indicating that these high frequency tones are highly directive.

Broadband noise sources are identified using a nested phased microphone array. Without a freestream, the trailing edge is the dominant sound source provided the jet Reynolds number is sufficiently high to create a turbulent jet. With a freestream, however, many sources are measured. At the chord Reynolds number tested, $Re_c = 6.5 \times 10^5$, contaminating noise from sidewall scrubbing and flow impingement are found to dominate at low momentum coefficients or jet Reynolds numbers. In addition, leading edge horseshoe vortices formed at the sidewall-model junctions dominate at frequencies below 8 kHz for $C_\mu < 0.017$, although their levels are low relative to the other sources identified. At higher momentum coefficients, the trailing edge is the dominant source. However, the sound is not evenly-distributed along the trailing edge. Instead,

sources are measured at the trailing edge-sidewall junctions, likely caused by the interaction of induced streamwise vortices with the sidewalls, and near 37% span, the origin of which is unknown but may be due to the seam between two airfoil components. Array measurements of tests utilizing the opposite blowing slot from the array indicate that at frequencies of 8 kHz and higher, the trailing edge-sidewall junctions are the primary sources.

The presence of multiple sources makes the estimation of broadband noise produced by the circulation control airfoil extremely difficult. Spectra computed using different microphone processing techniques, including single microphone autospectrum, coherent output power, and the three-microphone method, are found to be in close agreement. However, since the array detects multiple sources over all frequencies of interest, the results from the microphone processing techniques are all invalid since the single-source assumption is violated. Thus, these methods are not suitable for measurements of "two-dimensional" circulation control noise, including the sources theorized by Howe (2002). Array integration techniques provide the only means to estimate the sound not attributed to the undesired noise sources, but more work is needed to perfect calibration techniques, and assess and reduce microphone scattering effects.

Finally, Howe's model of circulation control acoustics is evaluated at $Re_c = 6.5 \times 10^5$, $C_\mu = 0.057$, and $h/c = 0.0019$ where circulation control related noise is dominant (Howe 2002). The mean velocity, friction velocity, and displacement thickness scales required by Howe's model are estimated from the PIV measurements of the trailing edge flow field. Using these scales, large differences ($\sim$ 30 dB) are observed between Howe's model and a broadband spectrum obtained from array measurements. Howe's model indicates that, at the test conditions evaluated, which correspond to a low chord Reynolds number and a moderate momentum coefficient, the dominant noise mechanism for frequencies below 20 kHz is the turbulent freestream boundary layer flow passing over the slot lip. The interaction of turbulence in the slot jet with the slot lip is the dominant source at higher frequencies. Noise produced by the turbulent flow passing over the round trailing edge is negligible.

6.2 Research Impact

The initial goals of this research investigation placed an emphasis on identifying and characterizing the two-dimensional noise source mechanisms of a circulation control airfoil. However, the rather unexpected results of this study indicate that three-dimensional noise sources may be of more interest and, from an acoustics perspective, a primary deterrent to the application of circulation control to underwater vehicles. The noise sources identified at the junctions between the trailing edge and sidewalls are significant at frequencies of at least 4 kHz and higher. These noise sources, not the original two-dimensional noise sources considered, warrant further investigation.

The findings of this investigation also highlight a recurring theme in experimental aeroacoustics - quantifying the source of interest is often extremely difficult. The noise produced by the baseline or low slot blowing flows is heavily contaminated by sidewall scrubbing and flow impingement noise. These undesired sources must be eliminated if the noise produced by circulation control is to be assessed at such test conditions. Of course, that is not a straightforward task, and options are limited based on the flow facility and the model being tested.

For example, if sidewalls are eliminated, other undesired sources or three-dimensional effects would be introduced. Perhaps a sidewall suction system, if implemented in a quiet fashion, could eliminate the three-dimensional effects without introducing additional noise. As for measurement techniques, the multiple sources identified by the phased acoustic array prohibit the use of multiple microphone-based methods if the two-dimensional sound sources are of primary interest. However, these methods might be suitable in the study of the three-dimensional noise sources. Otherwise, array-based methods provide the only possible manner by which to study the two-dimensional sources of interest.

6.3 Recommendations for Future Work

Since this investigation has identified substantial three-dimensional noise source mechanisms, future wind tunnel measurements should focus on three-dimensional models similar to an underwater vehicle control surface. A scaled semi-span circulation control wing should be mounted to a section of a model vehicle hull and tested in an anechoic wind tunnel. Furthermore, by removing the porous tunnel walls, sidewall scrubbing noise will be eliminated. Instead, the relative strength of the sound produced by the hull-trailing edge noise source can be evaluated, and other three-dimensional effects representative of an actual underwater vehicle can be gauged. In addition, future models should be constructed in as few components as possible, eliminating the likelihood that model seams or joints can influence the measurements.

Additional work is needed to fully characterize the emergence and behavior of the high-frequency lip tones. These tones could be a significant impediment to the application of circulation control to underwater vehicles. Since the tones have been experimentally verified, lip modifications aimed at reducing their levels, like those suggested by Slomski (2009), should be experimentally evaluated. Furthermore, the effect of such modifications on flow separation must be adequately assessed.

The present investigation utilizes PIV to measure the length and velocity scales required for Howe's model, but PIV is unable to measure extremely close to surfaces, which is essential for highly-accurate displacement thickness and friction velocity estimates of the curved wall jet (Howe 2002). Additional measurements are recommended on larger-scale models in larger test facilities, so that spatial resolution is subsequently improved. Hot-wire anemometry should also be considered in place of PIV for measuring near-wall velocity profiles, provided the flow is nominally unidirectional. Microelectromechanical systems (MEMS) shear stress sensors, like the one developed by Chandrasekharan (2009), should be considered for installation along the Coanda surface. Although packaging such devices may be difficult on a highly-contoured surface, they could provide a precise measurement of the friction velocity. Alternatively, global interferometric skin-friction measurements of the Coanda surface and lip could also provide accurate friction velocity information (Naughton & Sheplak 2002). Highly-accurate flow measurements at a variety of test conditions are essential to confirm under what conditions passive slot noise is indeed the primary two-dimensional noise source.

Finally, further work is needed to support the use of array-based methods in aeroacoustic measurements. These methods are particularly challenging when, like in the present investigation, high frequency sources must be considered. Higher frequencies motivate the need for

smaller aperture arrays, but smaller aperture arrays introduce significant microphone scattering effects. Either the scattering effects need to be characterized, or a suitable treatment needs to be found to mitigate scattering. The latter may not be too effective in some circumstances, like the present investigation, where the distance separating microphones is less than a half-wavelength at the highest frequency of interest. Instead, an array of MEMS microphones should be considered for future experiments. Such an array would permit closer sensor spacing and provide reduced scattering effects, both from neighboring sensors and the microphones themselves (Underbrink 2002; Arnold *et al.* 2003).

7 Acknowledgments

Appendix

The authors of this report have also presented this work at numerous conferences and are currently finalizing manuscripts for publication. These papers are listed below.

1. Wetzel, D., Liu, F., Rosenberg, B., and Cattafesta, L., "Acoustic Characteristics of a Circulation Control Airfoil," AIAA-2009-3103, *15th AIAA/CEAS Aeroacoustics Conference*, Miami, FL, May 2009.

2. Wetzel, D., Griffin, J., Liu, F., and Cattafesta, L., "An Experimental Study of Circulation Control on an Elliptic Airfoil," AIAA-2009-4280, *39th AIAA Fluid Dynamics Conference*, San Antonio, TX, June 2009.

3. Wetzel, D., Griffin, J., Liu, F., and Cattafesta, L., "An Experimental Study of a Circulation Control Airfoil Trailing Edge Flow Field," AIAA-2010-4576, *5th AIAA Flow Control Conference*, Chicago, IL, July 2010.

4. Wetzel, D., Griffin, J., and Cattafesta, L., "Experiments on an elliptic circulation control airfoil," *J. Fluid Mech.*, *In progress.*

5. Wetzel, D., Liu, F., Bahr, C., and Cattafesta, L., "Experiments on circulation control acoustics," *J. Sound Vib.*, *In progress.*

The primary author of this report, Drew Wetzel, received his Ph.D. in Mechanical Engineering in May 2011 after completing a dissertation based on the research presented in this report.

(a)

(b)
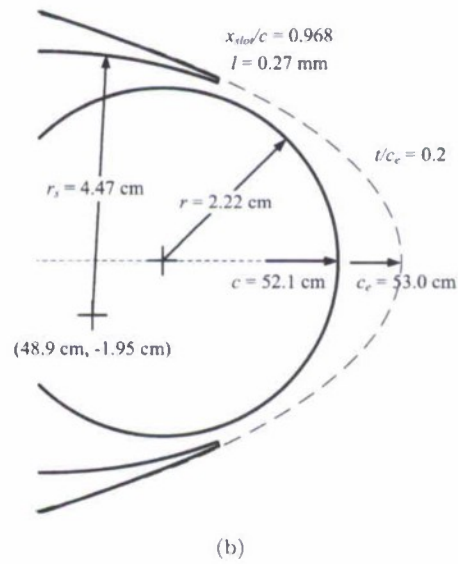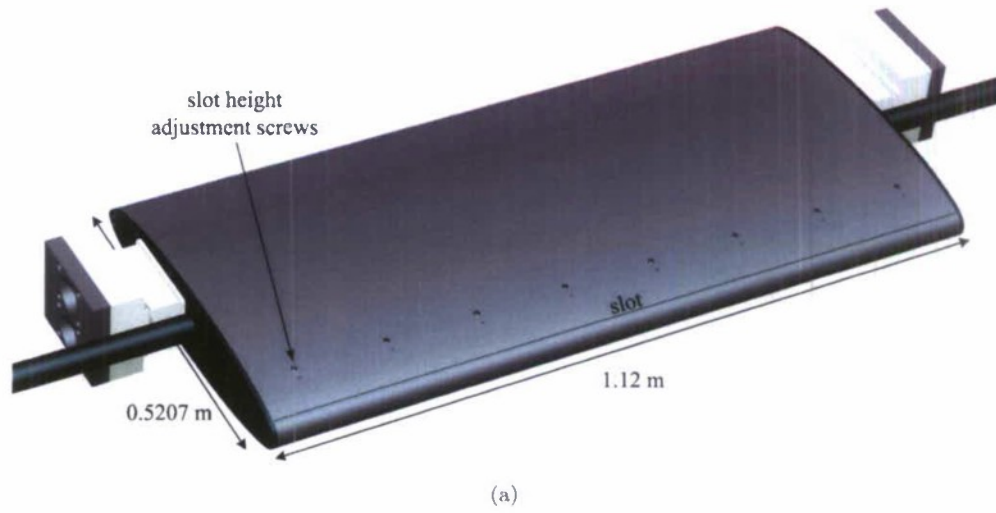
Figure 1: Circulation control airfoil geometry. a) Overall dimensions. b) Trailing edge geometry (l is the lip thickness, and t is the ellipse thickness).
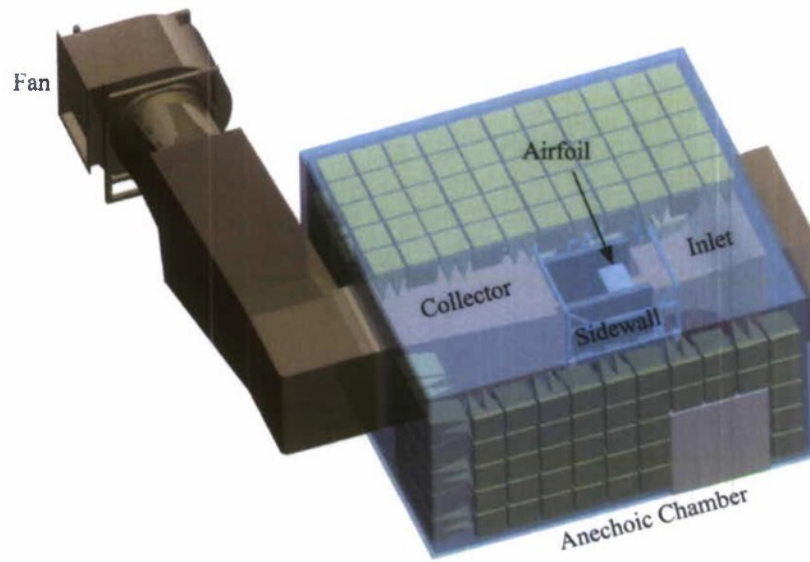
(a)
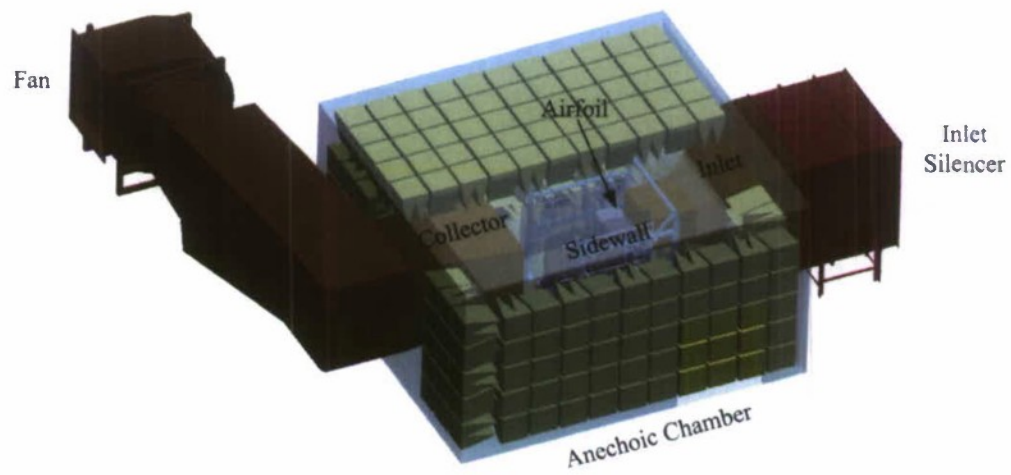
(b)

Figure 2: Circulation control airfoil installed in the UFAFF. a) 2009. b) 2010.

Figure 3: PIV trailing edge measurement regions: (a) trailing edge wake, (b) flow over lip, (c) curved wall jet, and (d) curved wall jet separation. Airfoil geometry sketched for reference.

Figure 4: Microphone experimental setup.
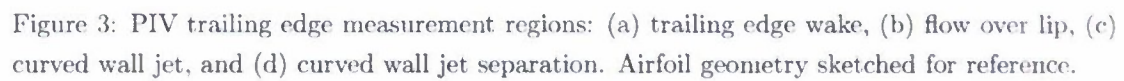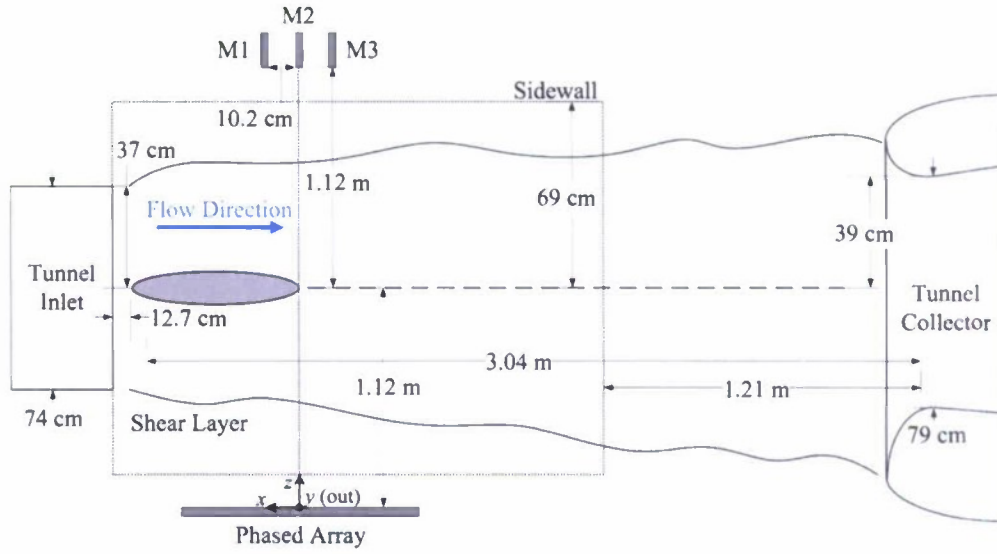
Figure 5: Phased array experimental setup.
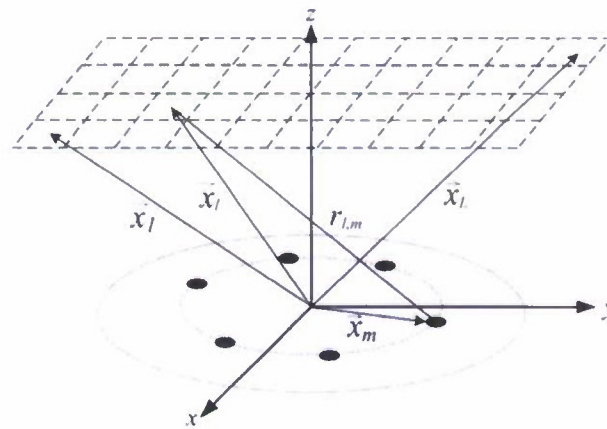
Figure 6: Scanning region of $l = 1, ..., L$ points.
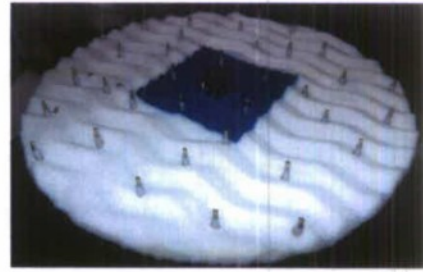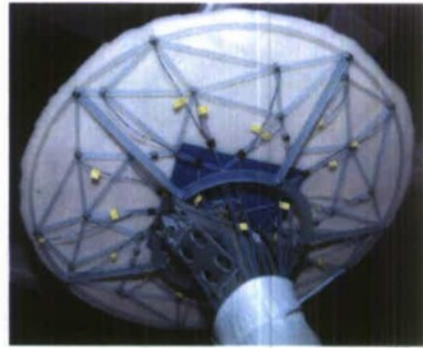
Figure 7: Pictures of the phased array. a) Installed in the UFAFF, looking towards the inlet. b) Magnified view of the array. c) Acoustic treatment removed to reveal the array frame.
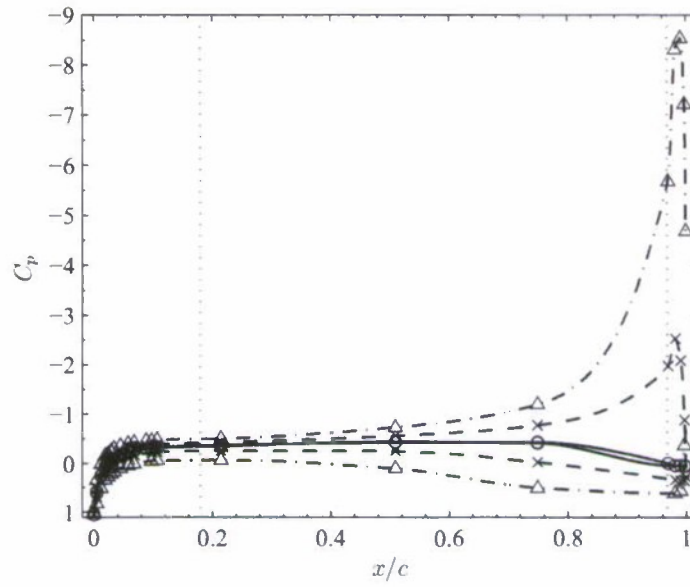
Figure 8: Airfoil surface pressure (C_p), $Re_c = 6.5 \times 10^5$, $h/c = 0.0019$. —o— $C_\mu = 0$ ($c_l = 0.020$), - -×- - $C_\mu = 0.015$ ($c_l = 0.58$), ---△--- $C_\mu = 0.057$ ($c_l = 1.5$). The left vertical dashed line represents the boundary layer trip, and the right vertical dashed line corresponds to the slot.
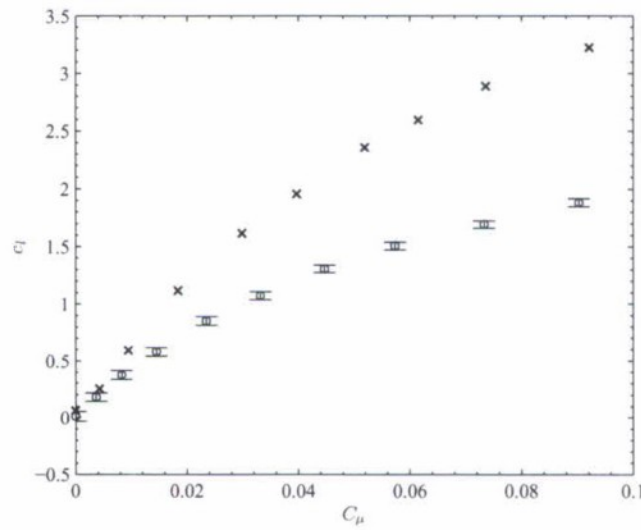
Figure 9: Lift coefficient (c_l) as a function of momentum coefficient, $Re_c = 6.5 \times 10^5$, $h/c = 0.0019$. o present investigation, × Abramson (1975) 20% elliptic circulation control airfoil, $Re_c = 3.4 \times 10^5$, $h/c = 0.0013$.
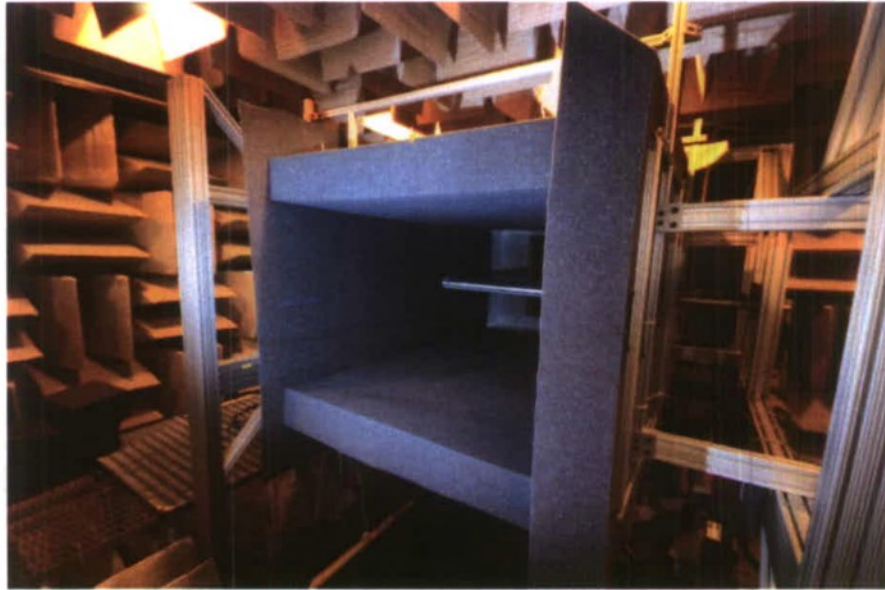
Figure 10: Photograph of closed test section.
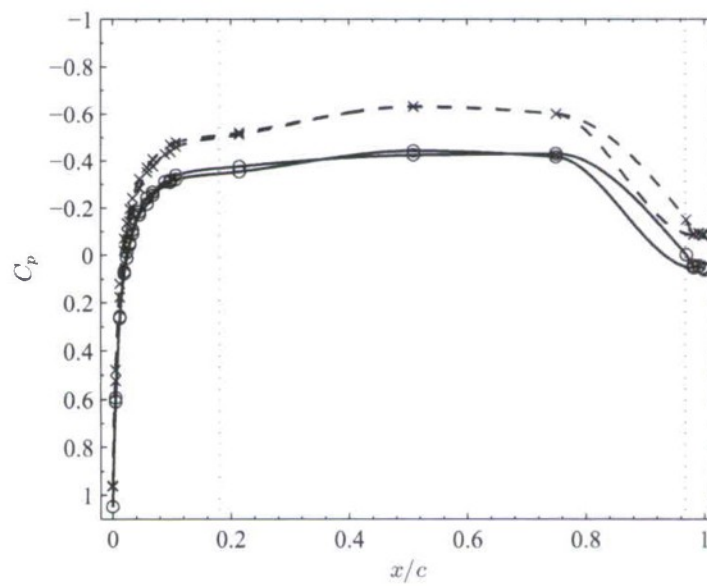
Figure 11: Airfoil surface pressure (C_p), $C_\mu = 0$, $h/e = 0.0019$. —○— open test section, $Re_c = 6.5 \times 10^5$; - -×- - closed test section, $Re_{c,c} = 6.7 \times 10^5$. The left vertical dashed line represents the boundary layer trip, and the right vertical dashed line corresponds to the slot.
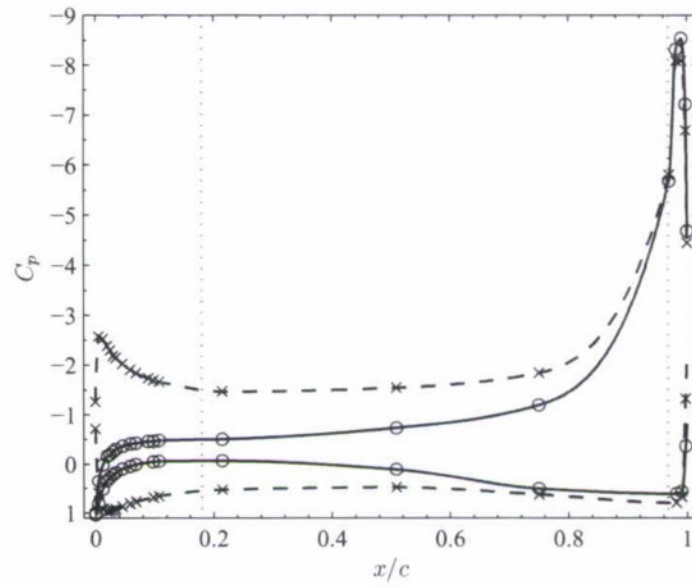
Figure 12: Airfoil surface pressure (C_p), $h/c = 0.0019$. —○— open test section, $C_\mu = 0.057$, $Re_c = 6.5 \times 10^5$ ($c_l = 1.5$); - -×- - closed test section, $C_{\mu,c} = 0.057$, $Re_{c,c} = 6.7 \times 10^5$ ($c_l = 2.7$). The left vertical dashed line represents the boundary layer trip, and the right vertical dashed line corresponds to the slot.
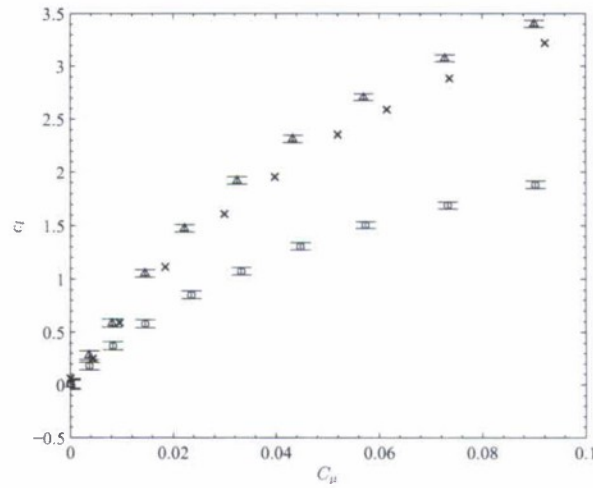
Figure 13: Lift coefficient (c_l) as a function of momentum coefficient, $Re_c = 6.5 \times 10^5$, $h/c = 0.0019$. ○ present investigation, open test section; △ present investigation, closed test section; × Abramson (1975) 20% elliptic circulation control airfoil, $Re_c = 3.4 \times 10^5$, $h/c = 0.0013$.

47

Figure 14: Photograph of closed test section for PIV measurements. The foam ceiling and one foam wall are replaced with clear polycarbonate panels.
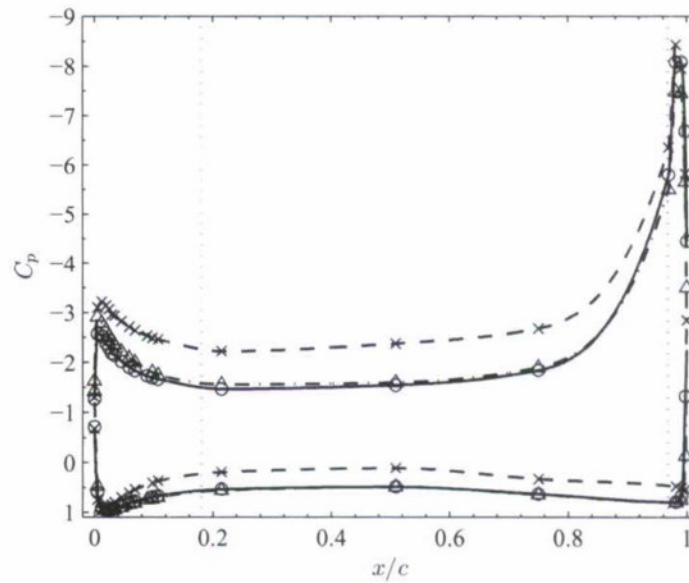
Figure 15: Airfoil surface pressure (C_p) in closed test section, $Re_c = 6.7 \times 10^5$, $h/c = 0.0019$. —○— foam walls, upper slot blowing, $C_\mu = 0.057$ $(C_l = 2.7)$; - -×- - foam/polycarbonate walls, upper slot blowing, $C_\mu = 0.052$ $(C_l = 3.1)$; ---△--- foam/polycarbonate walls, lower slot blowing, $C_\mu = 0.053$ $(C_l = 2.8)$. The left vertical dashed line represents the boundary layer trip, and the right vertical dashed line corresponds to the slot.
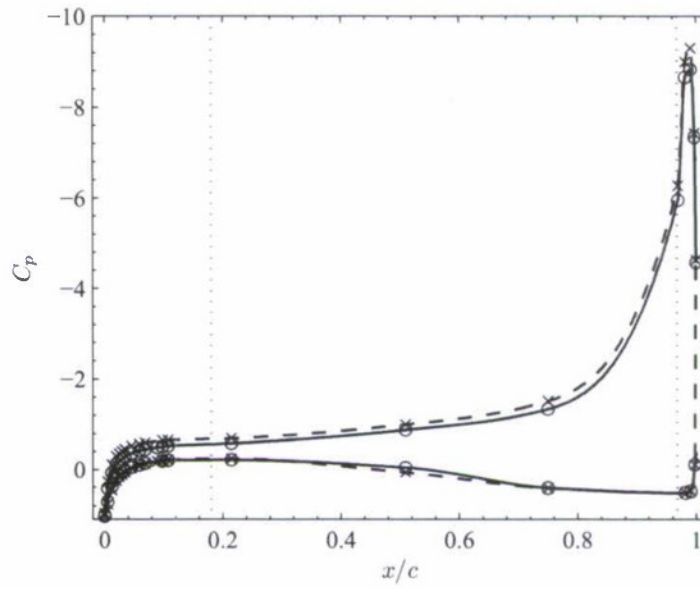
Figure 16: Airfoil surface pressure (C_p) in open test section, $Re_c = 6.5 \times 10^5$, $h/c = 0.0019$. —o— upper slot blowing, $C_\mu = 0.058$ ($c_l = 1.5$); - -×- - lower slot blowing, $C_\mu = 0.059$ ($c_l = 1.7$). The left vertical dashed line represents the boundary layer trip, and the right vertical dashed line corresponds to the slot.
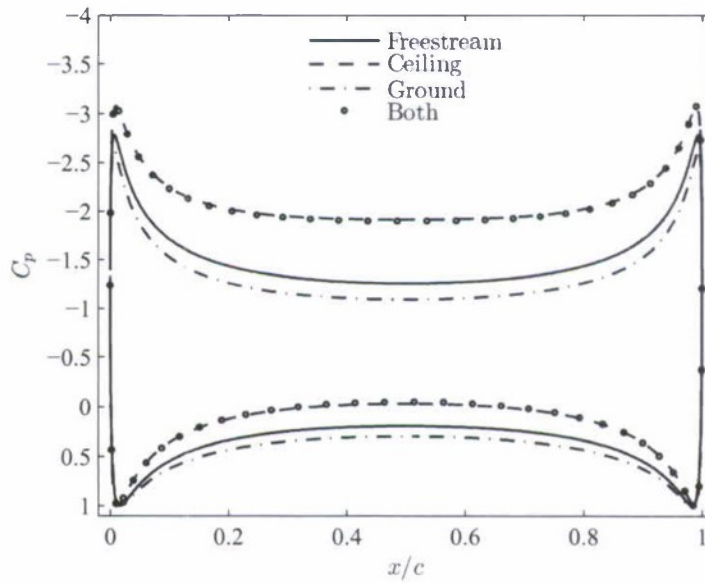
Figure 17: Potential flow C_p on a 20% ellipse, $U_\infty = 20$ m/s. —— freestream ($c_l = 1.90$); - - - - ceiling plane ($c_l = 2.29$); -·-·- ground plane ($c_l = 1.81$); ∘ ∘ ∘ ceiling and ground planes ($c_l = 2.26$).
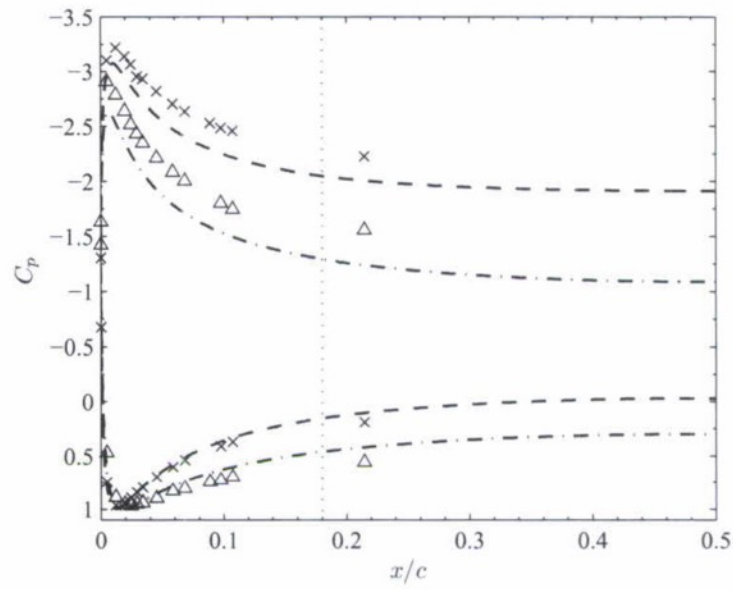
Figure 18: Airfoil surface pressure (C_p) in closed test section compared with potential flow theory. × foam/polycarbonate walls, upper slot blowing ($Cc_l = 3.1$); △ foam/polycarbonate walls, lower slot blowing ($c_l = 2.8$); - - - - potential flow, ceiling plane ($c_l = 2.29$); -·-·- potential flow, ground plane ($c_l = 1.81$).
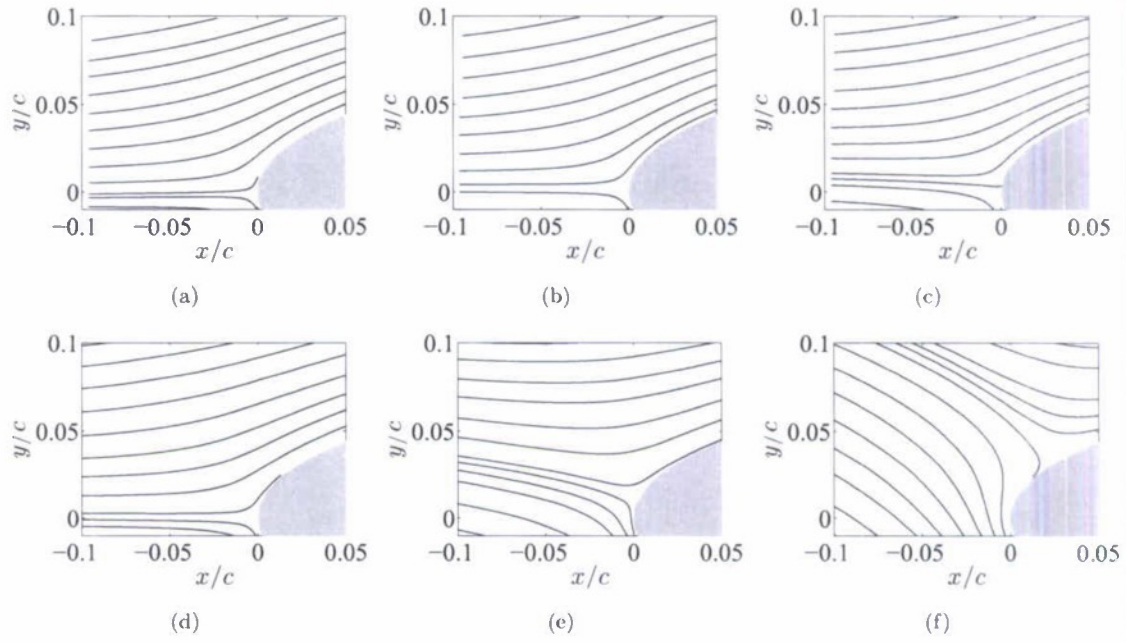
Figure 19: Leading edge mean flow streamlines in (a)-(c) open test section, $Re_c = 6.5 \times 10^5$ and (d)-(f) closed test section, $Re_{c,c} = 6.7 \times 10^5$. Flow is from left to right, and the origin is located at the leading edge. Lower slot blowing is used for all cases, $h/c = 0.0019$. a) $C_\mu = 0$. b) $C_\mu = 0.014$. c) $C_\mu = 0.057$. d) $C_{\mu,c} = 0$. e) $C_{\mu,c} = 0.013$. f) $C_{\mu,c} = 0.053$.
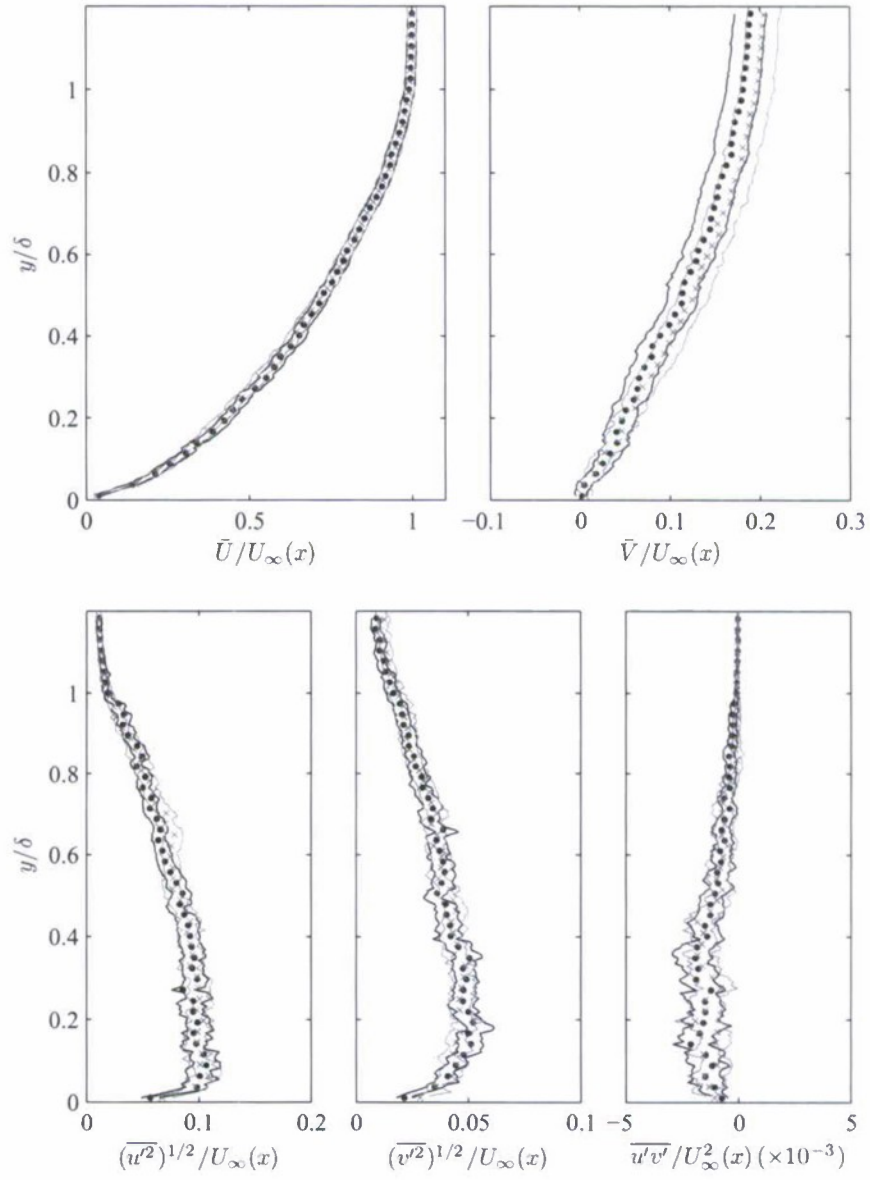
Figure 20: Comparison of profiles at the lip edge, $C_\mu = 0$. • open test section, $Re_c = 6.5 \times 10^5$; × closed test section, $Re_{c,c} = 6.7 \times 10^6$. The slot height is $h/c = 0.0019$ for both cases. For clarity, only every fourth datum point is displayed. Error bounds are represented by lines of matching color for each data set.
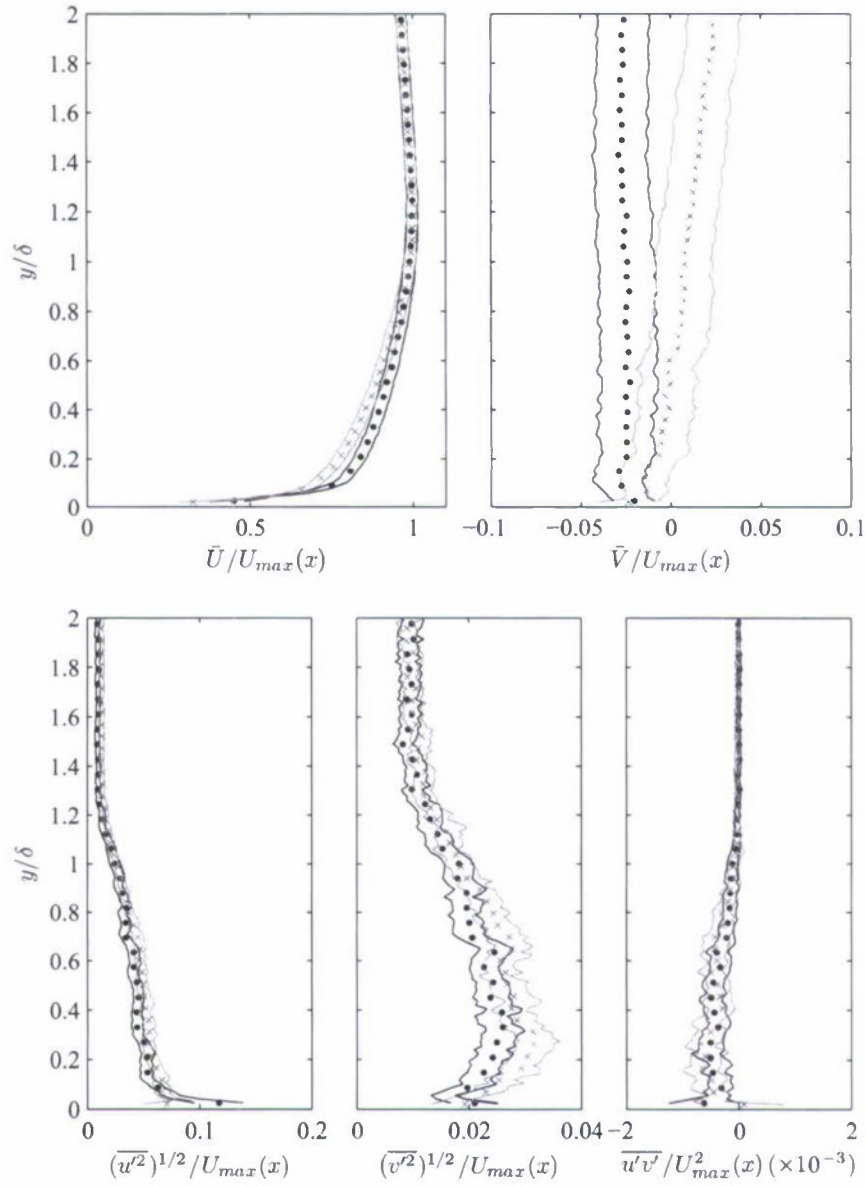
Figure 21: Comparison of profiles at the lip edge. • open test section, $Re_c = 6.5 \times 10^5$, $C_\mu = 0.014$; × closed test section, $Re_{c,c} = 6.7 \times 10^6$, $C_\mu = 0.013$. The slot height is $h/c = 0.0019$ for both cases. For clarity, only every fourth datum point is displayed. Error bounds are represented by lines of matching color for each data set.
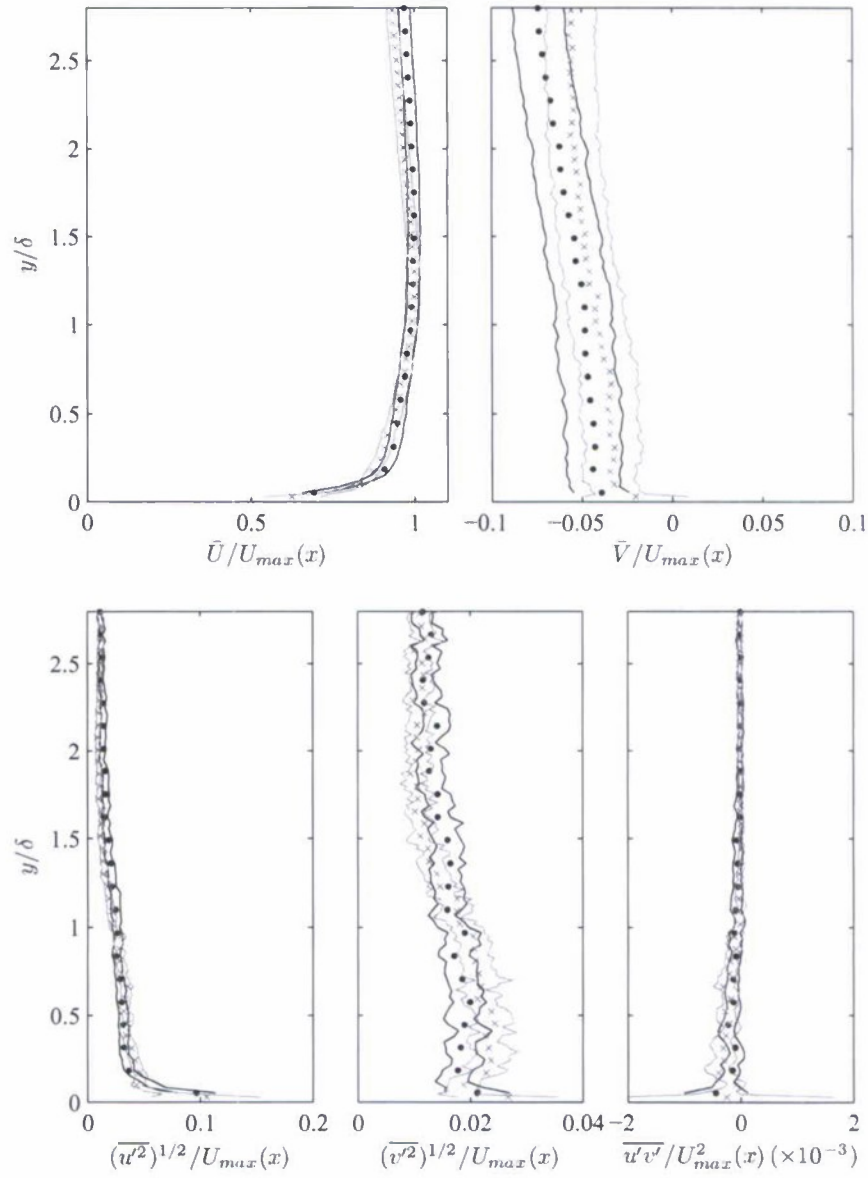
Figure 22: Comparison of profiles at the lip edge. •open test section $Re_c = 6.5 \times 10^5$, $C_\mu = 0.057$; × closed test section, $Re_{c,c} = 6.7 \times 10^6$, $C_\mu = 0.053$. The slot height is $h/c = 0.0019$ for both cases. For clarity, only every fourth datum point is displayed. Error bounds are represented by lines of matching color for each data set.
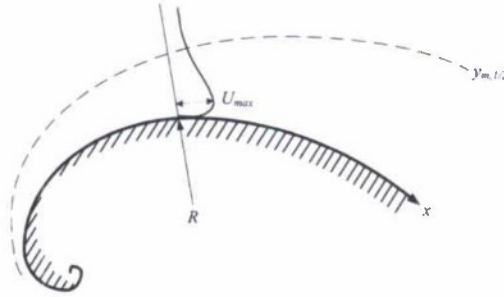
Figure 23: Logarithmic spiral surface.
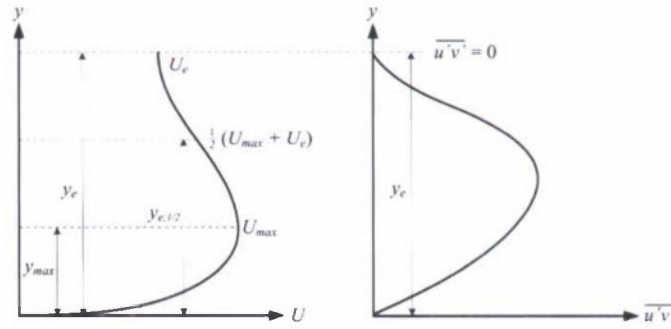
Figure 24: Length and velocity scales suggested by Launder & Rodi (1983).
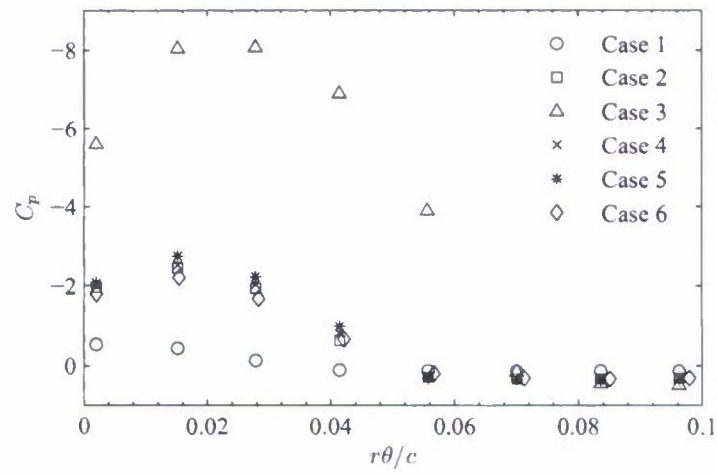
Figure 25: Coanda surface C_p. Please refer to Table 3 for test conditions for each case.
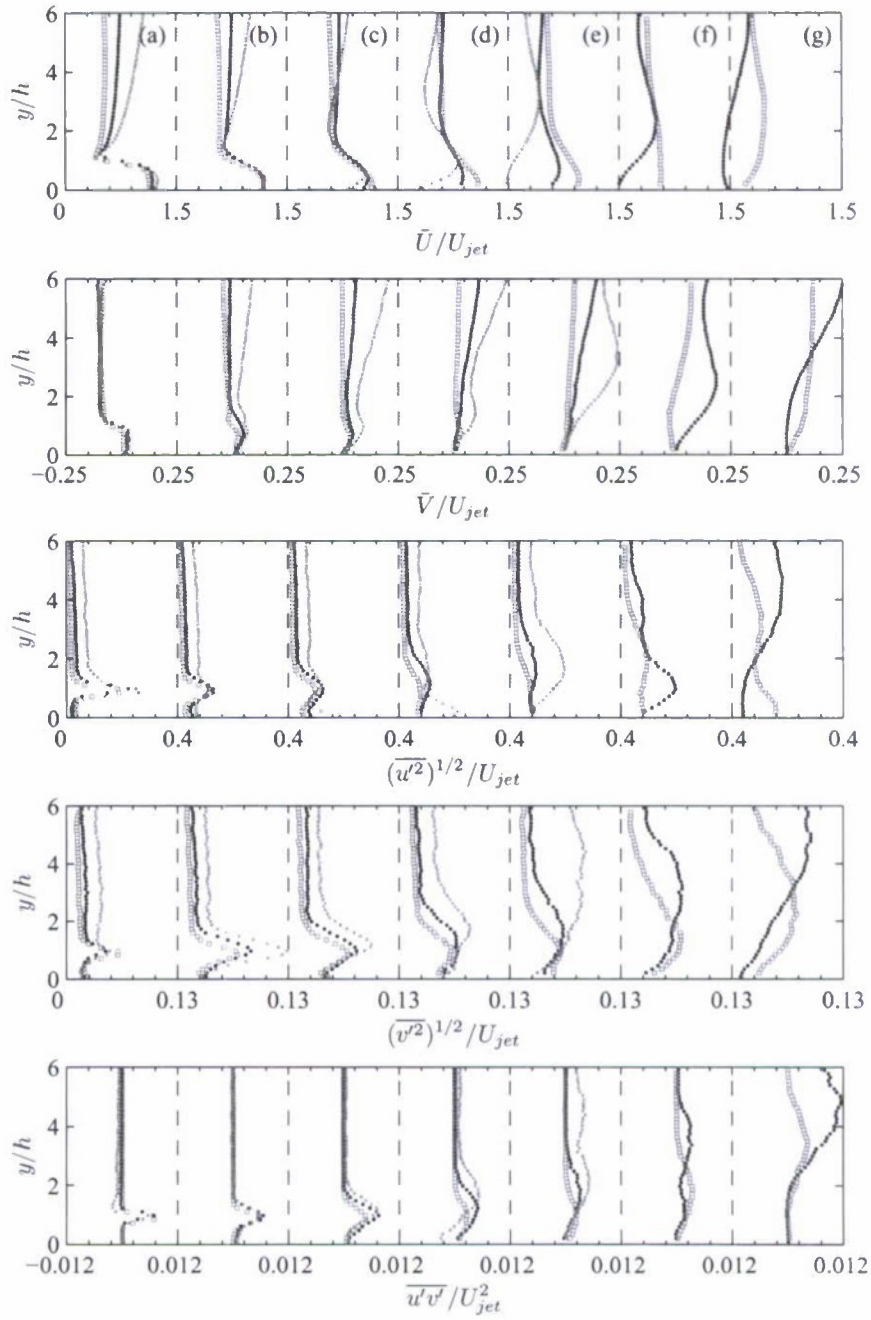
Figure 26: Circulation control curved wall jet profiles, $Re_c = 6.5 \times 10^5$, $h/c = 0.0019$. $r\theta/c =$ (a) 0.0036, (b) 0.011, (c) 0.018, (d) 0.026, (e) 0.033 (f) 0.040, and (g) 0.048. $\bullet$ $C_\mu = 0.015$, $C_\mu = 0.0039$, $C_\mu = 0.057$.
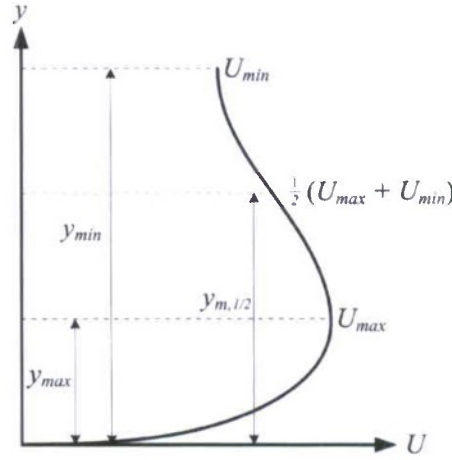
Figure 27: Length and velocity scales based on zero shear.
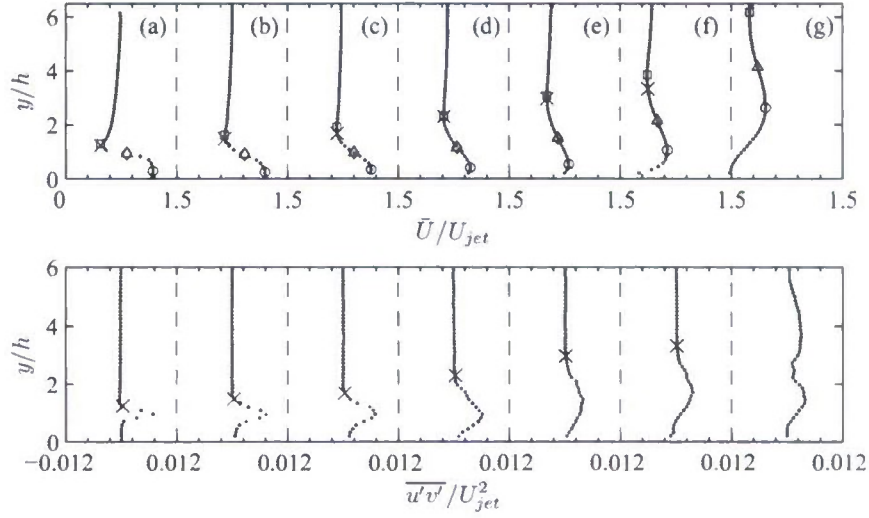
Figure 28: Circulation control curved wall jet profiles, $Re_c = 6.5 \times 10^5$, $C_\mu = 0.015$, $h/c = 0.0019$. $r\theta/c =$ (a) 0.0027, (b) 0.010, (c) 0.017, (d) 0.025, (e) 0.032 (f) 0.040, and (g) 0.047. Length scales are indicated by $\circ$ y_{max}, y_{min}, $\times$ y_e, $\triangle$ $y_{m,1/2}$, and $\diamond$ $y_{e,1/2}$.
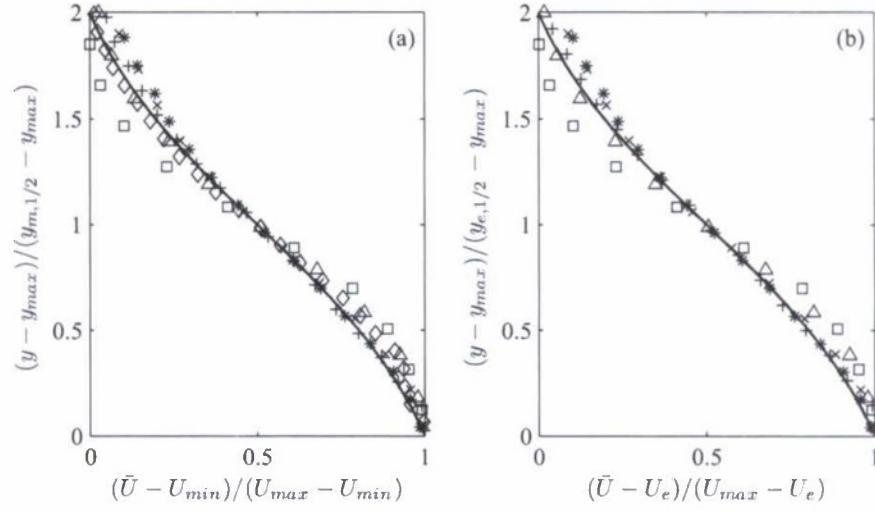
Figure 29: Outer region similarity of $\bar{U}$ using (a) mean shear scales and (b) scales suggested by Launder & Rodi (1983), $Re_c = 6.5 \times 10^5$, $C_\mu = 0.015$, $h/c = 0.0019$. $r\theta/c = $ 0.010, $\triangle$ 0.017, $\times$ 0.025, $*$ 0.032 + 0.040, and $\diamond$ 0.047. The line represents $U = 0.5\left[(1 - 1.315\tanh(y^- 1)\right]$.
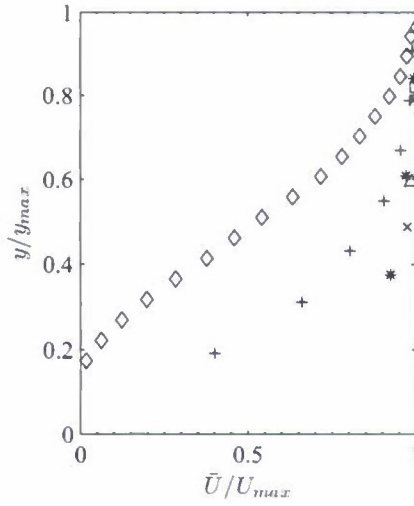
Figure 30: Lack of inner region similarity of $\bar{U}$, $Re_c = 6.5 \times 10^5$, $C_\mu = 0.015$, $h/c = 0.0019$. $r\theta/c = $ 0.010, $\triangle$ 0.017, $\times$ 0.025, $*$ 0.032 + 0.040, and $\diamond$ 0.047.
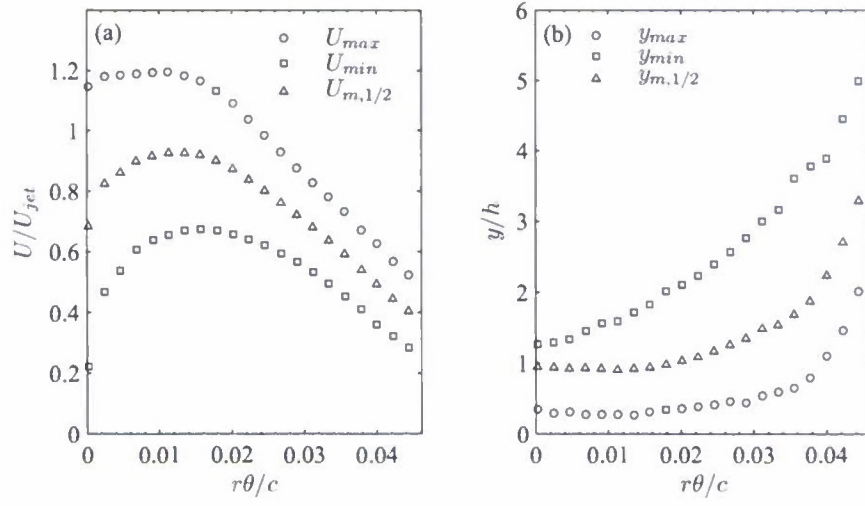
Figure 31: Velocity and length scales describing decay and spread of jet, $Re_c = 6.5 \times 10^5$, $C_\mu = 0.015$, and $h/c = 0.0019$.
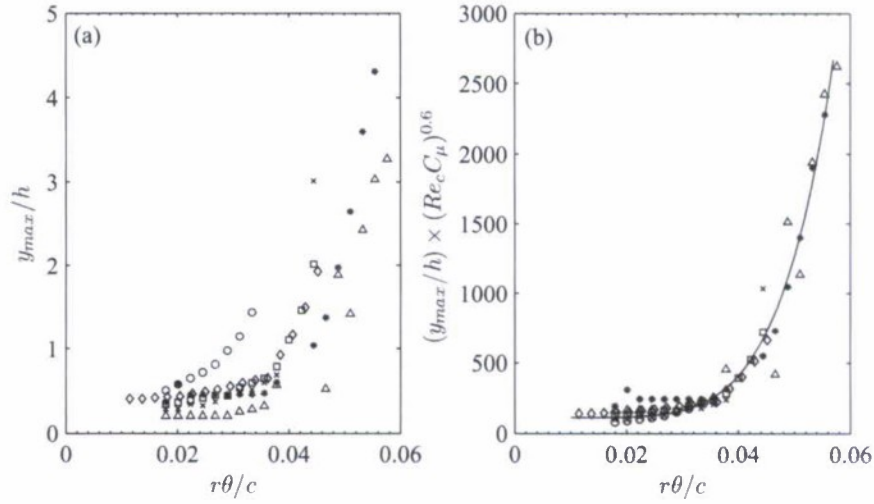
Figure 32: Rate of spread of y_{max}/h and collapsed data with best fit line, $R^2 = 0.95$. See Table 3 for test conditions: ∘ case 1, case 2, △ case 3, × case 4, ∗ case 5, ⋄ case 6.
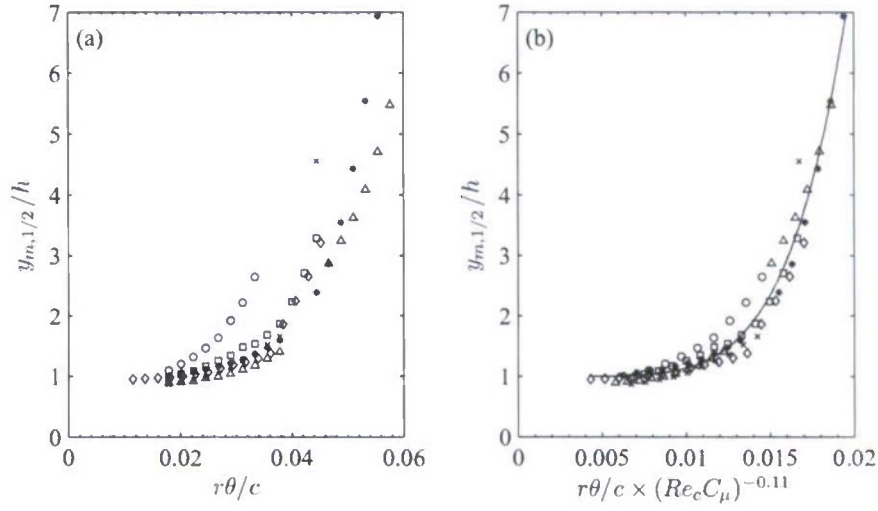
Figure 33: Rate of spread of $y_{m,1/2}/h$ and collapsed data with best fit line, $R^2 = 0.97$. See Table 3 for test conditions: ∘ case 1, case 2, △ case 3, × case 4, ∗ case 5, ◇ case 6.
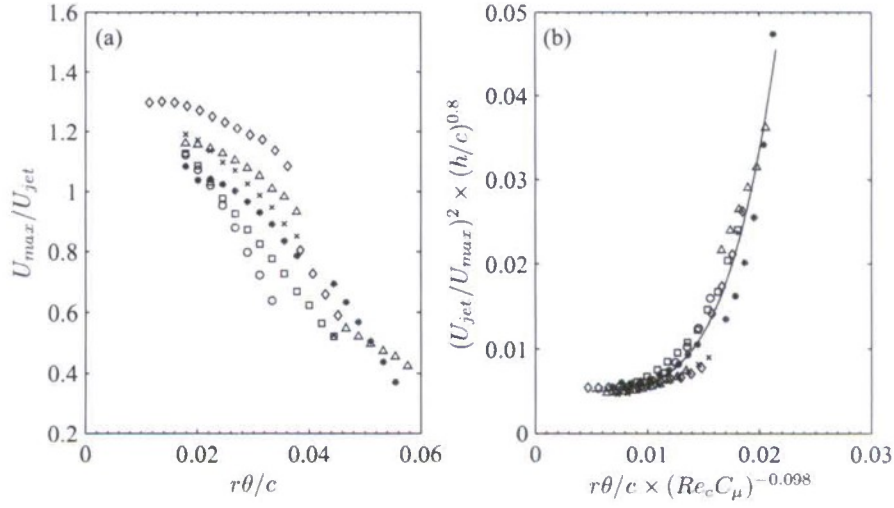
Figure 34: Rate of decay of U_{max}/U_{jet} and collapsed data with best fit line, $R^2 = 0.95$. See Table 3 for test conditions: ∘ case 1, case 2, △ case 3, × case 4, ∗ case 5, ◇ case 6.
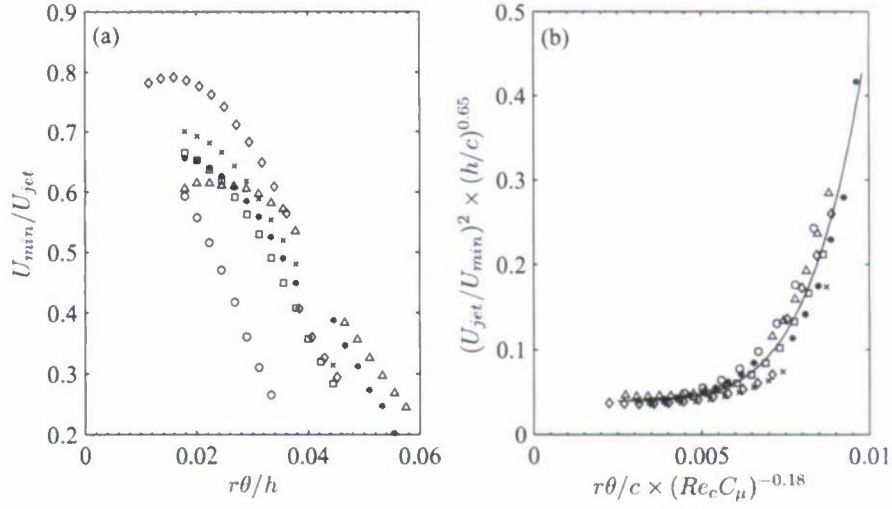
Figure 35: Rate of decay of U_{min}/U_{jet} for all cases listed in table 3, and collapsed data with best fit line, $R^2 = 0.95$. See Table 3 for test conditions: $\circ$ case 1, case 2, $\triangle$ case 3, $\times$ case 4, $*$ case 5, $\diamond$ case 6.
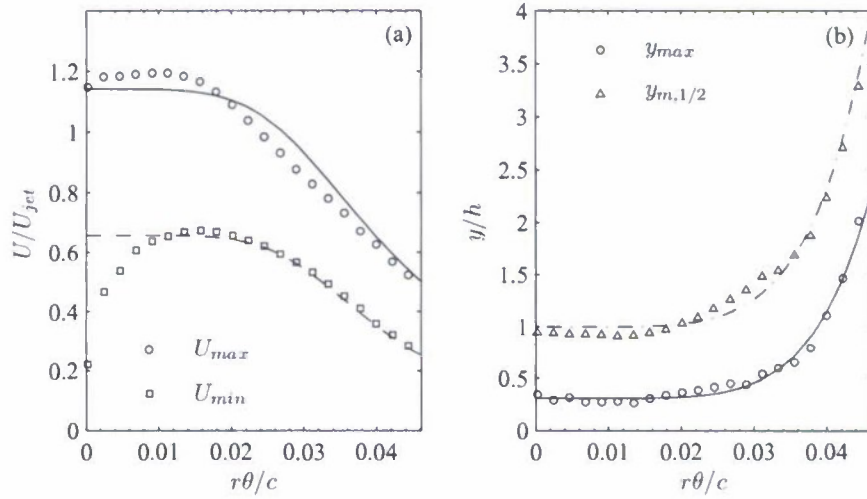
Figure 36: Comparison of measured and predicted (a) velocity scales and (b) length scales, $Re_c = 6.5 \times 10^5$, $C_\mu = 0.015$, $h/c = 0.0019$. Measured scales are represented by datum points, and predicted scales are represented by lines.
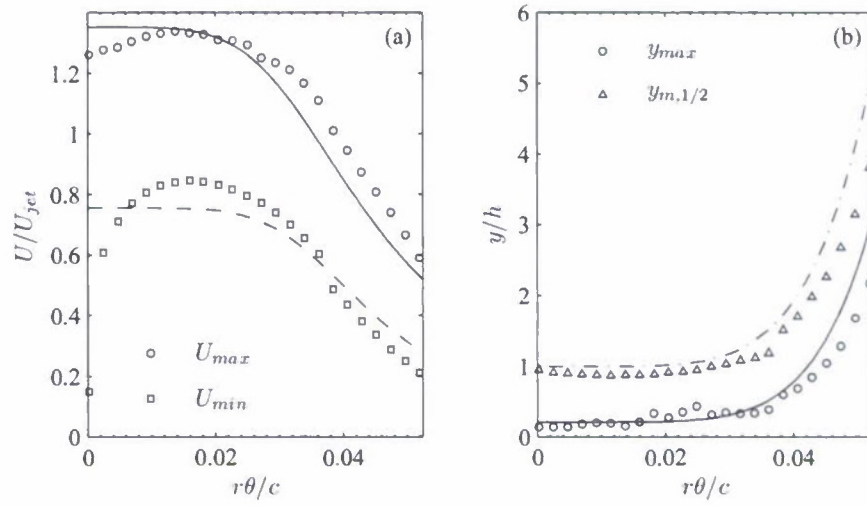
Figure 37: Comparison of measured and predicted (a) velocity scales and (b) length scales, $Re_c = 1.3 \times 10^6$, $C_\mu = 0.014$, $h/c = 0.0029$. Measured scales are represented by datum points, and predicted scales are represented by lines.
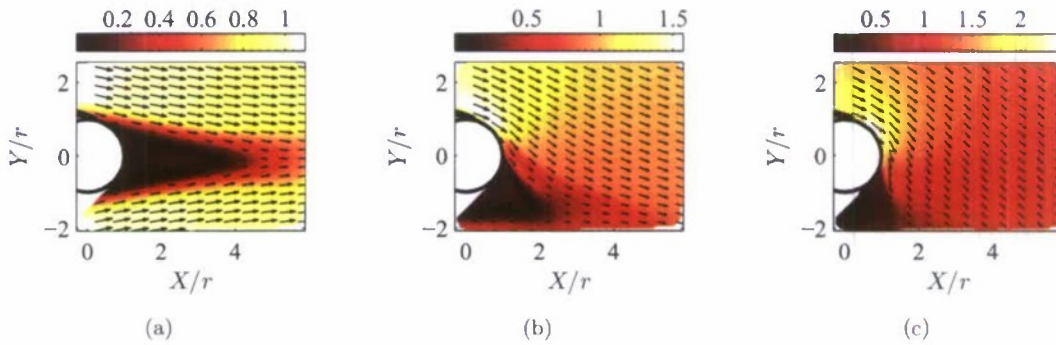
Figure 38: Mean speed ($|\mathbf{V}|/U_\infty$) contours and mean velocity vectors, $Re_c = 6.5 \times 10^5$ and $h/c = 0.0019$. The airfoil trailing edge is sketched for reference. a) $C_\mu = 0$. b) Upper slot blowing, $C_\mu = 0.014$. c) Upper slot blowing, $C_\mu = 0.057$.
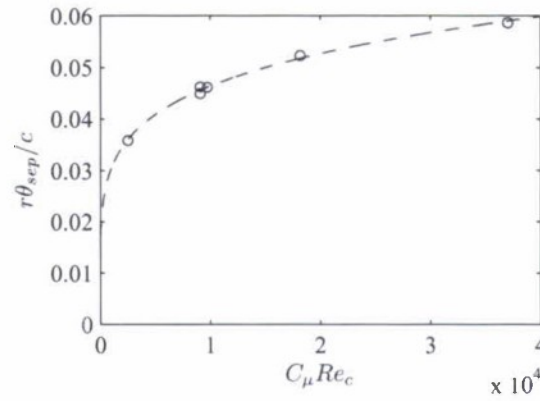
Figure 39: Approximate separation location as a function of $C_\mu Re_c$, ∘ measured, - - - fit ($R^2 = 0.996$).
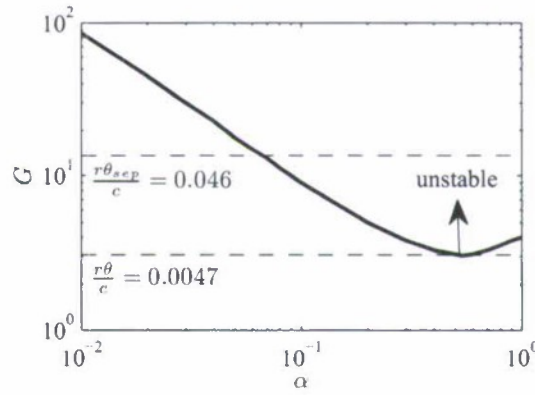
Figure 40: Instability range, indicated by Görtler number, $Re_c = 6.5 \times 10^5$, $C_\mu = 0.015$, $h/c = 0.0019$. The neutral stability curve is computed by Floryan (1986).
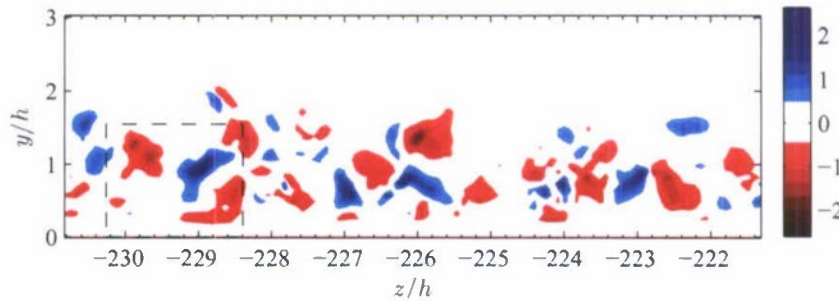
Figure 41: Instantaneous spanwise vorticity ($\omega_x h/U_{jet}$) distribution, $Re_c = 5.6 \times 10^5$, $C_\mu = 0.014$, $h/c = 0.0019$. The origin of z/h is located at midspan.

63
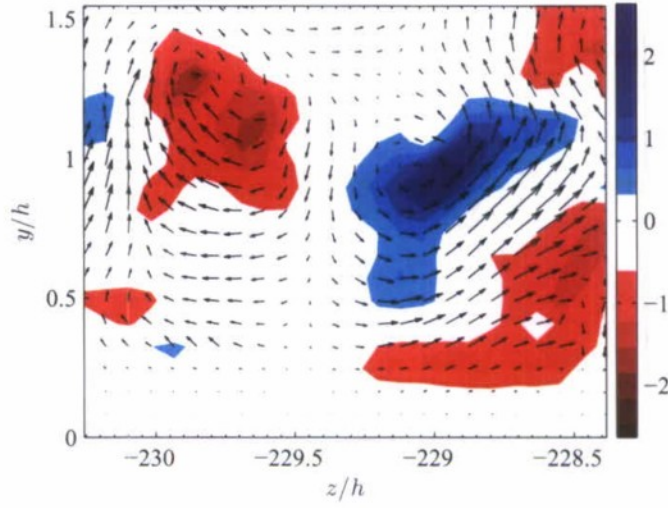
Figure 42: Instantaneous spanwise vorticity ($\omega_x h/U_{jet}$) distribution and instantaneous velocity vectors reveal presence of counter-rotating pair of vortices, $Re_c = 5.6 \times 10^5$, $C_\mu = 0.014$, $h/c = 0.0019$. The origin of z/h is located at midspan.
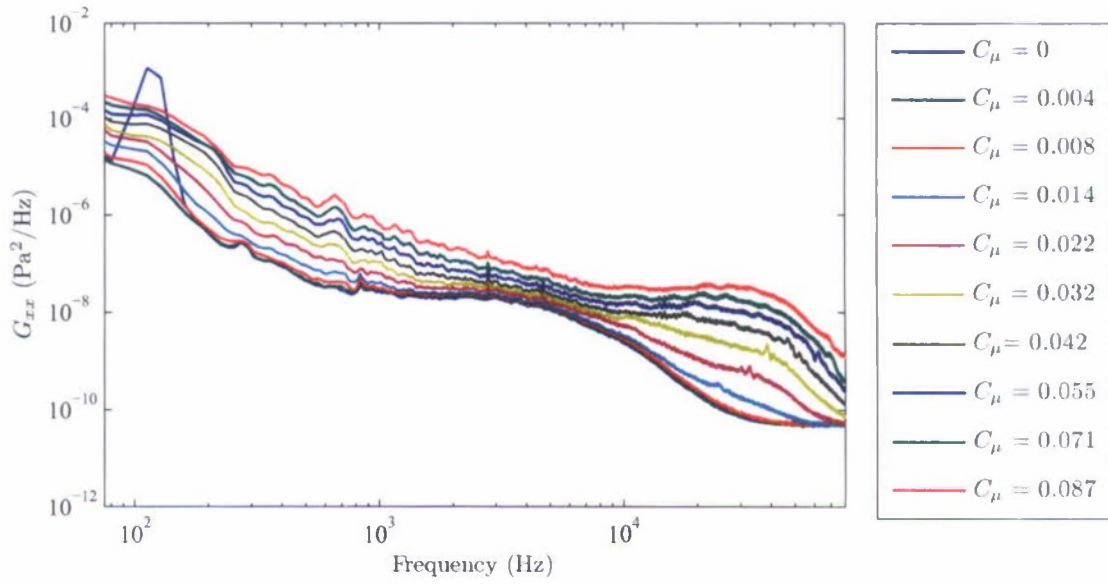
Figure 43: Power spectral density measured by microphone M1 above the trailing edge, $Re_c = 6.5 \times 10^5$, $h/c = 0.0019$.
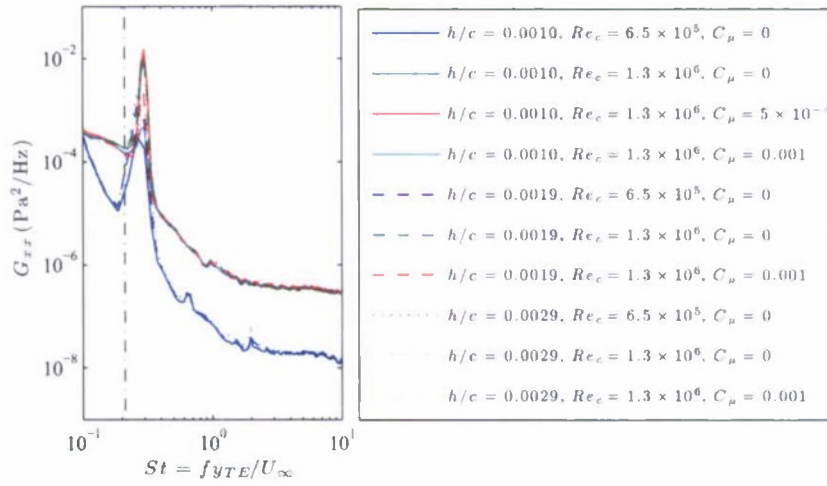
Figure 44: All cases with trailing edge vortex shedding tones measured by microphone M1. The vertical line corresponds to $St = 0.21$.
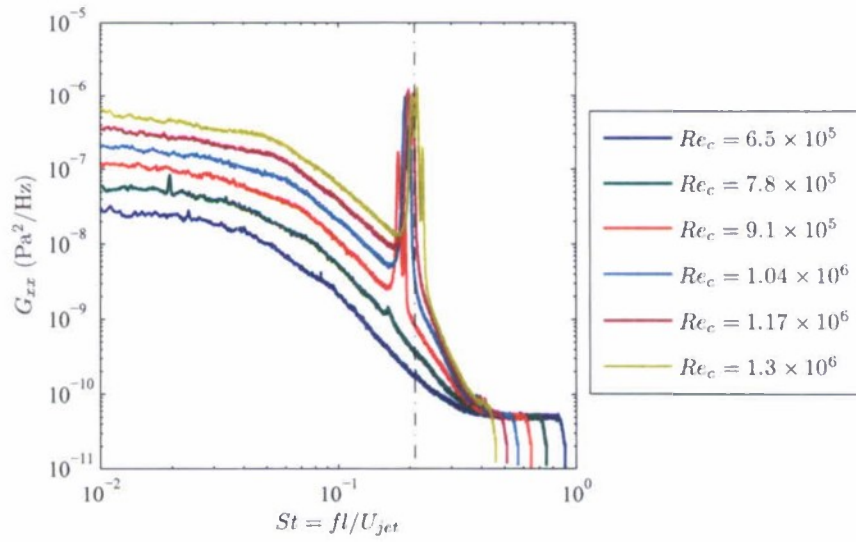
Figure 45: Slot lip vortex shedding tones measured by microphone M1, $C_\mu = 0.014$, $h/c = 0.0029$.
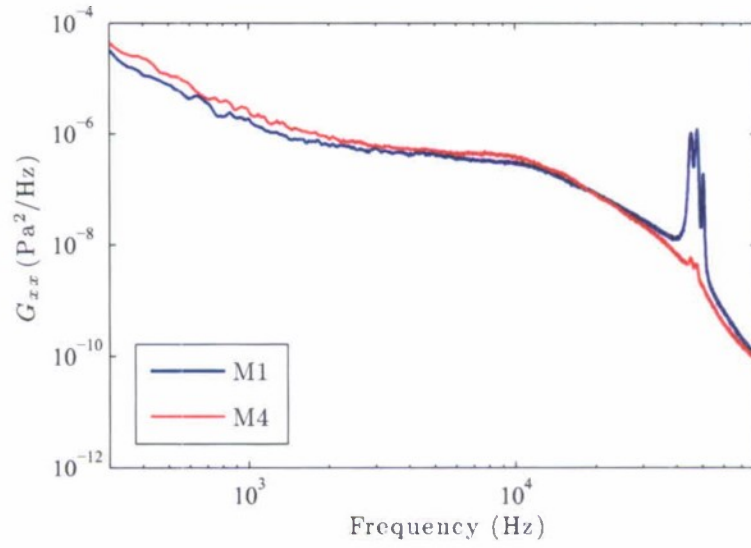
Figure 46: Slot lip vortex shedding tones measured by microphones M1 and M4 (see Figure 4), $Re_c = 1.3 \times 10^6$, $C_\mu = 0.014$, $h/c = 0.0029$.
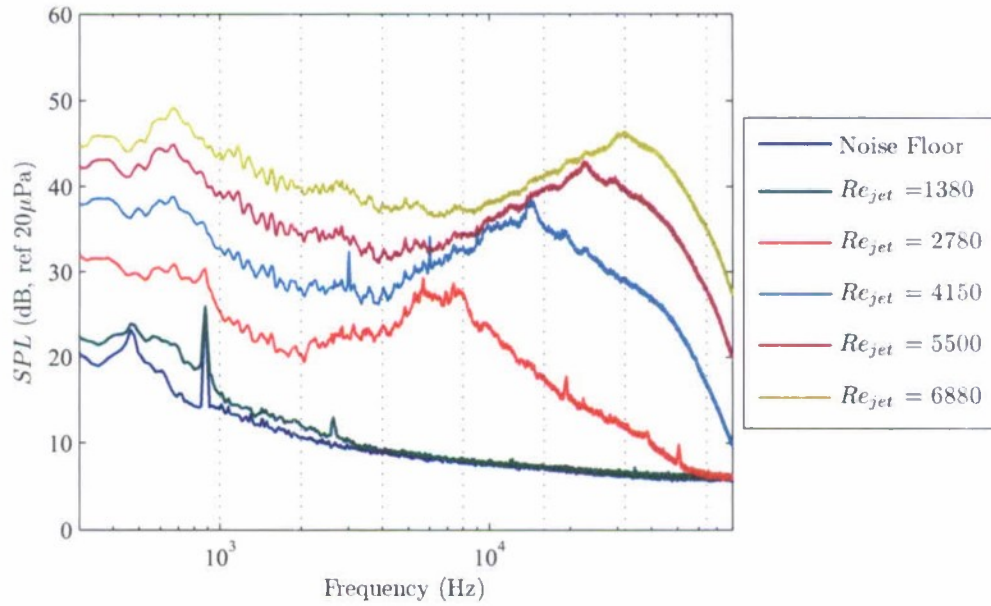
Figure 47: Spectra (16 Hz bin width) measured by the center microphone above the trailing edge, SSB, $U_\infty = 0$, $h/c = 0.0019$. The vertical lines represent the frequencies where beam maps are produced.
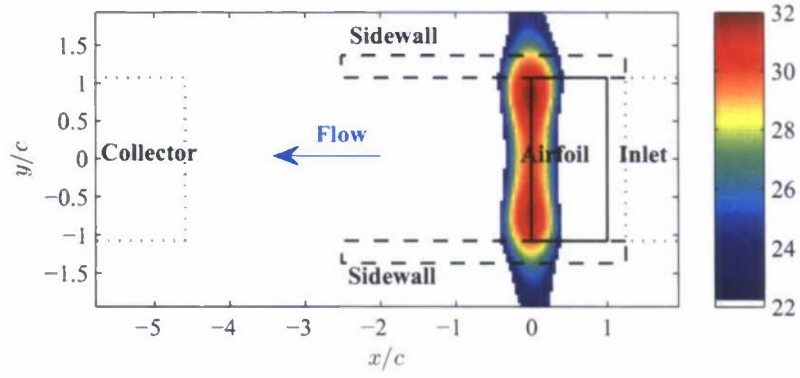
Figure 48: Sample beam map with airfoil and tunnel components labeled.
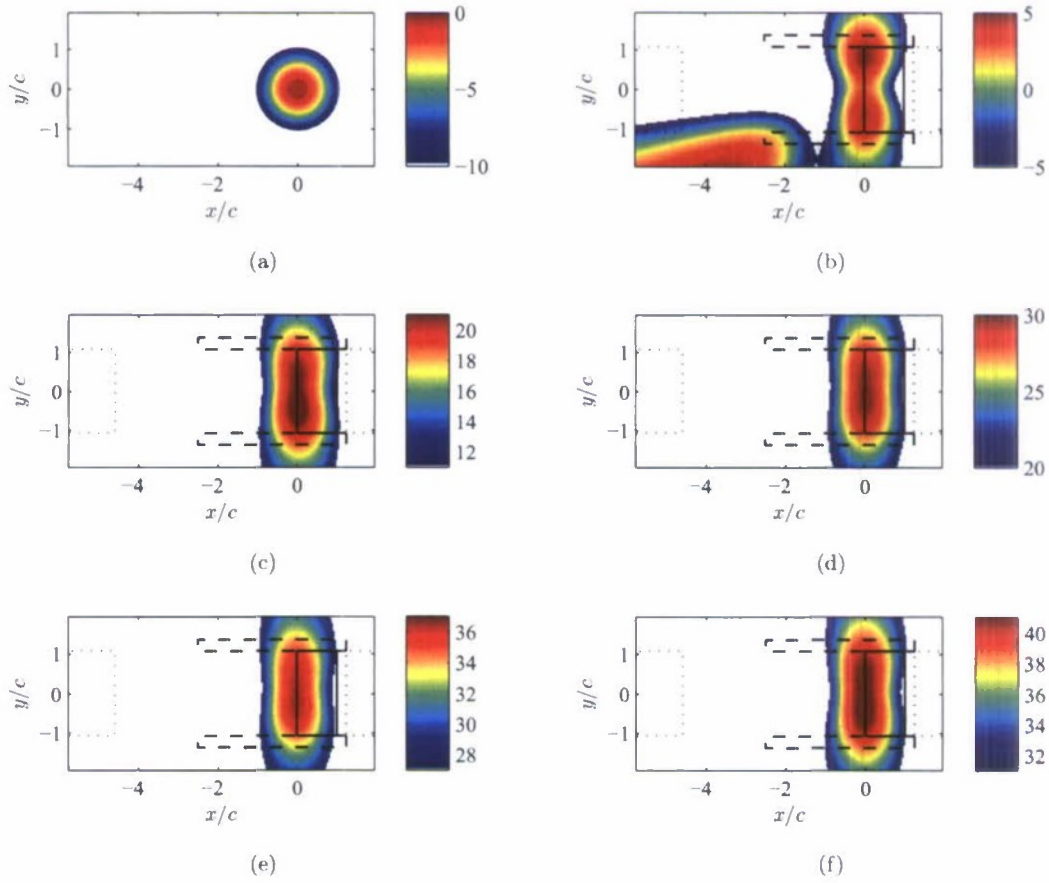
Figure 49: Outer array beam maps (dB) at 992 Hz, SSB, $U_\infty = 0$, $h/c = 0.0019$. a) Array PSF. b) $Re_{jet} = 1340$. c) $Re_{jet} = 2680$. d) $Re_{jet} = 3980$. e) $Re_{jet} = 5300$. f) $Re_{jet} = 6600$.
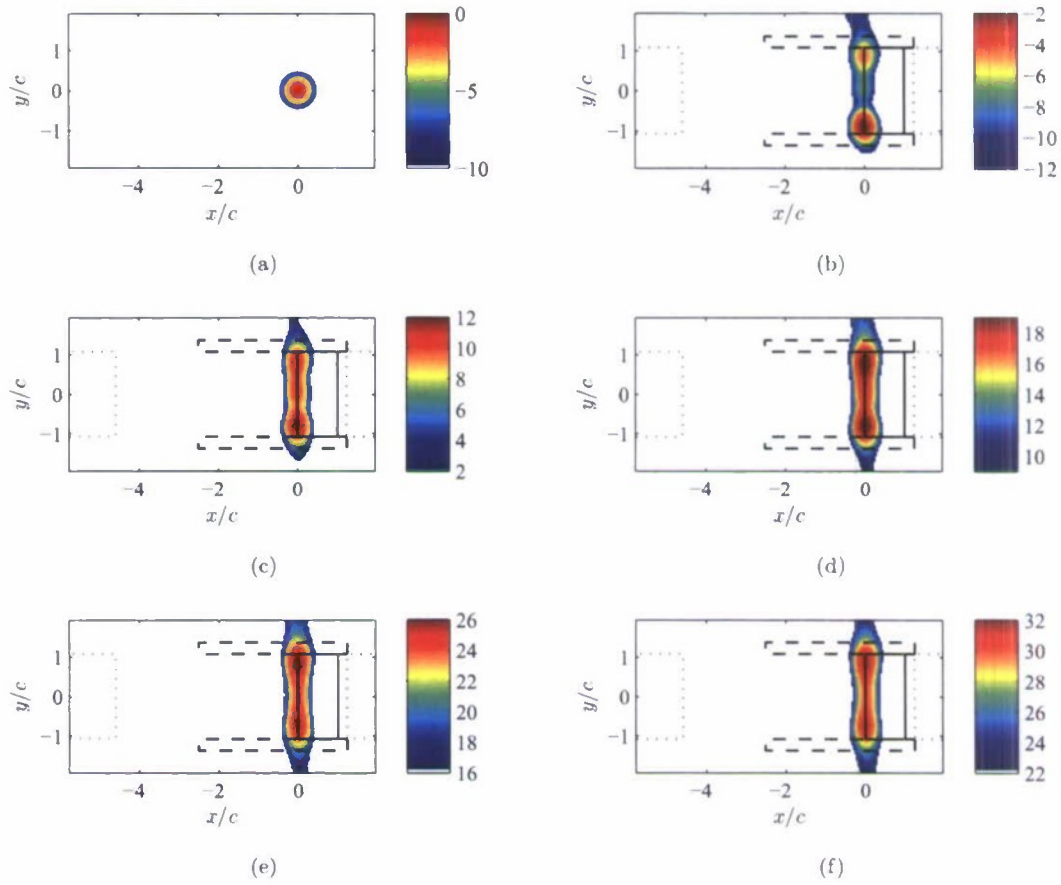
Figure 50: Outer array beam maps (dB) at 2 kHz, SSB, $U_\infty = 0$, $h/c = 0.0019$. a) Array PSF. b) $Re_{jet} = 1340$. c) $Re_{jet} = 2680$. d) $Re_{jet} = 3980$. c) $Re_{jet} = 5300$. f) $Re_{jet} = 6600$.
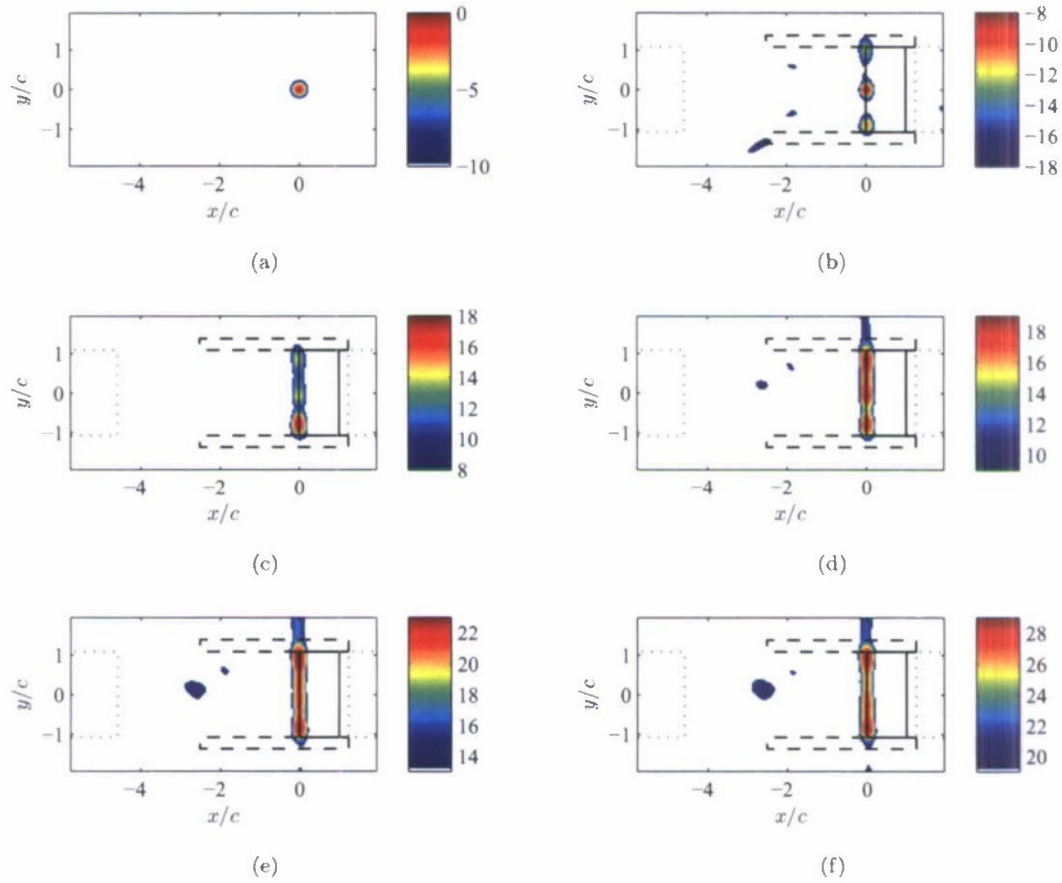
Figure 51: Outer array beam maps (dB) at 4 kHz, SSB, $U_\infty = 0$, $h/c = 0.0019$. a) Array PSF. b) $Re_{jet} = 1340$. c) $Re_{jet} = 2680$. d) $Re_{jet} = 3980$. e) $Re_{jet} = 5300$. f) $Re_{jet} = 6600$.
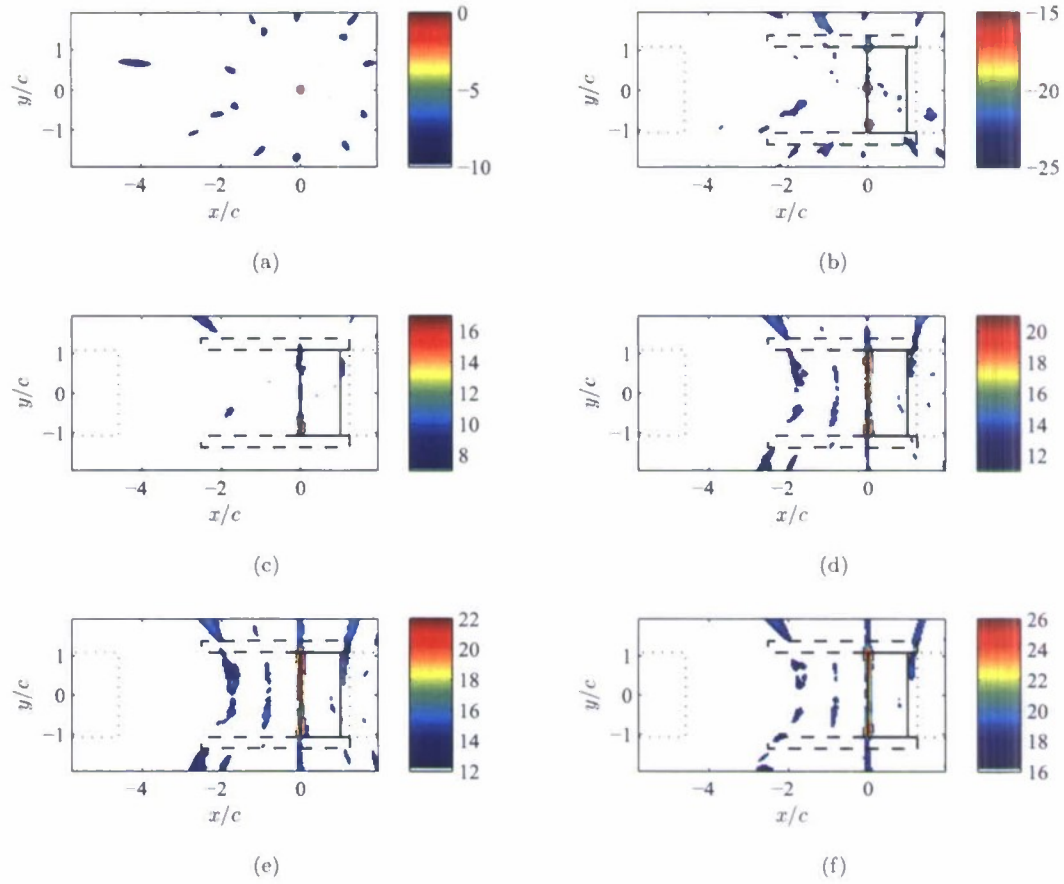
Figure 52: Outer array beam maps (dB) at 8 kHz, SSB, $U_\infty = 0$, $h/c = 0.0019$. a) Array PSF. b) $Re_{jet} = 1340$. c) $Re_{jet} = 2680$. d) $Re_{jet} = 3980$. e) $Re_{jet} = 5300$. f) $Re_{jet} = 6600$.
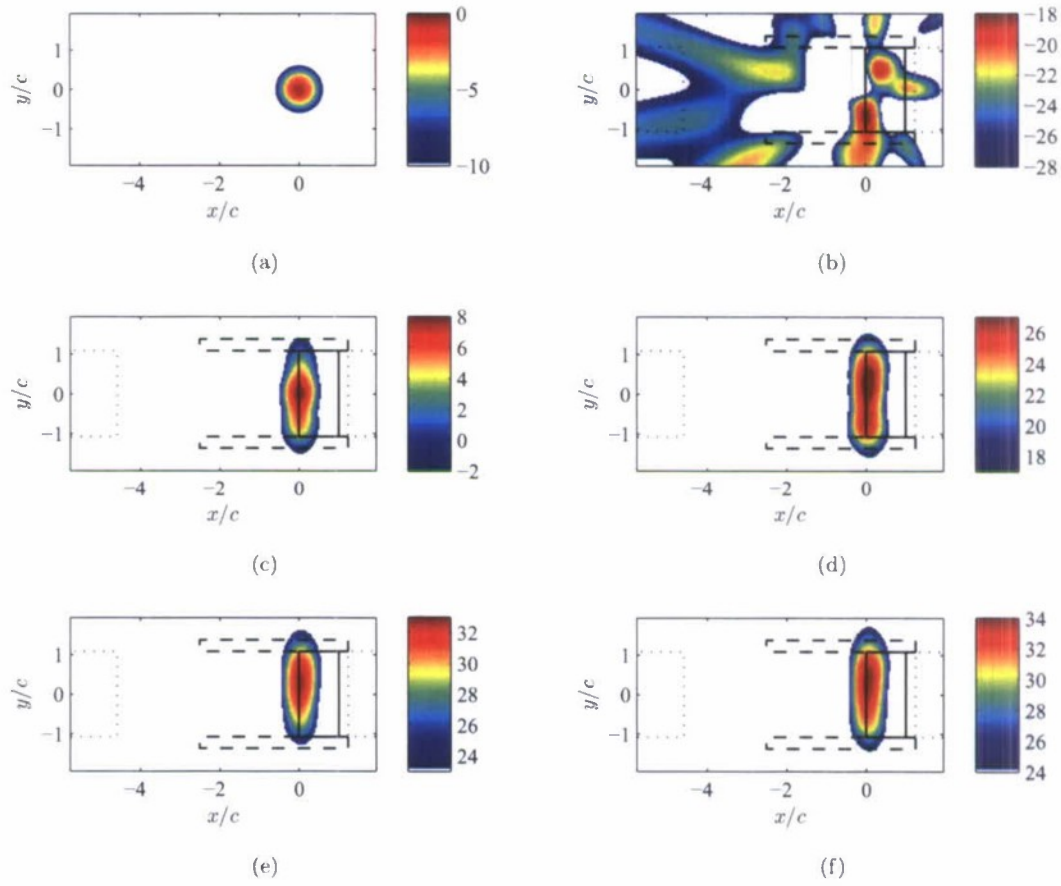
Figure 53: Inner array beam maps (dB) at 16 kHz, SSB, $U_\infty = 0$, $h/c = 0.0019$. a) Array PSF. b) $Re_{jet} = 1340$. c) $Re_{jet} = 2680$. d) $Re_{jet} = 3980$. e) $Re_{jet} = 5300$. f) $Re_{jet} = 6600$.
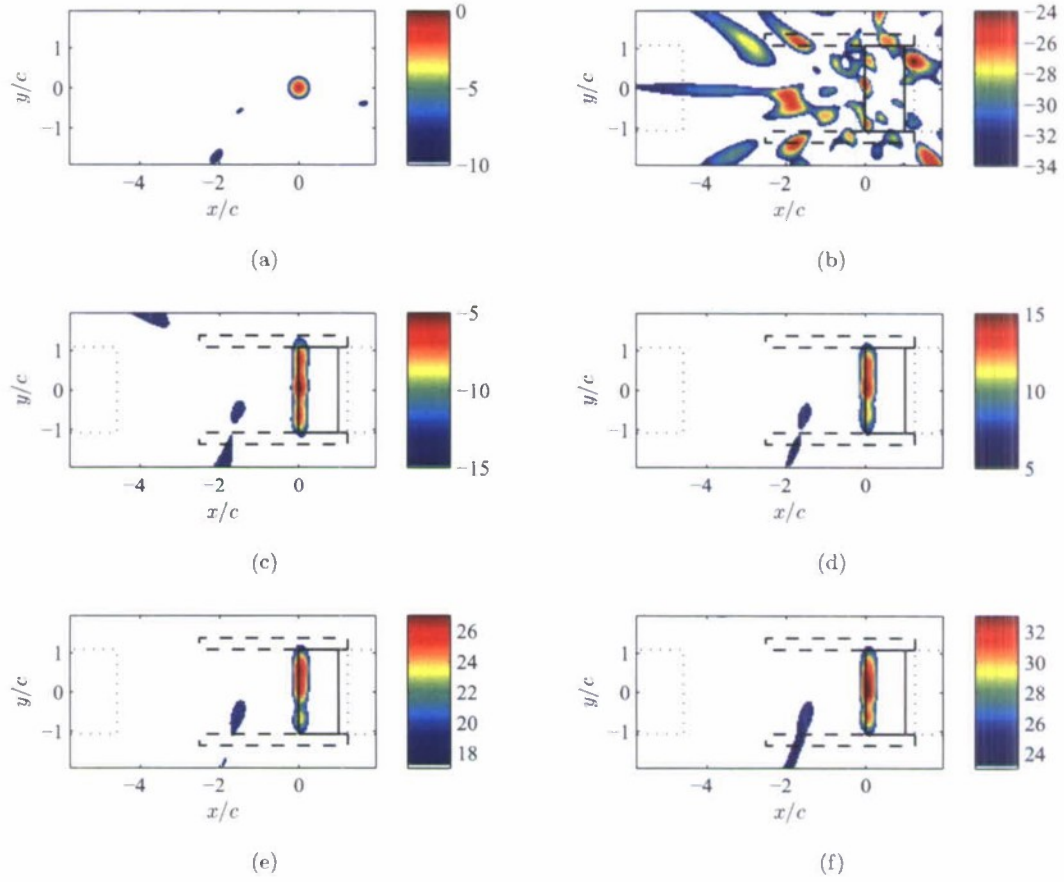
Figure 54: Inner array beam maps (dB) at 32 kHz, SSB, $U_\infty = 0$, $h/c = 0.0019$. a) Array PSF. b) $Re_{jet} = 1340$. c) $Re_{jet} = 2680$. d) $Re_{jet} = 3980$. e) $Re_{jet} = 5300$. f) $Re_{jet} = 6600$.
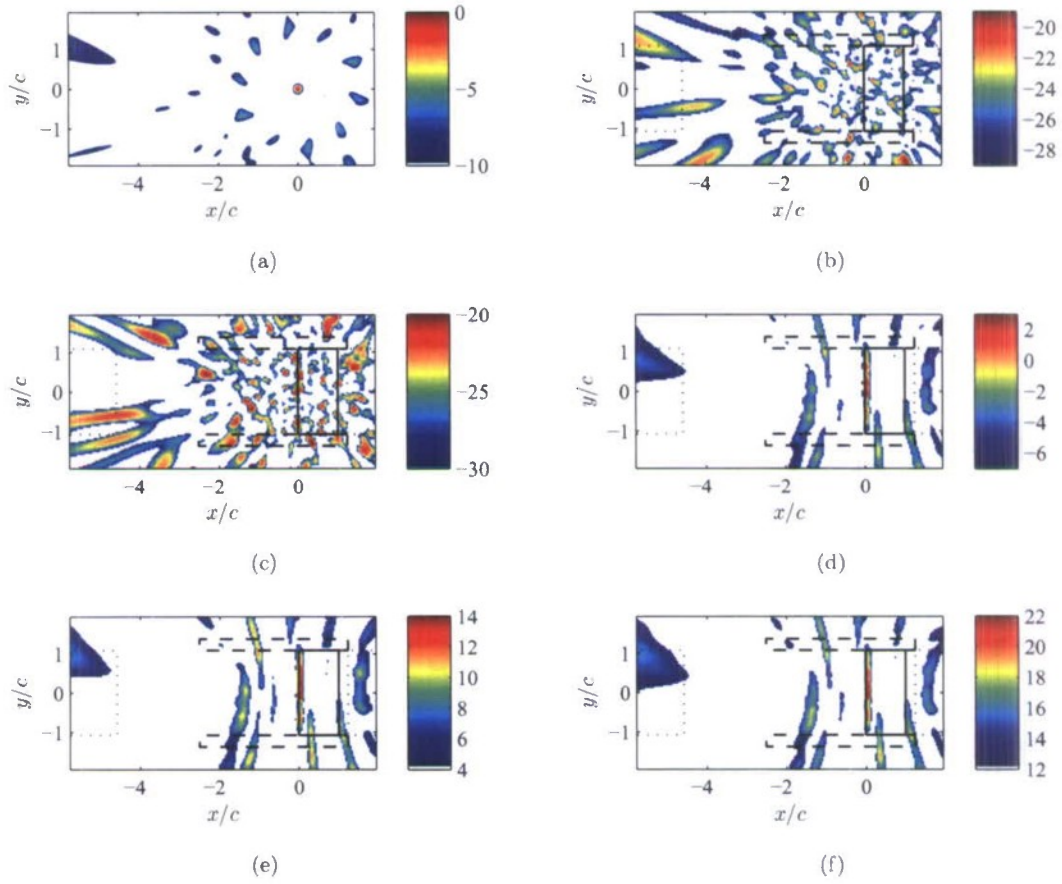
Figure 55: Inner array beam maps (dB) at 64 kHz, SSB, $U_\infty = 0$, $h/c = 0.0019$. a) Array PSF. b) $Re_{jet} = 1340$. c) $Re_{jet} = 2680$. d) $Re_{jet} = 3980$. e) $Re_{jet} = 5300$. f) $Re_{jet} = 6600$.
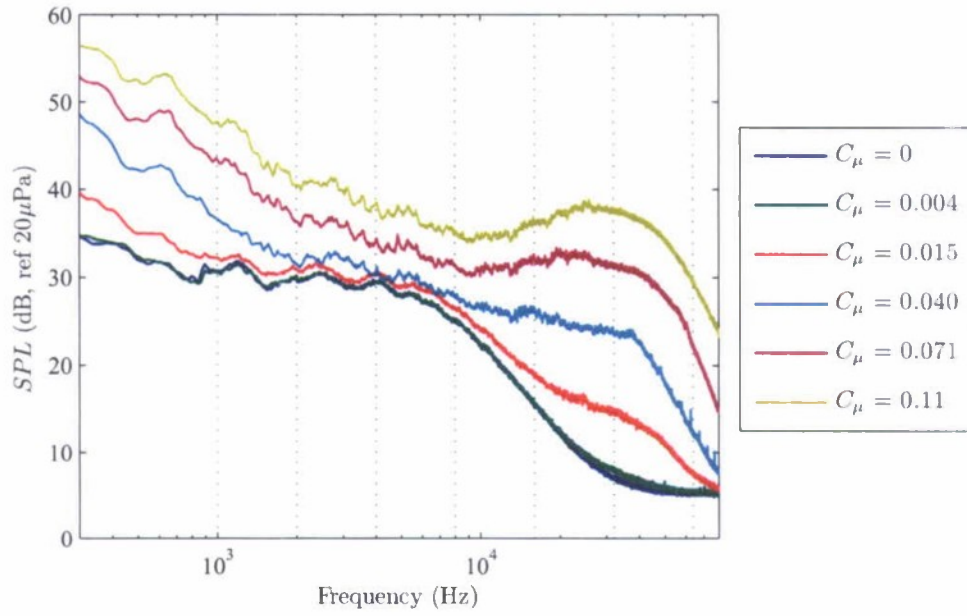
Figure 56: Spectra (16 Hz bin width) measured by the center microphone above the trailing edge, SSB, $Re_c = 6.5 \times 10^5$, $h/c = 0.0019$. The vertical lines represent the frequencies where beam maps are produced.
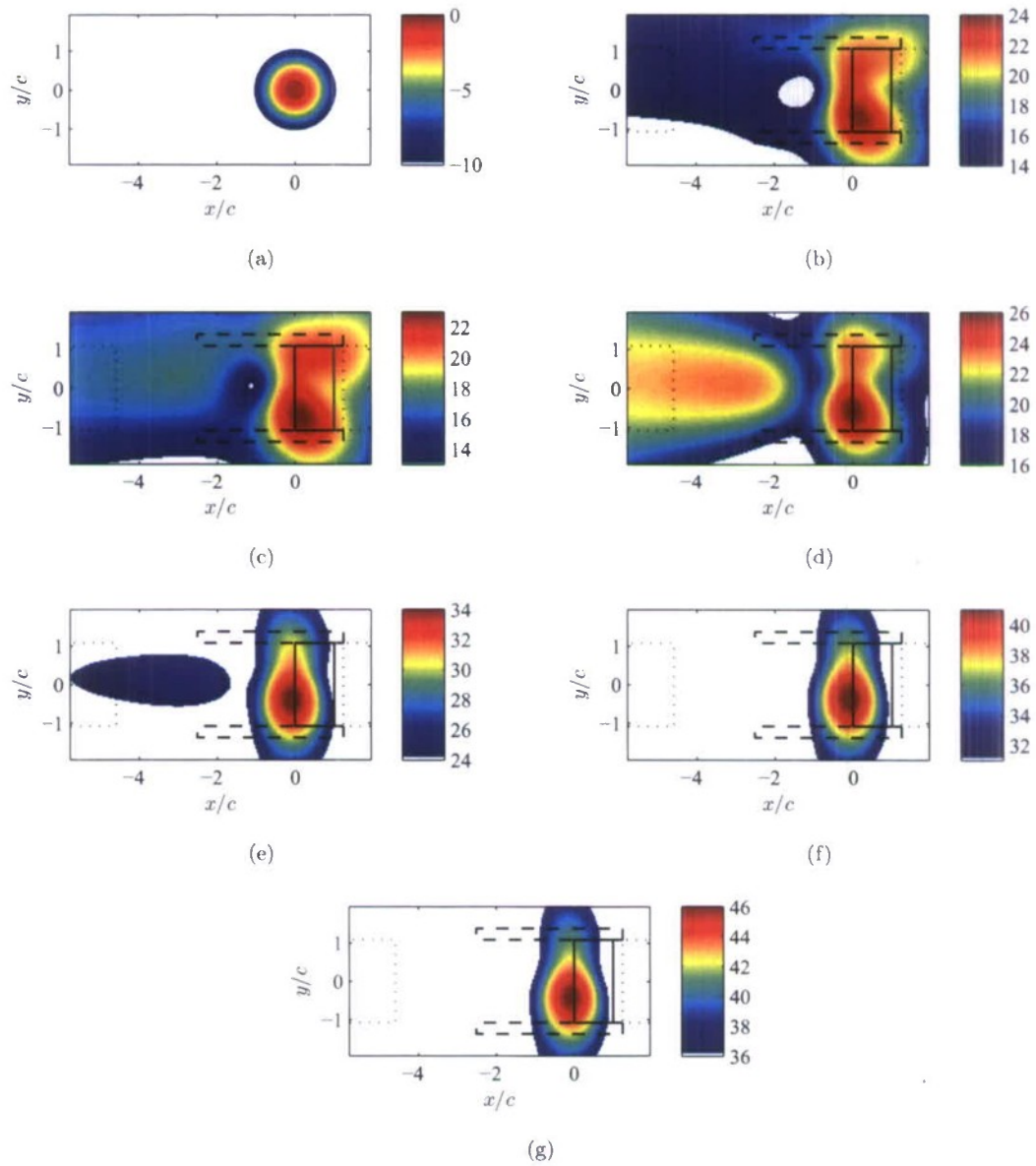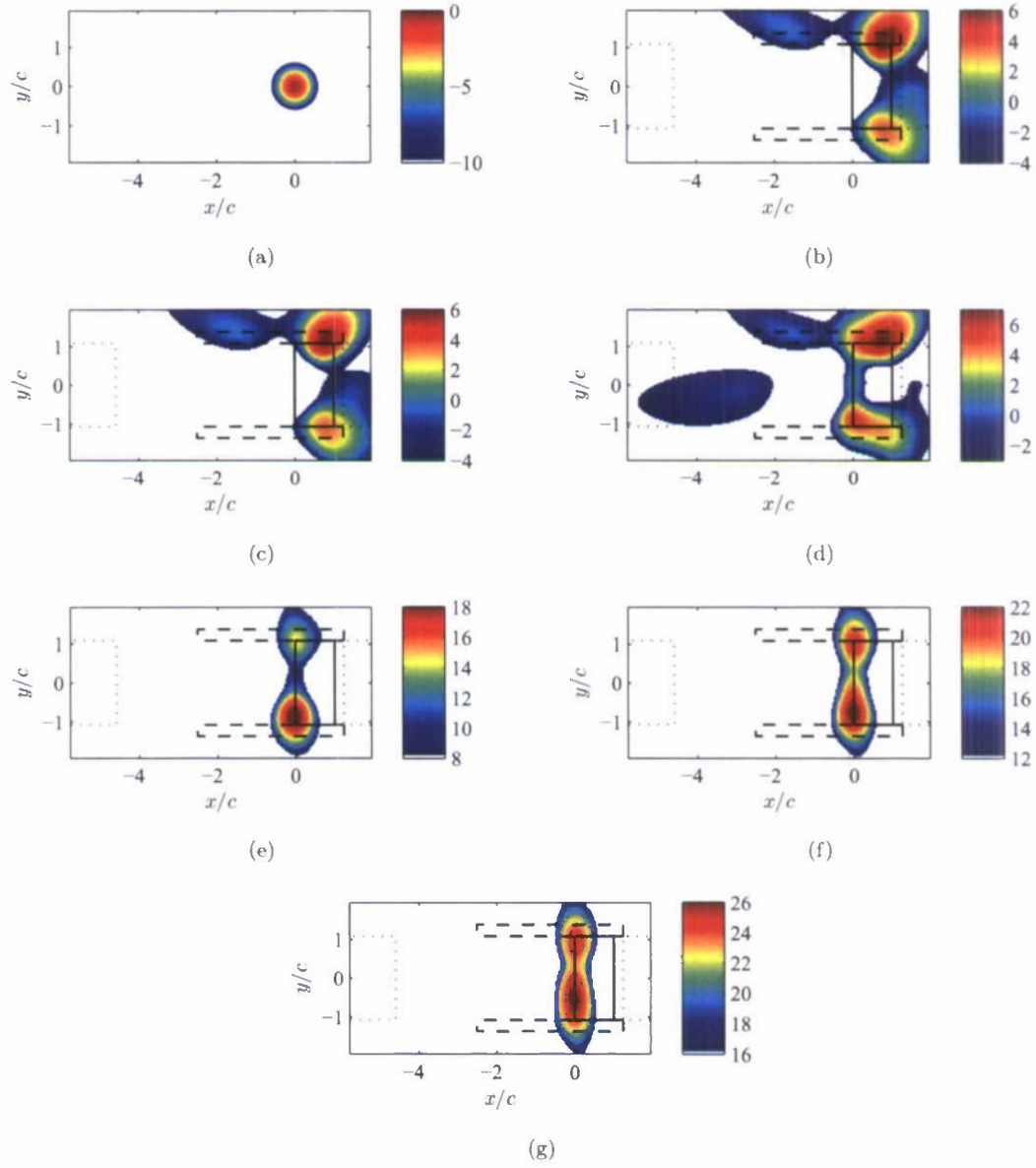
Figure 57: Outer array beam maps (dB) at 992 Hz, SSB, $Re_c = 6.5 \times 10^5$, $h/c = 0.0019$. a) Array PSF. b) $C_\mu = 0$. c) $C_\mu = 0.004$ ($Re_{jet} = 1330$). d) $C_\mu = 0.017$ ($Re_{jet} = 2660$). e) $C_\mu = 0.037$ ($Re_{jet} = 4000$). f) $C_\mu = 0.065$ ($Re_{jet} = 5300$). g) $C_\mu = 0.10$ ($Re_{jet} = 6640$).
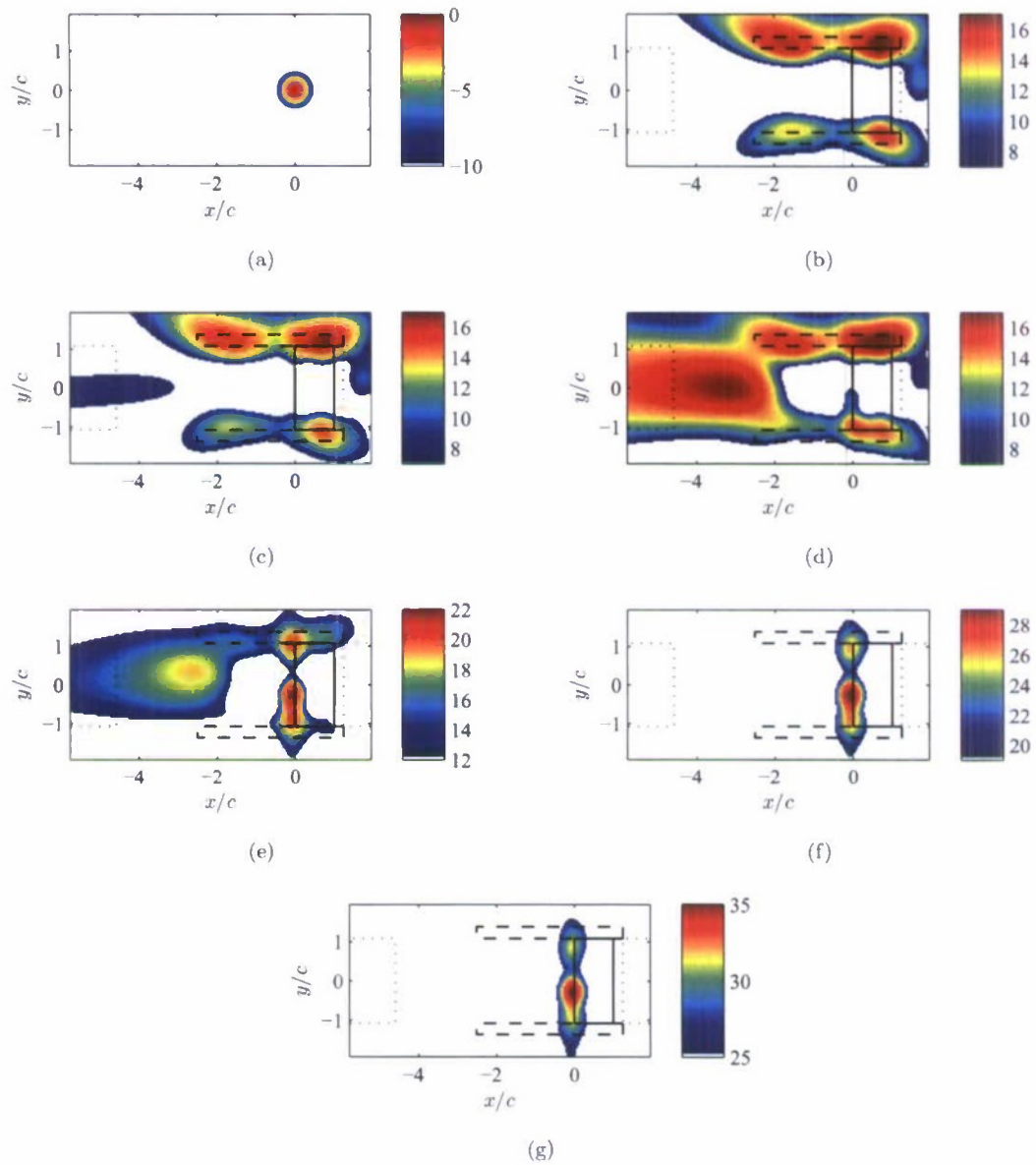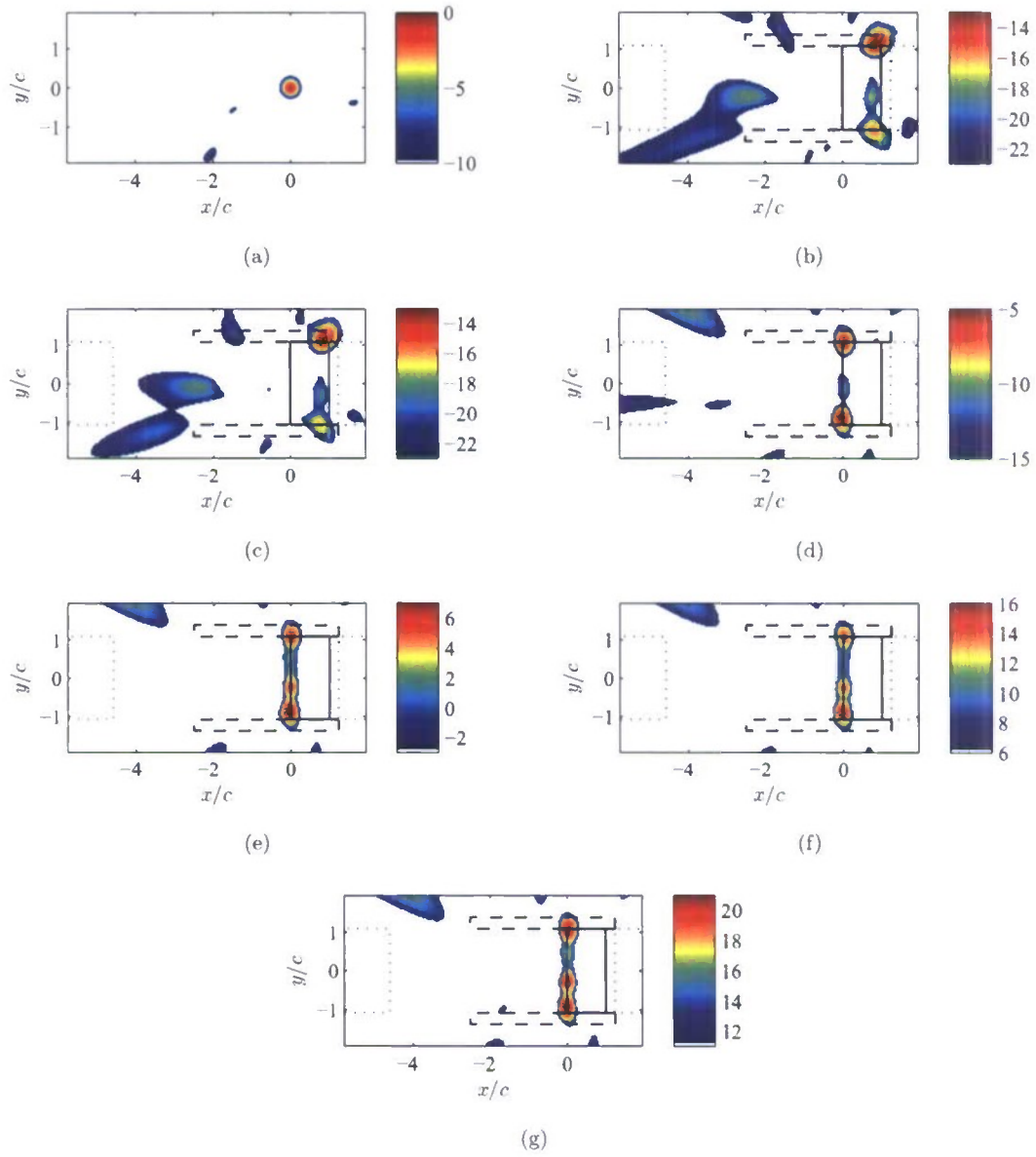
Figure 58: Outer array beam maps (dB) at 2 kHz, SSB, $Re_c = 6.5 \times 10^5$, $h/c = 0.0019$. a) Array PSF. b) $C_\mu = 0$. c) $C_\mu = 0.004$ ($Re_{jet} = 1330$). d) $C_\mu = 0.017$ ($Re_{jet} = 2660$). e) $C_\mu = 0.037$ ($Re_{jet} = 4000$). f) $C_\mu = 0.065$ ($Re_{jet} = 5300$). g) $C_\mu = 0.10$ ($Re_{jet} = 6640$).
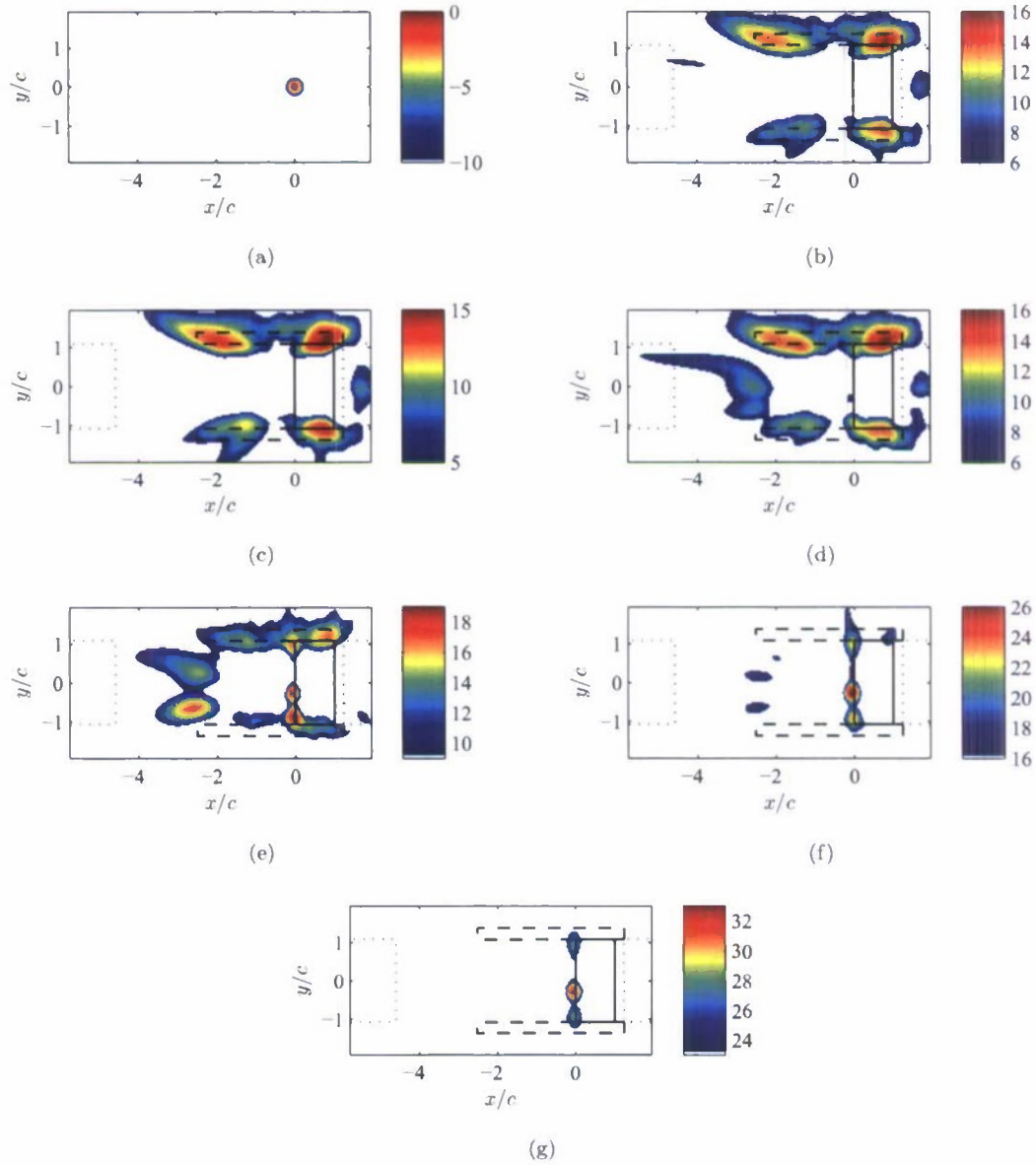
Figure 59: Outer array beam maps (dB) at 4 kHz, SSB, $Re_c = 6.5 \times 10^5$, $h/c = 0.0019$. a) Array PSF. b) $C_\mu = 0$. c) $C_\mu = 0.004$ ($Re_{jet} = 1330$). d) $C_\mu = 0.017$ ($Re_{jet} = 2660$). e) $C_\mu = 0.037$ ($Re_{jet} = 4000$). f) $C_\mu = 0.065$ ($Re_{jet} = 5300$). g) $C_\mu = 0.10$ ($Re_{jet} = 6640$).
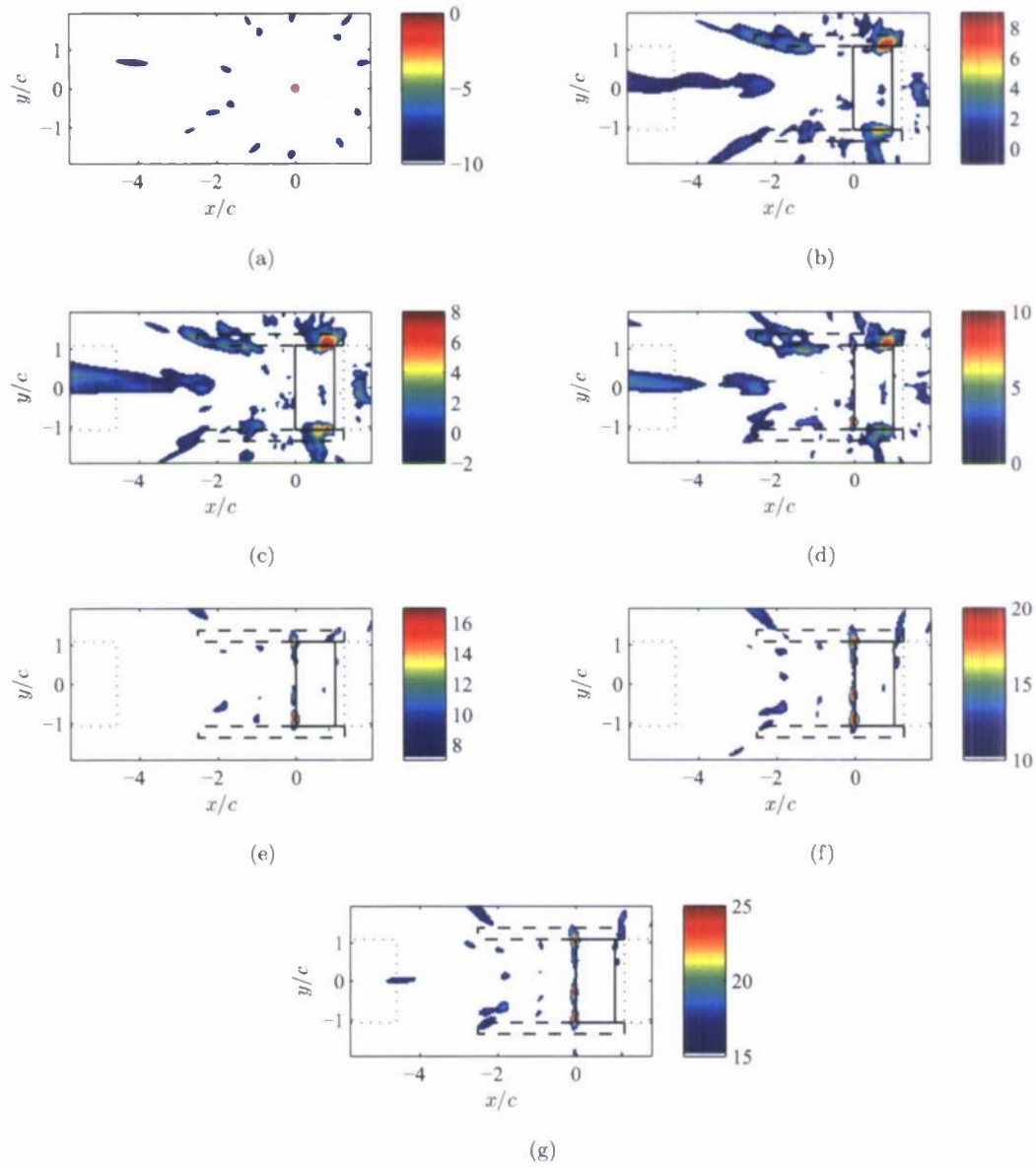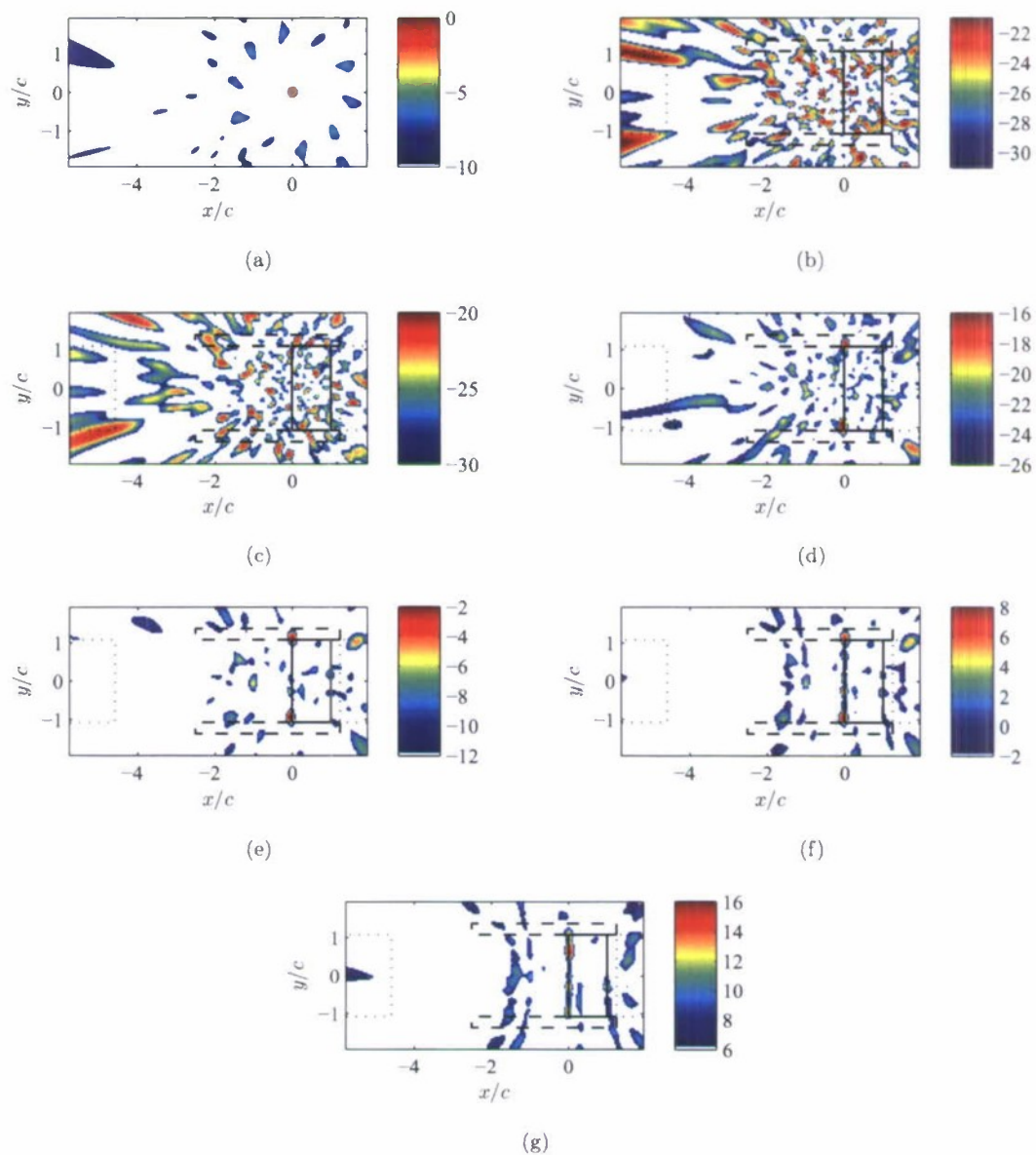
Figure 60: Outer array beam maps (dB) at 8 kHz, SSB, $Re_c = 6.5 \times 10^5$, $h/c = 0.0019$. a) Array PSF. b) $C_\mu = 0$. c) $C_\mu = 0.004$ ($Re_{jet} = 1330$). d) $C_\mu = 0.017$ ($Re_{jet} = 2660$). e) $C_\mu = 0.037$ ($Re_{jet} = 4000$). f) $C_\mu = 0.065$ ($Re_{jet} = 5300$). g) $C_\mu = 0.10$ ($Re_{jet} = 6640$).

Figure 61: Inner array beam maps (dB) at 16 kHz, SSB, $Re_c = 6.5 \times 10^5$, $h/c = 0.0019$. a) Array PSF. b) $C_\mu = 0$. c) $C_\mu = 0.004$ ($Re_{jet} = 1330$). d) $C_\mu = 0.017$ ($Re_{jet} = 2660$). e) $C_\mu = 0.037$ ($Re_{jet} = 4000$). f) $C_\mu = 0.065$ ($Re_{jet} = 5300$). g) $C_\mu = 0.10$ ($Re_{jet} = 6640$).

Figure 62: Inner array beam maps (dB) at 32 kHz, SSB, $Re_c = 6.5 \times 10^5$, $h/c = 0.0019$. a) Array PSF. b) $C_\mu = 0$. c) $C_\mu = 0.004$ ($Re_{jet} = 1330$). d) $C_\mu = 0.017$ ($Re_{jet} = 2660$). e) $C_\mu = 0.037$ ($Re_{jet} = 4000$). f) $C_\mu = 0.065$ ($Re_{jet} = 5300$). g) $C_\mu = 0.10$ ($Re_{jet} = 6640$).

Figure 63: Inner array beam maps (dB) at 64 kHz, SSB, $Re_c = 6.5 \times 10^5$, $h/c = 0.0019$. a) Array PSF. b) $C_\mu = 0$. c) $C_\mu = 0.004$ ($Re_{jet} = 1330$). d) $C_\mu = 0.017$ ($Re_{jet} = 2660$). e) $C_\mu = 0.037$ ($Re_{jet} = 4000$). f) $C_\mu = 0.065$ ($Re_{jet} = 5300$). g) $C_\mu = 0.10$ ($Re_{jet} = 6640$).
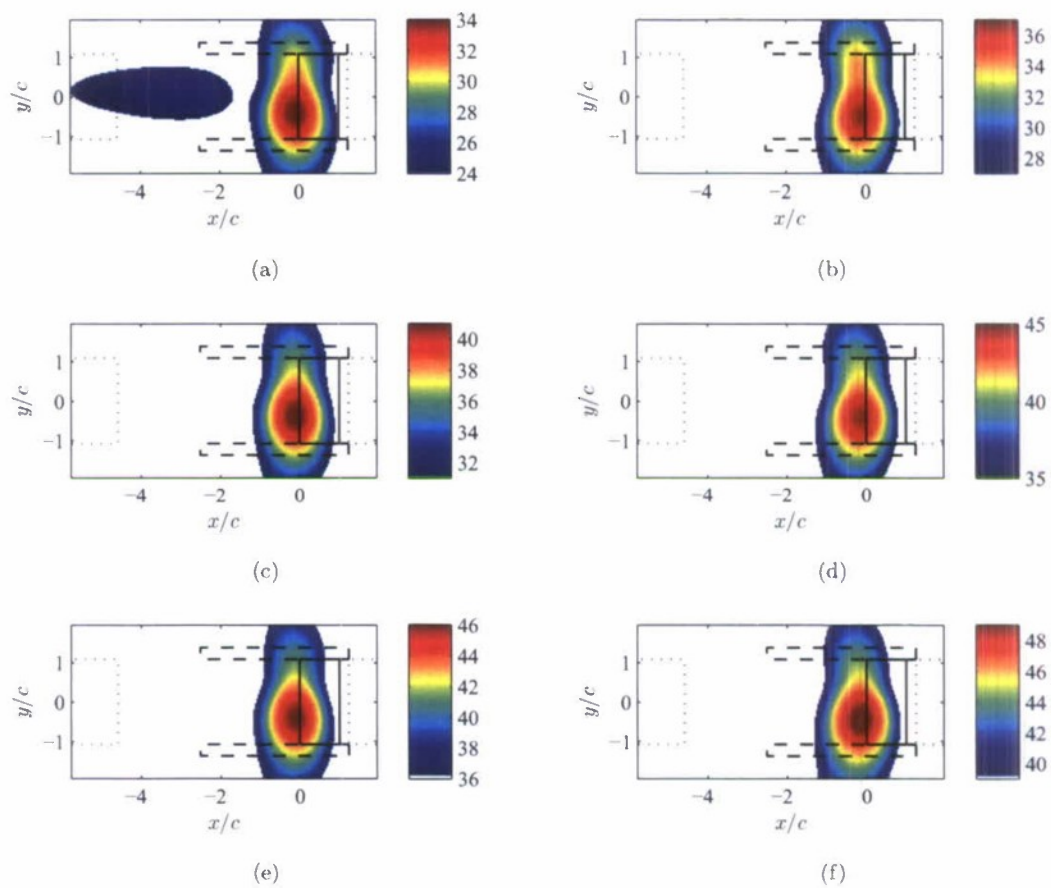
Figure 64: Outer array beam maps (dB) at 992 Hz, $Re_c = 6.5 \times 10^5$, $h/c = 0.0019$. a) SSB, $C_\mu = 0.037$. b) OSB, $C_\mu = 0.040$. c) SSB, $C_\mu = 0.065$. d) OSB, $C_\mu = 0.071$. e) SSB, $C_\mu = 0.10$. f) OSB, $C_\mu = 0.11$.
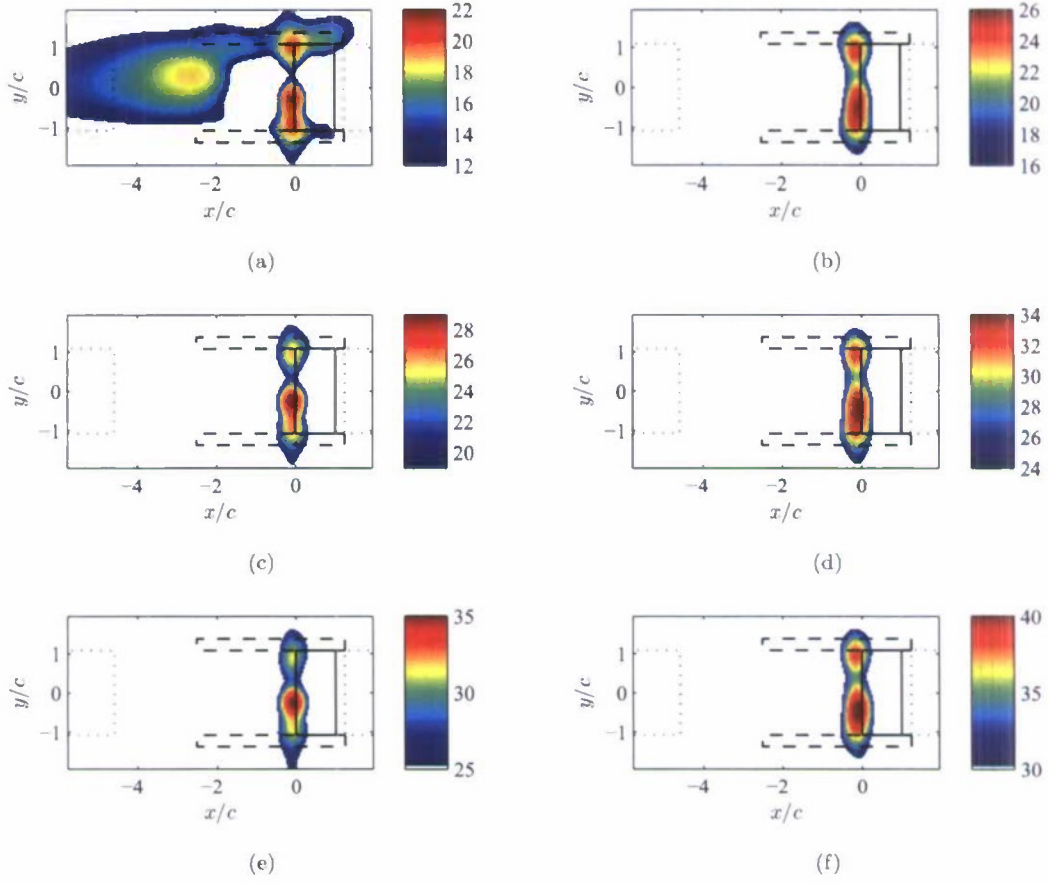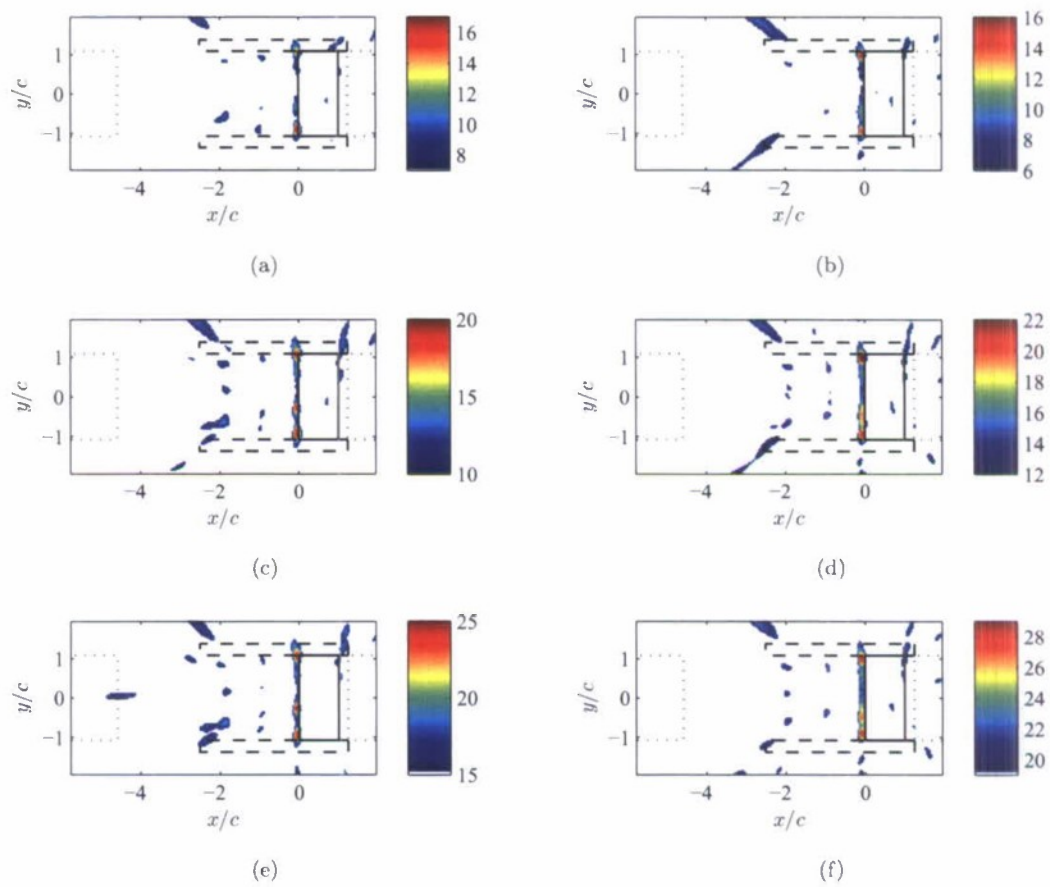
Figure 65: Outer array beam maps (dB) at 2 kHz, $Re_c = 6.5 \times 10^5$, $h/c = 0.0019$. a) SSB, $C_\mu = 0.037$. b) OSB, $C_\mu = 0.040$. c) SSB, $C_\mu = 0.065$. d) OSB, $C_\mu = 0.071$. e) SSB, $C_\mu = 0.10$. f) OSB, $C_\mu = 0.11$.
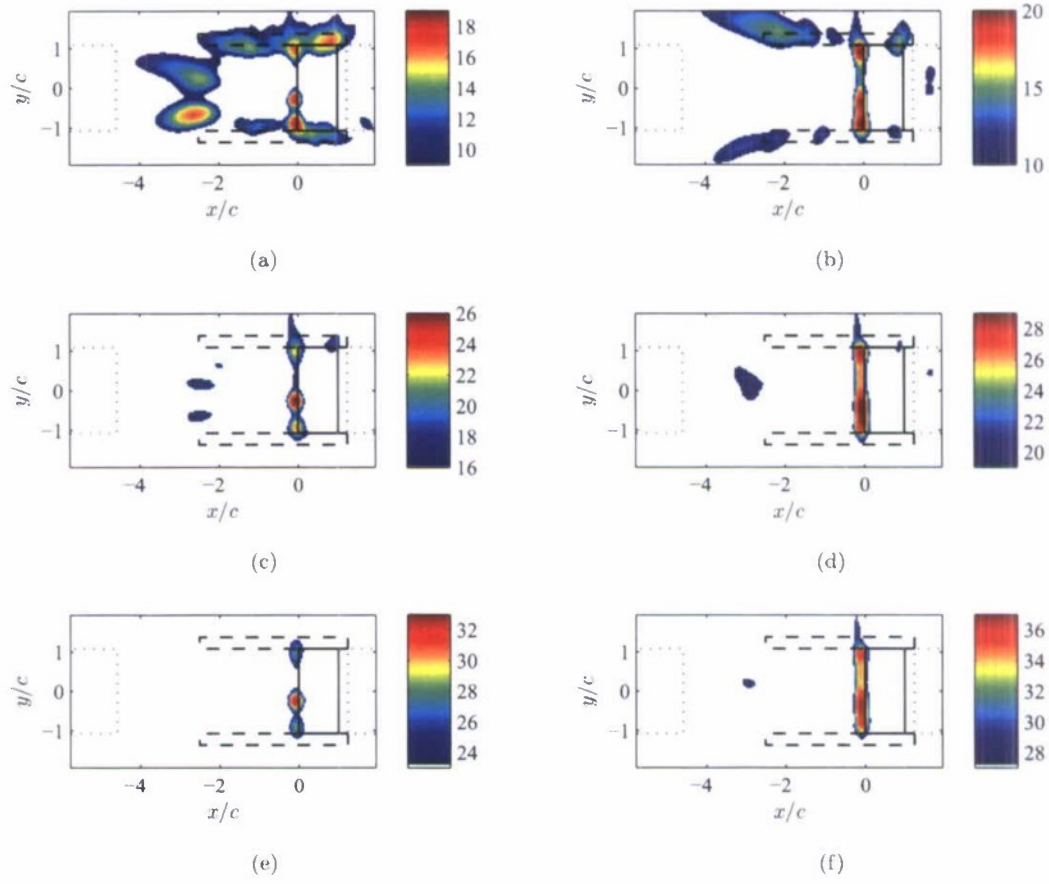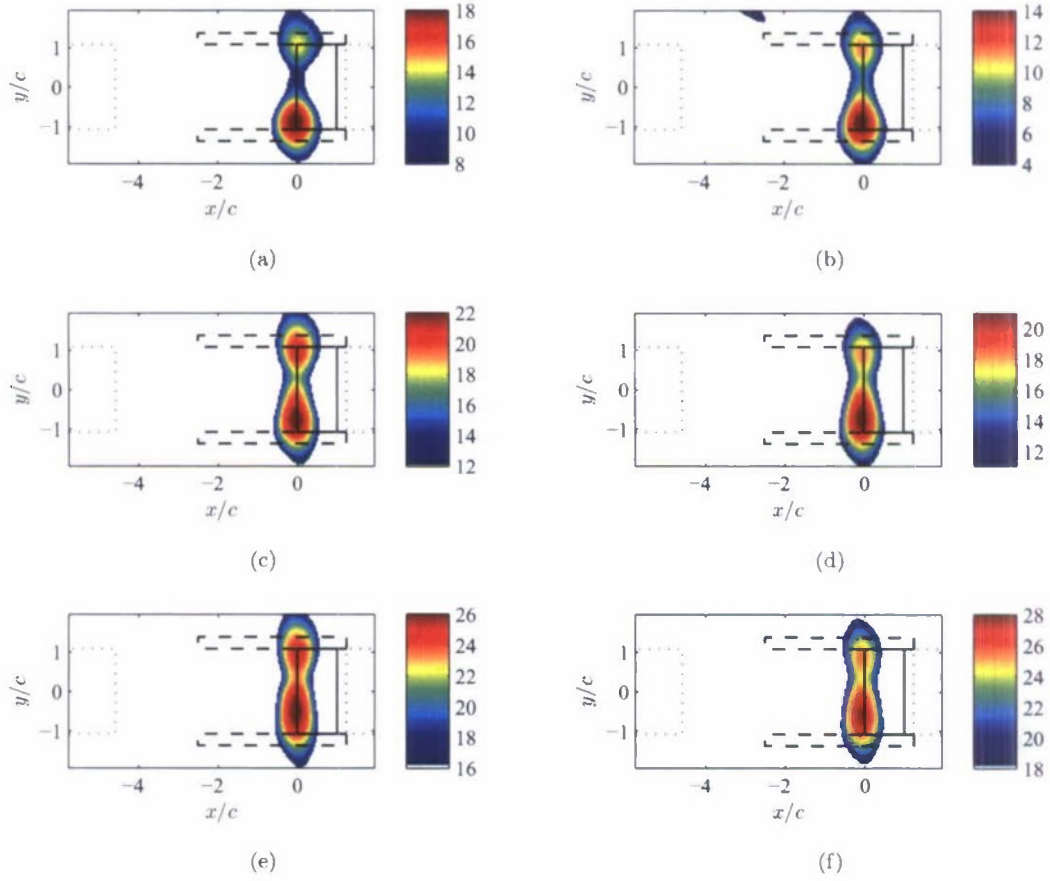
Figure 66: Outer array beam maps (dB) at 4 kHz, $Re_c = 6.5 \times 10^5$, $h/c = 0.0019$. a) SSB, $C_\mu = 0.037$. b) OSB, $C_\mu = 0.040$. c) SSB, $C_\mu = 0.065$. d) OSB, $C_\mu = 0.071$. e) SSB, $C_\mu = 0.10$. f) OSB, $C_\mu = 0.11$.

Figure 67: Outer array beam maps (dB) at 8 kHz, $Re_c = 6.5 \times 10^5$, $h/c = 0.0019$. a) SSB, $C_\mu = 0.037$. b) SSB, $C_\mu = 0.040$. c) SSB, $C_\mu = 0.065$. d) OSB, $C_\mu = 0.071$. e) SSB, $C_\mu = 0.10$. f) OSB, $C_\mu = 0.11$.
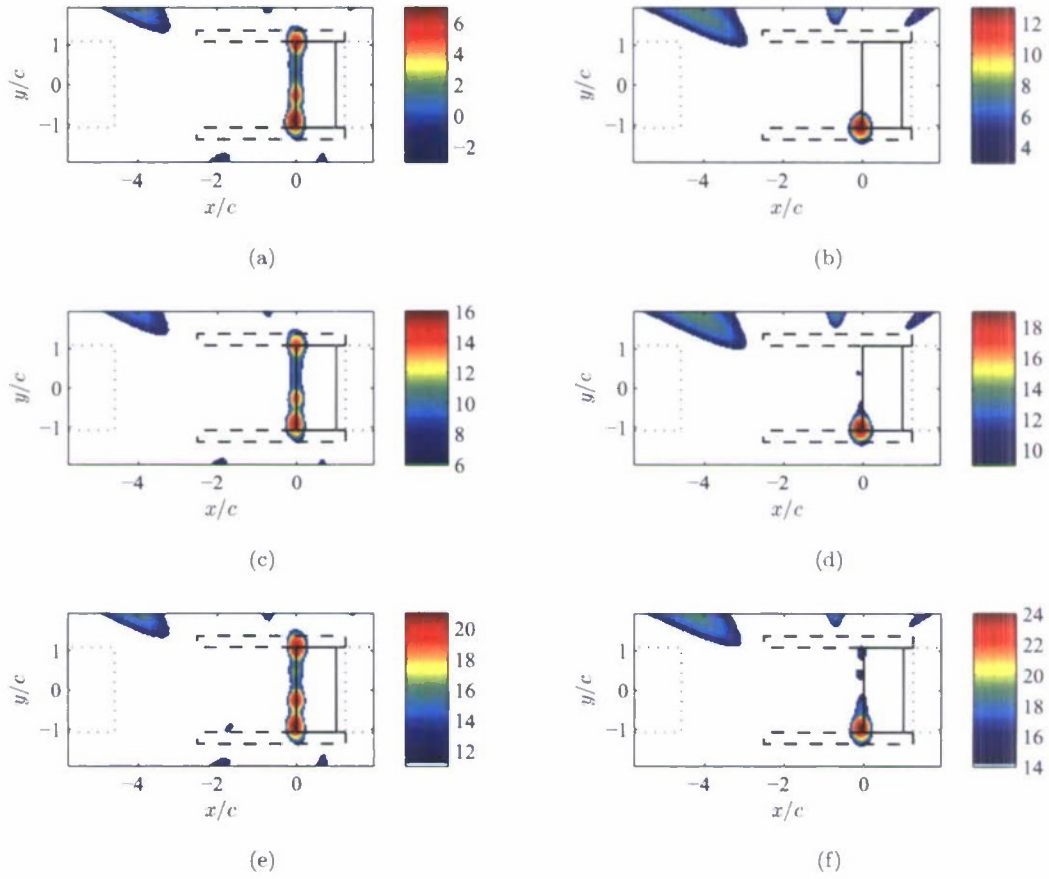
Figure 68: Inner array beam maps (dB) at 16 kHz, $Re_c = 6.5 \times 10^5$, $h/c = 0.0019$. a) SSB, $C_\mu = 0.037$. b) OSB, $C_\mu = 0.040$. c) SSB, $C_\mu = 0.065$. d) OSB, $C_\mu = 0.071$. e) SSB, $C_\mu = 0.10$. f) OSB, $C_\mu = 0.11$.
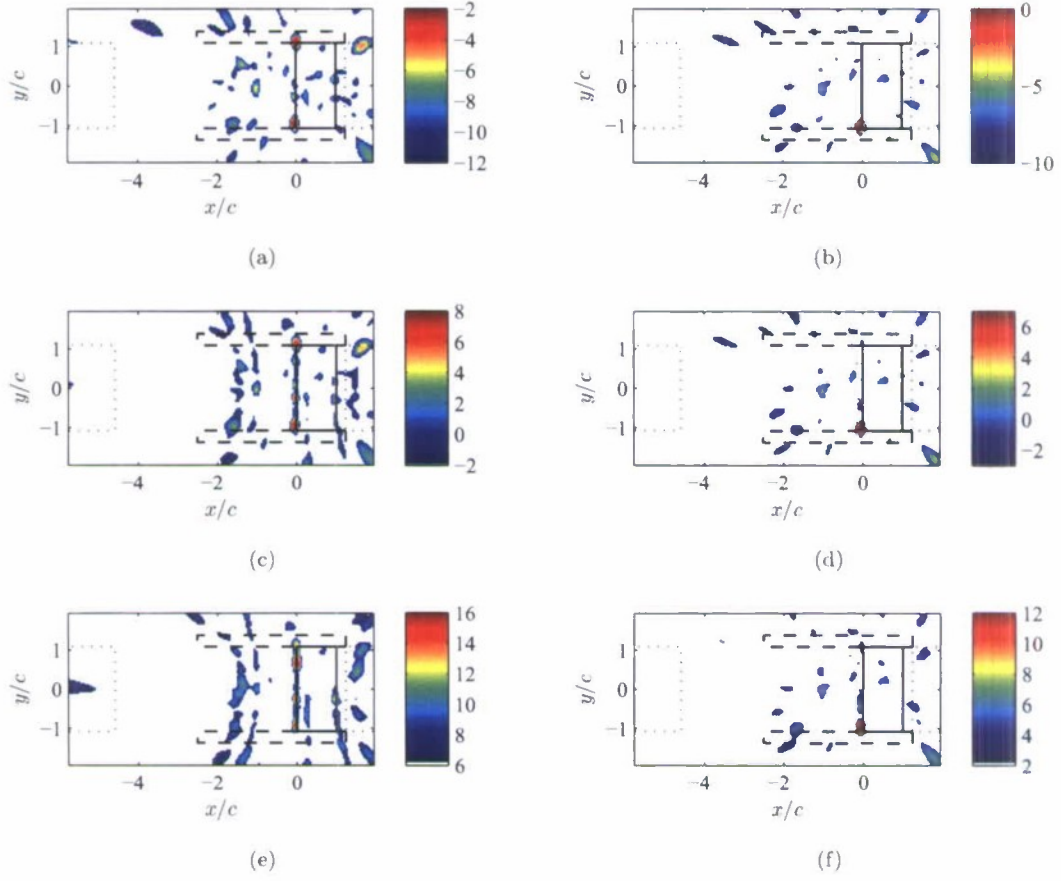
Figure 69: Inner array beam maps (dB) at 32 kHz, $Re_c = 6.5 \times 10^5$, $h/c = 0.0019$. a) SSB, $C_\mu = 0.037$. b) OSB, $C_\mu = 0.040$. c) SSB, $C_\mu = 0.065$. d) OSB, $C_\mu = 0.071$. e) SSB, $C_\mu = 0.10$. f) OSB, $C_\mu = 0.11$.

Figure 70: Inner array beam maps (dB) at 64 kHz, $Re_c = 6.5 \times 10^5$, $h/c = 0.0019$. a) SSB, $C_\mu = 0.037$. b) OSB, $C_\mu = 0.040$. c) SSB, $C_\mu = 0.065$. d) OSB, $C_\mu = 0.071$. e) SSB, $C_\mu = 0.10$. f) OSB, $C_\mu = 0.11$.
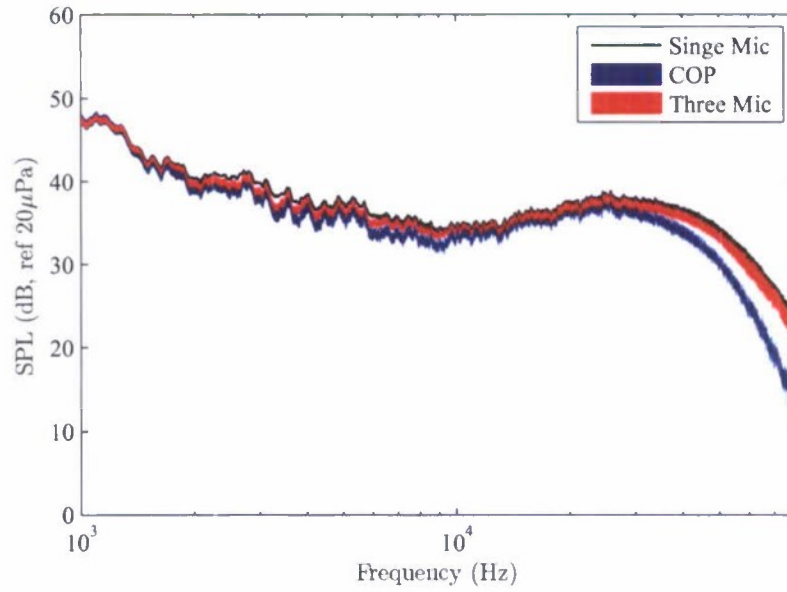
Figure 71: Comparison of free-standing microphone processing techniques for SSB, $Re_c = 6.5 \times 10^5$, $C_\mu = 0.11$, and $h/c = 0.0019$ (16 Hz bin width).
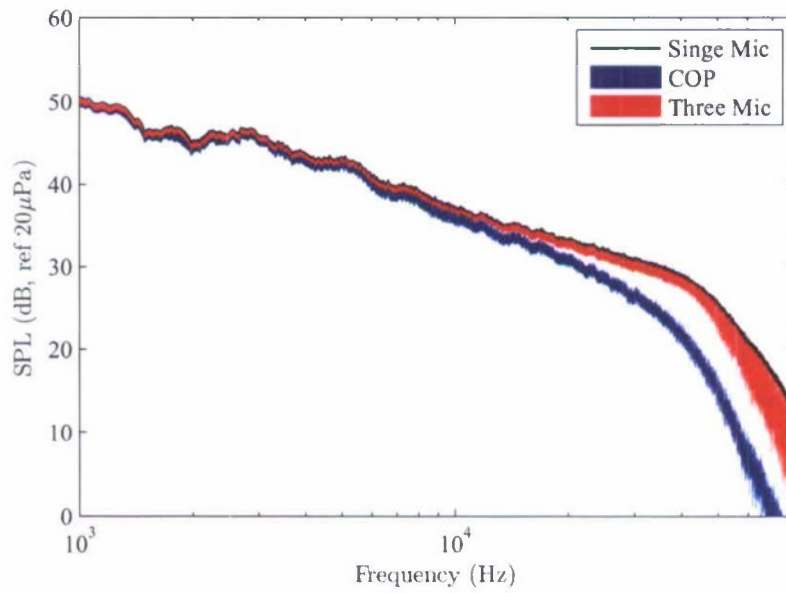

Figure 72: Comparison of free-standing microphone processing techniques for OSB, $C_\mu = 0.10$, $Re_c = 6.5 \times 10^5$, and $h/c = 0.0019$ (16 Hz bin width).
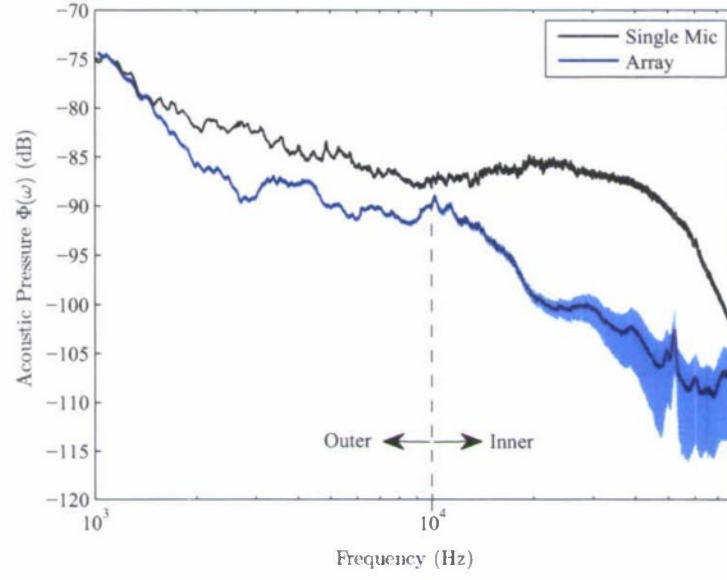
Figure 73: Single microphone and integrated array spectra (16 Hz bin width) for SSB, $C_\mu \approx$ 0.065, $Re_c = 6.5 \times 10^5$, and $h/c = 0.0019$.
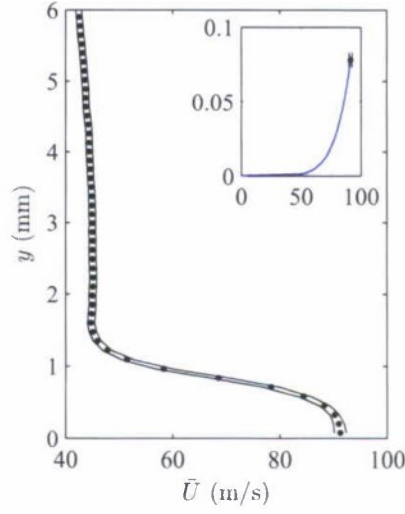

Figure 74: Mean tangential velocity profile along trailing edge at $r\theta/c = 0.0129$, $Re_c = 6.5 \times 10^5$, $C_\mu = 0.057$, $h/c = 0.0019$ with one-seventh power curve inset (Prandtl 1961).
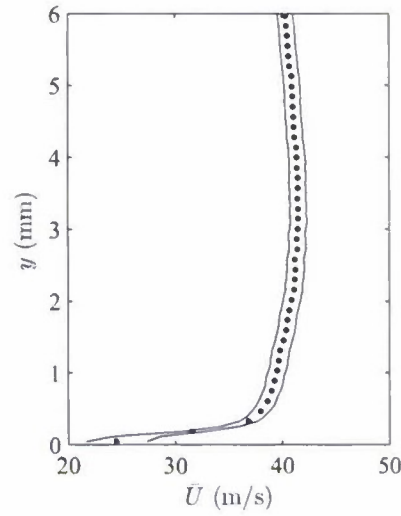
Figure 75: Mean tangential velocity profile at slot lip edge, $Re_c = 6.5 \times 10^5$, $C_\mu = 0.057$, $h/c = 0.0019$. Notice the local maximum velocity. Only every other point is displayed for clarity.
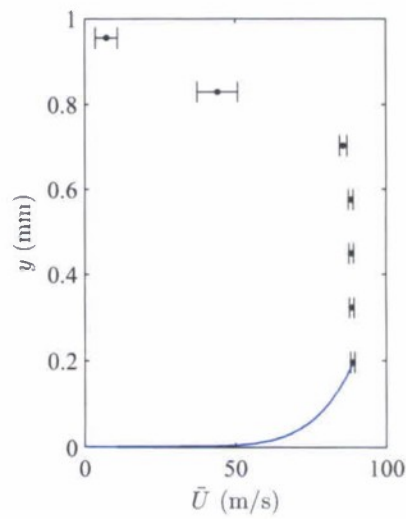

Figure 76: Mean tangential velocity profile at slot exit with one-seventh power curve. $Re_c = 6.5 \times 10^5$, $C_\mu = 0.057$, $h/c = 0.0019$ (Prandtl 1961).
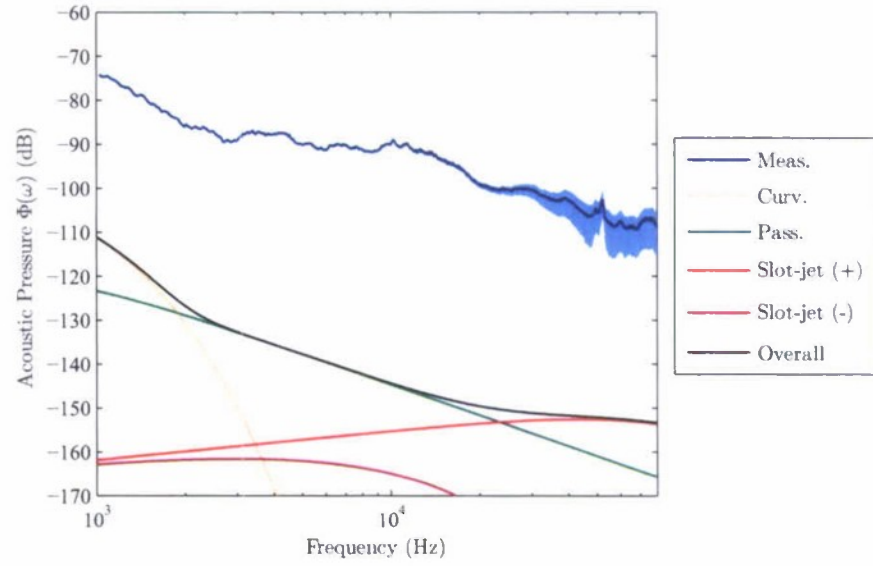
Figure 77: Howe's model, evaluated for $Re_c = 6.5 \times 10^5$, $C_\mu = 0.057$, $h/c = 0.0019$, providing only airfoil geometry details and test conditions. The array spectrum represents SSB, $Re_c = 6.5 \times 10^5$, $C_\mu = 0.065$, $h/c = 0.0019$.

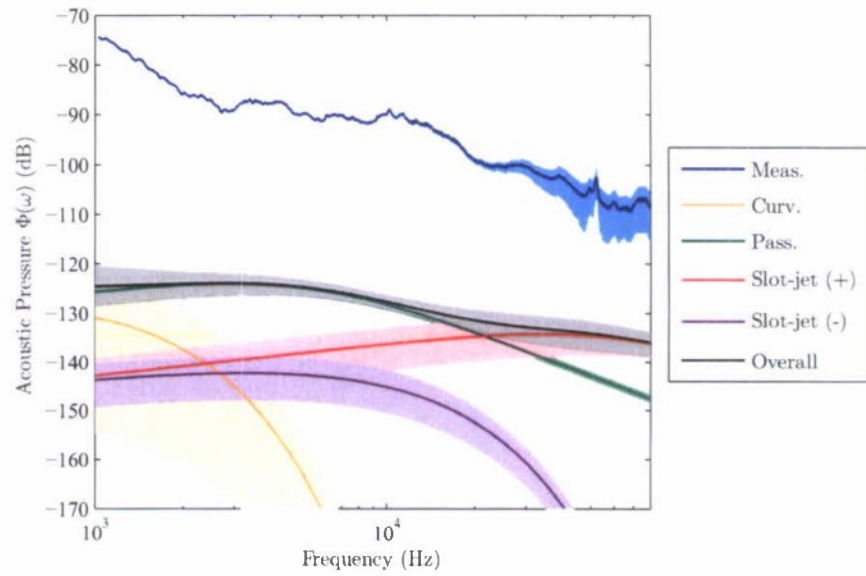Figure 78: Howe's model, evaluated for $Re_c = 6.5 \times 10^5$, $C_\mu = 0.057$, $h/c = 0.0019$ using length and velocity scales estimated from PIV data. The array spectrum represents SSB, $Re_c = 6.5 \times 10^5$, $C_\mu = 0.065$, $h/c = 0.0019$.
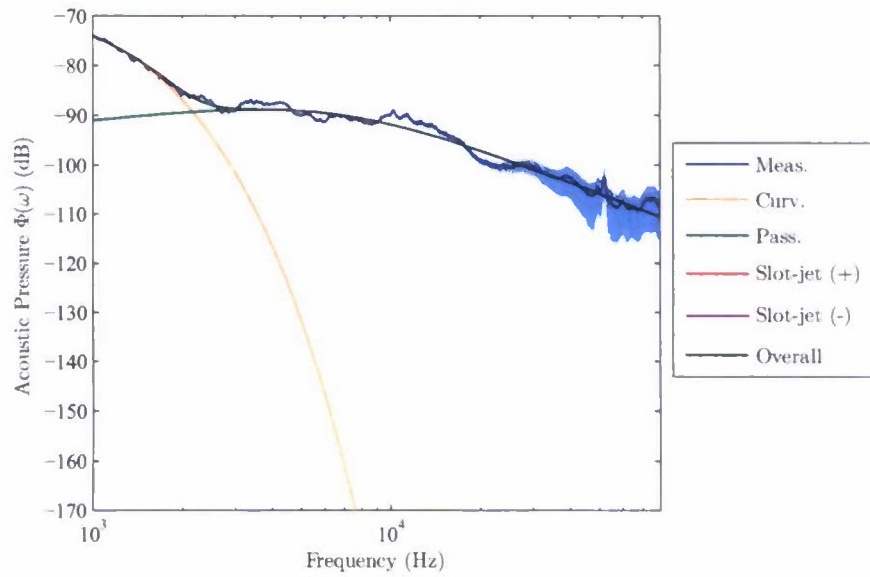
Figure 79: Best fit of Howe's model to measured spectrum.

Table 1: Scaling of length and velocity scales from similarity solution of Guitton & Newman (1977); x is the arc length and a is a constant

Parameter	Scaling
R	x
$y_{1/2m}$	x
U_{max}	x^a

Table 2: Scaling of length and velocity scales from general similarity solution of a curved wall jet in a freestream; x is the arc length and a is a constant

Parameter	Scaling
R	x
y_1	x
y_2	x
U_1	x^a
U_2	x^a
U_2/U_1	constant

Table 3: Test cases presented

Case	$h/c\,(\times 10^{-3})$	$Re_c\,(\times 10^5)$	$U_\infty(m/s)$	$U_{jet}(m/s)$	U_{jet}/U_∞	C_μ
1	1.9	6.5	20	20	1	0.0039
2	1.9	6.5	20	40	2	0.015
3	1.9	6.5	20	80	4	0.057
4	1.9	6.5	20	38	1.9	0.014
5	1.9	13	40	78	2.0	0.014
6	2.9	6.5	20	32	1.6	0.014

Table 4: Length and velocity scales used to evaluate Howe's model

Noise type	Predicted (Howe 2002)			PIV Measurement		
	U (m/s)	δ_* (mm)	v_* (m/s)	U (m/s)	δ_* (mm)	v_* (m/s)
Curvature	56.3	1.04	1.97	91.3	0.010	9.57
Passive slot	32.0	1.04	1.12	41.4	0.140	2.78
Slot-jet	79.9	0.019	2.80	88.8	0.025	6.84

Table 5: Example of scales required for Howe's model to match measurement

Noise type	U (m/s)	δ_* (mm)	v_* (m/s)
Curvature	63.1	0.5	20.0
Passive slot	59.8	0.17	19.0
Slot-jet	88.8	1.0×10^{-5}	7.60

References

ABRAMSON, J. 1975 Two-dimensional subsonic wind tunnel evaluation of a 20-percent-thick circulation control airfoil. *Tech. Rep.* ASED-331. DTNSRDC.

AMIET, R. K. 1978 Refraction of sound by a shear layer. *J. Sound Vib.* **58** (3), 467–482.

ARNOLD, D. P., NISHIDA, T., CATTAFESTA, L. & SHEPLAK, M. 2003 A directional acoustic array using silicon micromachined piezoresistive microphones. *J. Acoust. Soc. Am.* **113** (1), 289–298.

BAHR, C. 2010 An assessment of trailing edge noise measurement techniques. PhD thesis, University of Florida.

BAHR, C., YARDIBI, T., LIU, F. & CATTAFESTA, L. 2008 An analysis of different measurement techniques for airfoil trailing edge noise. *Paper* 2008-2957. AIAA.

BENDAT, J. S. & PIERSOL, A. G. 2000 *Random Data Analysis and Measurement Procedures*, 3rd edn. John Wiley & Sons, Inc.

BROOKS, T. F. & HODGSON, T. H. 1981 Trailing edge noise prediction from measured surface pressures. *J. Sound Vib.* **78** (1), 69–117.

CHANDRASEKHARAN, V. 2009 A microscale differential capacitive wall shear stress sensor. PhD thesis, University of Florida.

DOUGHERTY, R. P. 2002 *Aeroacoustic Measurements*, chap. 2, pp. 63–97. Springer-Verlag: Berlin, Heidelberg & New York.

ENGLAR, R. J. & WILLIAMS, R. M. 1972 Test techniques for high lift, two-dimensional airfoils with boundary layer and circulation control for application to rotary wind aircraft. *Tech. Rep.*. NSRDC.

FLORYAN, J. M. 1986 Gortler instability of boundary layers over concave and convex walls. *Phys. Fluids* **29** (8), 2380–2387.

GUITTON, D. E. & NEWMAN, B. G. 1977 Self-preserving turbulent wall jets over convex surfaces. *J. Fluid Mech.* **81** (1), 155–185.

HAN, G., DE ZHOU, M. & WYGNANSKI, I. 2006 On streamwise vortices and their role in the development of a curved wall jet. *Phys. Fluids* **18** (9), 095104–095104–14.

HOWE, M. S. 2002 Noise generated by a Coanda wall jet circulation control device. *J. Sound Vib.* **249** (4), 679 – 700.

HUTCHESON, F. V. & BROOKS, T. F. 2002 Measurement of trailing edge noise using directional array and coherent output power methods. *Paper* 2002-2472. AIAA.

KATZ, J. & PLOTKIN, A. 2001 *Low-Speed Aerodynamics*, 2nd edn. Cambridge University Press.

LAUNDER, B. E. & RODI, W. 1983 The turbulent wall jet - measurements and modeling. *Annu. Rev. Fluid Mech.* **15**, 429–459.

LIKHACHEV, O., NEUENDORF, R. & WYGNANSKI, I. 2001 On streamwise vortices in a turbulent wall jet that flows over a convex surface. *Phys. Fluids* **13** (6), 1822 – 1825.

MATHEW, J., BAHR, C., CARROLL, B., SHEPLAK, M. & CATTAFESTA, L. 2005 Design, fabrication, and characterization of an anechoic wind tunnel facility. *Paper* 2005-3052. AIAA.

MUNRO, S., AHUJA, K. K. & ENGLAR, R. J. 2001 Noise reduction through circulation control. *Paper* 2001-0666. AIAA.

NAUGHTON, J. W. & SHEPLAK, M. 2002 Modern developments in shear stress measurement. *Progress in Aerospace Sciences* **38**, 515–570.

NEUENDORF, R., LOURENCO, L. & WYGNANSKI, I. 2004 On large streamwise structures in a wall jet flowing over a circular cylinder. *Phys. Fluids* **16** (7), 2158 – 2169.

NEUENDORF, R. & WYGNANSKI, I. 1999 On a turbulent wall jet flowing over a circular cylinder. *J. Fluid Mech.* **381**, 1 – 25.

NISHINO, T. & SHARIFF, K. 2010 Numerical study of wind-tunnel sidewall effects on circulation control airfoil flows. *AIAA J.* **48** (9), 2123–2132.

NOVAK, C. J. & CORNELIUS, K. C. 1986 An LDV investigation of a circulation control airfoil flowfield. *Paper* 1986-0503. AIAA.

NOVAK, C. J., CORNELIUS, K. C. & ROADS, R. K. 1987 Experimental investigations of the circular wall jet on a circulation control airfoil. *Paper* 1987-0155. AIAA.

OELERMANS, S., BROERSMA, L. & SIJTSMA, P. 2007 Quantification of airframe noise using microphone arrays in open and closed wind tunnels. *Int. J. Acoustics* **6** (4), 309–333.

PANTON, R. L 2005 *Incompressible Flow*, 3rd edn. John Wiley & Sons, Inc.

POPE, A. & RAE, WILLLIAM H. 1984 *Low-Speed Wind Tunnel Testing*. Wiley-Interscience.

PRANDTL, L. 1961 *Collected Works*, , vol. 2. Springer, Berlin.

RAFFEL, M., WILLERT, C. E., WERELEY, S. T. & KOMPENHANS, J. 2007 *Particle Image Velocimetry*, 2nd edn. Springer-Verlag.

ROGERS, E. O. & DONNELLY, M. J. 2004 Characteristics of a dual-slotted circulation control wing of low aspect ratio intended for naval hydrodynamic applications. *Paper* 2004-1244. AIAA.

SALIKUDDIN, M., BROWN, W. H. & AHUJA, K. K. 1987 Noise from a circulation control wing with upper surface blowing. *J. Aircraft* **24** (1), 55–64.

SARIC, W. 1994 Görtler vortices. *Annu. Rev. Fluid Mech.* **26**, 379–409.

SLOMSKI, J. F. 2009 Reducing vortex shedding sound from a trailing edge above a wall jet. *Paper* 2009-778. AIAA.

STALNOV, O. & SEIFERT, J. 2010 On amplitude scaling of active separation control. *Active Flow Control II* .

UNDERBRINK, J. R. 2002 *Aeroacoustic Measurements*, chap. 3, pp. 98–217. Springer-Verlag.

WETZEL, D. 2011 An experimental investigation of circulation control acoustics. PhD thesis, University of Florida.

WHITE, F. M. 2006 *Viscous Fluid Flow*, 3rd edn. McGraw-Hill.

YARDIBI, T., BAHR, C., ZAWODNY, N., LIU, F., CATTAFESTA, L. N. & LI, J. 2010a Uncertainty analysis of the standard delay-and-sum beamformer and array calibration. *J. Sound Vib.* **329** (13), 2654–2682.

YARDIBI, T., ZAWODNY, N. S., BAHR, C., LIU, F., CATTAFESTA, L. N. & LI, J. 2010b Comparison of microphone array processing techniques for aeroacoustic measurements. *Int. J. Acoustics* **9** (6), 733–762.

ZHOU, M. D. & WYGNANSKI, I. 1993 Parameters governing the turbulent wall jet in an external stream. *AIAA J.* **31** (5).